DEVELOMENT OF TUNGSTEN-RHENIUM BASE TOOL FOR FRICTION STIR WELDING OF STEEL

BY

ZAFAR IQBAL

A Dissertation Presented to the
DEANSHIP OF GRADUATE STUDIES

KING FAHD UNIVERSITY OF PETROLEUM & MINERALS
DHAHRAN, SAUDI ARABIA

In Partial Fulfillment of the
Requirements for the Degree of

DOCTOR OF PHILOSOPHY

In

MECHANICAL ENGINEERING

JUNE 2016

KING FAHD UNIVERSITY OF PETROLEUM & MINERALS
DHAHRAN- 31261, SAUDI ARABIA

DEANSHIP OF GRADUATE STUDIES

This thesis, written by ZAFAR IQBAL under the direction of his thesis advisor and approved by his thesis committee, has been presented and accepted by the Dean of Graduate Studies, in partial fulfillment of the requirements for the degree of **DOCTOR OF PHILOSOPHY IN MECHANICAL ENGINEERING.**

Dr. Abdel Rahman Nasr Shuaib
(Advisor)

Dr. Zuhair Gasem
Department Chairman

Dr. Nesar Merah
(Co-Advisor)

Dr. Saheb Nouari
(Member)

Dr. Salam A. Zummo
Dean of Graduate Studies

16/6/16
Date

Dr. Nasser Al-Aqeeli
(Member)

Dr. Tahar Laoui
(Member)

Dedicated to my beloved parents, wife and daughters

ACKNOWLEDGMENTS

First of all, I would like to thank Almighty Allah, the most Beneficent and the most Merciful, for helping me to accomplish my thesis dissertation. I pay sincere tributes to my parents for all the prayers and support in achieving my professional objectives. I must not forget to thank my wife for all the care and support during difficult times.

Special thanks to my advisor, Professor Abdel Rahman Nasr Shuaib, for providing me all the wisdom and motivation to achieve my thesis goals. Dr. Shuaib has always inspired me a lot to carry out research on key issues especially which are application oriented. I deeply acknowledge the technical support, inspiration and motivation that I have received from Professor Dr. Nesar Merah in my PhD research work. My mentor, Dr. Nesar Merah has played a vital role in the successful completion of my PhD dissertation. I would like to pay special gratitude to Dr. Saheb Nouari who has supported me in the field of material processing. I have acquired so much wisdom from Dr. Nouari's experience. I acknowledge the valuable suggestions and support of my committee members, Dr. Nasser Al-Aqeeli and Dr. Tahar Laoui in the field of material development. I pay special gratitude to Dr. Fadi Al-Badour who has supported and guided me during the experimental work of FSW steel. I am very thankful to Dr. Fadi for sparing so much time for my guidance. I would like to thank Dr. Abdul Samad and Dr. Abdul Aziz Bazoune for their valuable input in the thesis dissertation. Thanks to Mr. Khawaja, Mr. Lateef, Mr. Kamal, Mr. Romeo, Mr. Sabir and Mr. Sadaqat for their support and assistance in completing my experimental work. I acknowledge the help provided by Mr. Nabeel Mehar, Mr. Irfan Somrow, and Mr. Ahmad.

I would like to also acknowledge the support and continuous motivation and encouragement of my best friend Dr. Rashid Hussain throughout my academic career.

I acknowledge the support provided by King Abdulaziz City for Science and Technology (KACST) through the Science and Technology Unit at King Fahd University of Petroleum and Minerals (KFUPM) for funding this work through projects No. NSTIP 11-ADV2130-04 and NSTIP 13-ADV-2155-04 as part of the National Science, Technology and Innovation Plan.

TABLE OF CONTENTS

LIST OF TABLES

LIST OF FIGURES

LIST OF ABBREVIATIONS

PCBN : Polycrystalline Cubic Boron Nitride

SPS : Spark Plasma Sintering

FSW : Friction Stir Welding

FSSW : Friction Stir Spot Welding

HAZ : Heat Affected Zone

SZ : Stir Zone

RM-1 : Research Machine 1

TMAZ : Thermomechanical Affected Zone

PCA : Process Control Agent

MA : Mechanical Alloying

W : Tungsten

Re : Rhenium

SE : Secondary Electron

BSE : Back Scattered Electron

XRD : X- Ray Diffraction

FESEM : Field Emission Scanning Electron

ABSTRACT

Full Name	:	[Zafar Iqbal]
Thesis Title	:	[Development of Tungsten-Rhenium base tool for friction stir welding of steel]
Major Field	:	[Materials and Manufacturing]
Date of Degree	:	[June 2016]

The development of tool materials from tungsten-rhenium (W-Re) alloys friction stir welding (FSW) of steels and high strength materials remains a key challenge because these alloys are difficult to synthesize and consolidate by conventional means. Dense nanocrystalline W-25%Re alloy & W-25%Re-HfC composite material with nanostructured matrix and uniform distribution of the reinforcement was successfully developed by mechanical alloying and spark plasma techniques. Mechanical alloying of partially alloyed W-25wt. %Re powder for 25 h yielded a single nanostructured solid solution with a crystallite size of 13 nm. The fully alloyed powder was reinforced with 5 and 10 vol. % of HfC particles and further milled for 15 h, which led to the formation of homogenous composite powders. The homogenous distribution of HfC particles, obtained by mechanical alloying, was maintained in the consolidated samples. Crystallite size of the matrix phase in the sintered composites remained in the nanometer range and did not exceed 100 nm. Spark plasma sintering of the partially and fully alloyed monolithic W-25wt. %Re alloys, at 1800ºC for 10 minutes, resulted in relative density values of 98.2 and 97.8 %, respectively. The spark plasma sintering of W-25Re-HfC composites containing 5 and 10 vol. % HfC, at 1800ºC for 10 minutes, developed relative density values of 96.9 and 96.2 %, respectively. The composite containing 10 vol. % of HfC possessed the highest microhardness value of 495. Thermal conductivity of monolithic alloy sintered at 1500ºC was found to be 39 $Wm^{-1}.K^{-1}$, whereas it was improved to 48 $Wm^{-1}.K^{-1}$ for the sample sintered at 1800ºC. Incorporation of HfC caused thermal conductivity to decrease to 34 $Wm^{-1}.K^{-1}$ for the sample containing 10 vol% HfC. The sliding wear results of the monolithic alloy showed that wear resistance of the SPS consolidated powder increased with the increase of sintering temperature. Wear resistance was found to improve with the addition of 5vol% HfC in W-25wt%Re matrix. Wear tests revealed that the dominant wear mechanism was adhesive wear, which was attributed to the presence of HfC debris and pullout sites. The coefficient of friction values of the SPS consolidated powders were found to be dependent on temperature and type of alloy. The newly developed nanocrystalline fully alloyed W-25wt%Re disc was used as a pin tool for the exploratory friction stir spot welding (FSSW) on thin mild steel plates in order to confirm its feasibility and to evaluate its performance in harsh conditions of the process. A heat treated AISI 4140 alloy steel holder was manufactured to hold the small disc. Good quality spot welds were obtained using the experimental tool tip made from the consolidated powders. The tool has shown excellent resistance to abrasion, adhesion and diffusional wear during the severe and harsh conditions of FSW of steel.

ملخص الرسالة

الاسم الكامل: ظفر إقبال

عنوان الرسالة: تطوير آداة للحام التحريكي الدوراني للفولاذ من خليط مادتي التنجستان والرينيوم

التخصص: التصميم والتصنيع

تاريخ الدرجة العلمية: مايو 2016

إن التطور في مجال أدوات القطع لتطبيقات درجة الحرارة العالية مثل اللحام الإحتكاكي للفولاذ والمواد ذات القوة العالية ظلت تحدياً وذلك لصعوبة تركيب وتماسك تلك المواد بالطرق التقليدية. في الدراسة الحالية تم تطوير سبيكية ذات بنية نانومترية بطريقة الخلط الميكانيكي mechanical alloying (MA) ومن ثم التلبيد بشرارة البلازما spark plasma sintering (SPS). تلك السبيكة تحتوي على 25% من معدن التنجستان والرينيوم مع تركيب متجانس من مادة W-25Re-HfC تحتوي على نسبية حجمية 5 و 10 % من حبيبات مادة HfC. الخلط الميكانيكي للمسحوق الخام والمكونة من 25% تنجستان مع الرينيوم ونصف المخلوطة لمدة 25 ساعة أنتجت خليط صلب لتركيب نانومتري مفرد بحجم بلوري 13 نانومتر تم تقوية المسحوق المخلوطة ب 5 و 10 نسبة حجمية من حبيبات الهافنيوم الكربوني HfC وتمت مواصلة عملية الطحن 15 ساعة إضافية ، نتج عن ذلك تكون مسحوق خليط مركب متجانس . الحجم البلوري في طور المصفوفة في العينات الملبدة ظلت في المدى النانومتري ولم تتخطى 100 نانومتر. ان السبائك الجزئية والسبائك الكلية W-25wt المعدة باستخدام التلبيد بشرارة البلازما في درجة حرارة 1800 ºC لمدة 10 دقائق ، تمتلك كثافة نسبية بقيمة 98.2٪ و 97.8٪ بالترتيب. بينما مركبات W-25Re-HfC تحتوي على مقدار حجم 5 إلى 10 . كربيد الهافنيوم و التي انتجت بنفس الظروف السابقه ، تملك كثافة نسبية بقيمة 96.2٪ و 96.9٪ بالترتيب. المركب المحتوي على مقدار حجم 10٪ من كربيد الهافنيوم تمتلك أعلى " للصلادة الدقيقة " بقيمة 495. التوصيل الحراري في السبيكة المكونة من وحدة واحدة المتكلسة في درجة حرارة 1500 ºC وجد أنها تحوز على 39 W/m.K في حين حسنت العينة المستخدمة في درجة حرارة 1800 ºC إلى 48 W/m.K. وجد أن التوصيل الحراري يتقلص مع دمج محتويات كربيد الهافنيوم وتم الإيفاد بقيمة 34 W/m.K للعينة المستخدمة لحجم 10٪ من كربيد الهافنيوم. أظهرت نتائج اختبار التآكل الانزلاقي أن مقاومة التآكل ازدادت للسبائك المكونة من وحدة واحدة مع ازدياد درجة

حرارة التكلس. التكوين الخاص بالتآكل المورفولوجي لعلامات الانزلاق والحطام تدل بأن الآلية الرئيسية للتآكل كانت ذي طبيعة كاشطة. وجد أن مقاومة التآكل تتحسن بإضافة حجم 5٪ من كربيد الهافنيوم في مصفوفة W-25wt %Re. تحليل مسار حطام المركب يكشف بأن السبب الرئيسي للتآكل كان اللصقية والذي يعزى إلى وجود حطام كربيد الهافنيوم ووجود مواقع السحب. يعتمد معامل الاحتكاك (coefficient of friction) السبائك المصنعة باستخدام التلبيد بشرارة البلازما على درجة الحرارة ونوع من سبائك.

أن السبائك المطورة في هذه الدراسة تم استخدامها لصناعة أداة اللحام التحريك الاحتكاكي لأغراض اختبارها في الظروف القاسية، ولقد تبين من النتائج قدرة السبائك المنتجة على مقاومة الاهتراء الناتج عن الاحتكاك.

CHAPTER 1

INTRODUCTION

This chapter proposes a feasible route for the development of relatively new class of Tungsten-Rhenium (W-Re) base tool materials for friction stir welding (FSW) of steel and high melting point materials. In future, W-Re alloy tool materials can replace ceramic base tools which are currently being used on commercial scale for FSW of steel as the former class of material can be developed with ease and has several advantages over ceramic counterparts. In this chapter, it is also proposed that W-Re base tool materials can be synthesized by powder metallurgy route using a unique combination of mechanical alloying (MA) and spark plasma sintering (SPS).

1.1 Problem statement

Friction Stir Welding (FSW) process was invented by The Welding Institute (TWI) in 1991[1]. The process employs a spinning pin tool that produces frictional heat in the welding of the workpiece. The pin tool is pressed into contact with a seam to be welded. A typical FSW system is shown in Figure 1-1 [2]. The base metal heats up due to the rubbing of tool faces by visco-plastic dissipation of mechanical energy at high strain rates [3][4][5]. When the heat of the workpiece reaches about 80% of its melting point it becomes soft and easy to form joining.

FSW is well established process for welding of low melting point materials such as Aluminum. Microstructural examination of aluminum alloys joined by FSW exhibits several zones in the weld or bead. These are Stir Zone (SZ), Thermo-Mechanical Heat

Affected Zone (TMAZ) around the nugget and Heat Affected Zone (HAZ) [6][7][8]. Stir zone experiences the highest strain rates and consequently higher temperatures [9]. These zones are related to thermomechanical cycle during FSW of aluminum metal and alloys.

Although the FSW process has initially been developed for joining non-ferrous materials such as aluminum, by using suitable tool materials the use of the process has been extended to harder and higher melting point materials such as steels, titanium alloys and copper. Recently, a considerable attention has been given to FSW of high melting temperature alloys such as steel, due to the process advantages over conventional welding methods, which avoids many problems of fusion welding like porosity, cracking, and solidification [9].

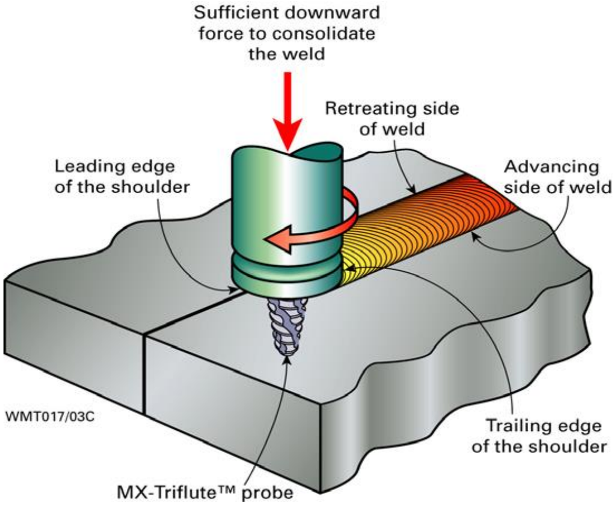

Figure 1-1 Schematic of friction stir welding process [2]

Friction Stir Welding (FSW) tool is the most important component which dictates the success of the process. Recently efforts have been made to produce cost effective and reusable tool for Friction Stir Welding (FSW) of steel and hard alloys but majority of these efforts need improvement in tool material development aspect [10][11][12]. FSW of these hard alloys put stringent conditions on the requirements for the tool material as tool will be exposed to harsh condition during the process.

PCBN (Polycrystalline Boron Nitride) and other ceramic tool materials such as Si_3N_4 are currently being used on commercial scale due to their high hardness and strength at elevated temperature. The issue with the use of PCBN is that its processing involves a combination of very high temperature and pressure. Moreover most of them has tendency to fail during the plunging stage due to its low toughness [10]. Tool wear affects not only the tool life but also the weld characteristics. It has also been noted that FSW of steels with PCBN involves boron and nitrogen pick-up from worn tool leaving the material susceptible to corrosion and pitting [10]. Workpiece may be contaminated with Nitrogen. Nitrogen can also react with oxygen to make detrimental oxides. PCBN has high thermal conductivity (100– 250 W m^{-1} K^{-1}) which results in higher heat loss and lower workpiece temperatures. These issues motivates the researcher to develop new tool materials to overcome these challenges.

1.2 Approach to address the problem

The challenges of finding a suitable tool material for friction stir welding of steels and high temperature alloys has been addressed by replacing PCBN with tungsten base alloys and composites [12]. Although pure tungsten (W) has sufficient strength at elevated temperatures, its use has been limited by its poor toughness at room temperature and has showed great amount of wear when used as tool material. Since tungsten is also susceptible to embrittlement and recrystallization at temperatures higher than 1200^{o}C [11], Rhenium has been added to lower the ductile to brittle transition temperature and increases the recrystallization temperature [12].

Present work will involve the synthesis of W-25%R nanocrystalline alloy reinforced with Hafnium Carbide HfC by using mechanical alloying and Spark Plasma Sintering (SPS), a novel consolidating technique. The developed tool material is expected to bear the harsh conditions of FSW of steel. It should have relatively high hardness, high wear resistance. It can be machined and reused and must be cost effective. It should have a reasonable thermal conductivity in order to avoid the heat loss.

The main objective of selecting this composite is to employ the advantage of superior high temperature properties of these elements (all the components have melting points more than 3000^{o}C). The addition of Re will decrease the ductile to brittle transition temperature of the tool. Nanocrystalline W-25%Re solid solution can be synthesized by MA and SPS. The homogenous dispersion of HfC particles inside the W-25%Re will enhance the strengthening effect at high temperature.

1.3 Mechanical alloying (MA) and spark plasma sintering (SPS)

Mechanical alloying is non-equilibrium powder metallurgy process for fabrication of several alloys and advanced materials at room temperature which are difficult to synthesize by conventional melting, casting and other techniques. To date, little attention has been given to mechanical alloying to synthesize W-Re alloy and their composites. The term *mechanical alloying* (MA) is being extensively used in the materials science and metallurgy field which involves the alloying of two or more elements to make equilibrium and non-equilibrium products [13]. Figure 1-2 shows the schematic of planetary ball mill. Centrifugal forces are responsible for the collisions between the constituents of the ball mill

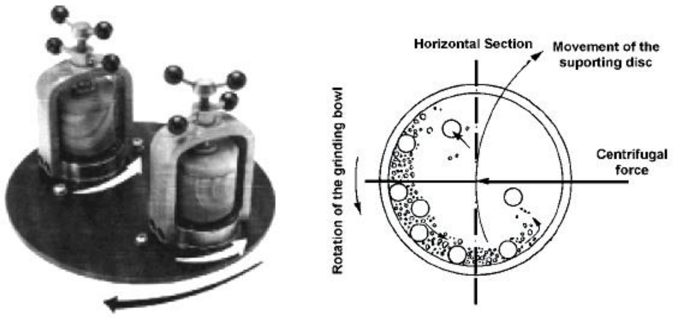

Figure 1-2 Schematic drawing of a high-energy planetary ball mill [13]

One of the key challenges in powder metallurgy is to choose a suitable sintering technique that can retain the developed microstructure by reducing undesirable grain growth. Conventional sintering techniques often lead to undesirable grain growth, reduced densification and lower strength due to the longer sintering time and higher temperature involvement. SPS is emerging as an effective sintering technique for the consolidation of many alloys and composites [14][15]. SPS is a very rapid consolidation technique for the synthesis of fully dense nanocrystalline materials at lower temperature as compared to traditional sintering techniques. Moreover SPS does not need any pre-compaction of the powders. The grain growth of initial microstructure is retarded due to low temperature and less time involvement in SPS as compared to that of hot and hot isostatic press techniques and other conventional techniques. In fact, the simultaneous application of pressure and current reduces the time for sintering. Resistance pulse heating, which results in high localized temperature and the simultaneously assisted consolidation pressure, are key factors for consolidation of nano size powders without causing grain growth. Furthermore, the generation of spark plasma pulse helps in removing the oxide layer which further activates the clean surfaces for rapid sintering.

Spark plasma sintering process involves the heating of powders and die by pulse current. It involves uniform heating and surface purification by SPS. Figure 1-3 shows the schematic of SPS process [16]. The SPS system consists of uniaxial press, vacuum chamber, pulse generator and temperature and pressure controllers. Pulse current and pulse duration along with holding time and ramp rate will control the temperature of the consolidating powders. The DC pulse generates the joule heating effect. The advantages of SPS include the ease of purification of powder particles by the joule heating resulting in lower sintering temperature and time as shown in Figure 1-4.

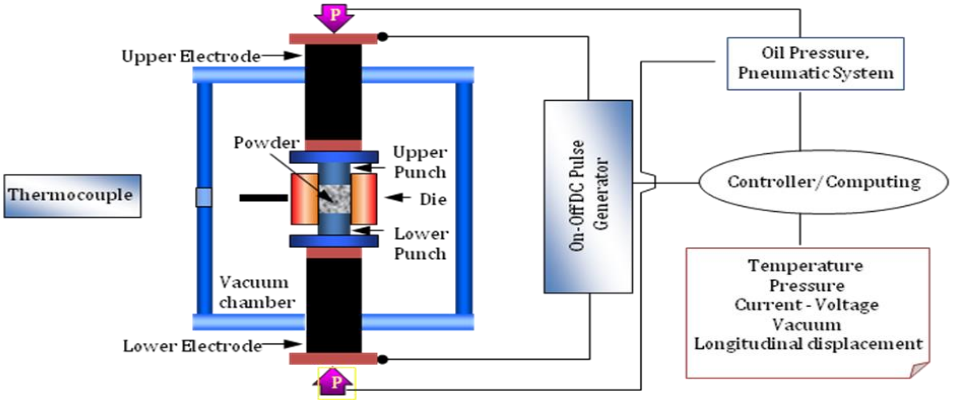

Figure 1-3 schematic of spark plasma sintering process [16]

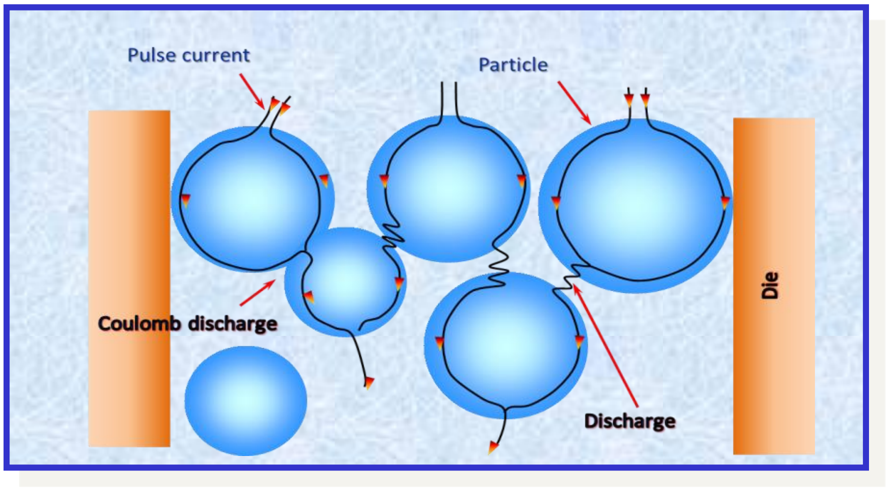

Figure 1-4 Direct Current-pulse current flow through the particles [16]

1.4 Goals and organization of the dissertation

The thesis dissertation is comprised of 6 chapters. First chapter is dedicated to stating the tom problem definition, its importance and causes, and a proposed approach for its solution. Chapter 2 describes the detailed literature review of potentially existing tool material candidates for FSW of steel and harder alloys. It also discusses the quality of the weld and FSW process parameters. Chapter 3 is dedicated for the synthesis and characterization of W-25%Re-HfC (both alloy and composites) tool materials using mechanical alloying. Chapter 4 discusses the subsequent consolidation of synthesized powders by SPS. This chapter also evaluates the newly developed pin tool materials by various physical, mechanical and tribological techniques. In chapter 5, a commercial W-25wt%Re pin tool is used for FSW of mild steel. The objective of using a commercial tool is to streamline the FSW process and to acquire baseline parameters for newly developed nanocrystalline W-Re tool for welding steels and high temperature alloys. In the last part of this chapter, newly developed nanocrystalline experimental tool was tested for friction stir spot welding of mild steel. Integrity of the tool and soundness of the weld was examined. Chapter 6 summarizes the conclusions and includes future recommendations.

CHAPTER 2

LITERATURE REVIEW

Chapter 2 includes a comprehensive literature review of different classes of tool materials, their synthesis and finally use of some of these tool materials for the FSW of steel and other hard alloys. The chapter also provides microstructural, mechanical and physical characterization of different tool materials developed by different consolidating techniques

2.1 Tool materials

There are several varieties of tool materials available in the markets, which include: high carbon steels, high speed steels (HSS), and cemented carbides (WC-based and ceramics, alumina-based, silicon nitride-based, sintered polycrystalline diamond), and sintered polycrystalline cubic boron nitride (PCBN). Diamond and cubic boron nitride (BN) are known as super hard materials due to their exceptional hardness. So we can say that going from carbon steels to diamond, the tool material shows an increase in wear resistance, hardness, plastic deformation resistance, and cost while the thermal shock resistance and ease of fabrication decrease

2.1.1 Sintered polycrystalline cubic boron nitride (PCBN)

Cubic boron nitride (cubic BN, Knoop hardness 4700 kgfmm^{-2}) is not available in nature. Synthesis of cubic BN requires the transformation of BN from hexagonal to cubic form at high temperature-high pressure. Figure 2-1 compares important mechanical properties of friction and fusion welds with those of the parent metal [19]. Diamond is the hardest materials (Knoop hardness 8000kgfmm^{-2}). The brittleness of some important tool materials such PCBN is a major issue that needs to be addressed.

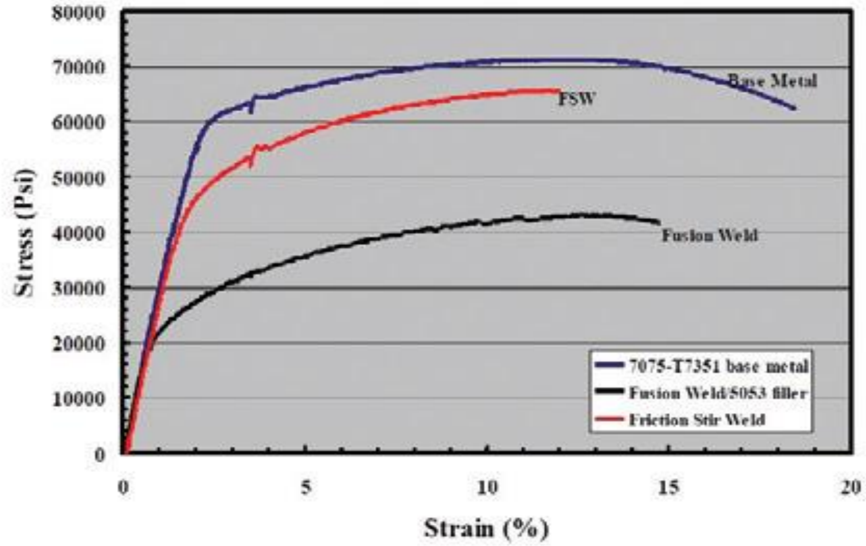

Figure 2-1 Mechanical properties of FSW, fusion welds and parent metal [19]

2.1.2 Tungsten based tools

Commercially pure tungsten (cp-W) is strong at higher temperatures but has poor toughness at room temperature. Pure tungsten exhibits high wear when utilized as a tool material for Friction Stir Welding of steels and titanium alloys. Exposure of cp-W to temperatures in higher than 1473 K results in crystallization and brittleness when cooled to room temperature. Addition of Re to tungsten lowers the ductile to brittle transition temperature as a result of changing the Peierls stress for dislocation motion. This led to the development of tungsten–rhenium alloys, with W–25 wt-%Re as a candidate material for FSW tools [12]. Steels and titanium alloys are friction stir welded by W–25 wt-%Re tool. The weld microstructure can be affected due to interaction with the tool material. Wear of the tool will increase the cost of the tool if the tool has lower yield strength at elevated temperature [12]. The tool material under investigation should have high strength, high thermal conductivity and low coefficient of thermal expansion at high temperature. The interaction of work piece with the tool is also important at high temperature. Pin tools made from PCBN and W based alloys have found to be suitable candidates for FSW of steel and titanium alloys.

Oxidation of the tool is also a serious concern during FSW. Figure 2-2 shows the high oxidative resistance of Tungsten and Rhenium at high temperature which is the key physical property in the development and the performance of the tool during the service.

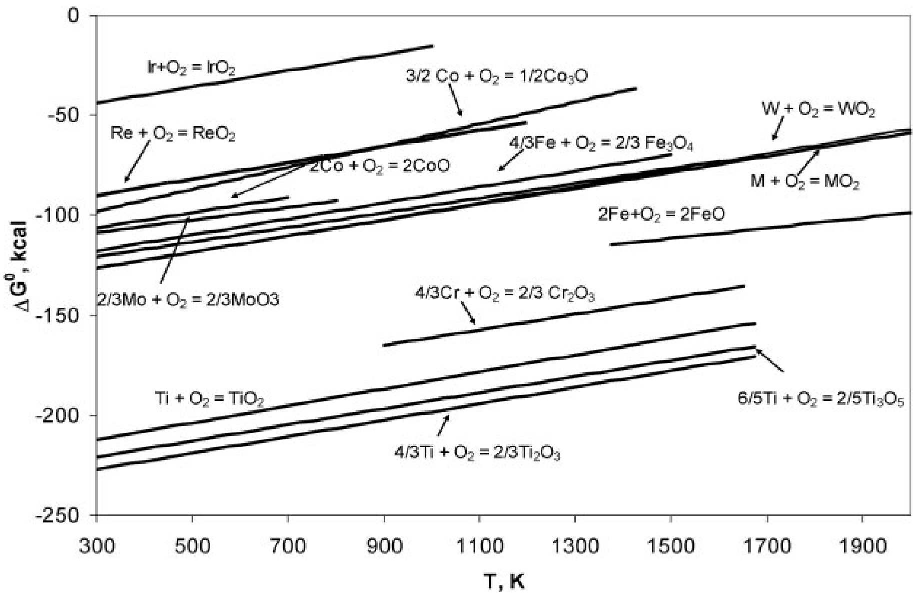

Figure 2-2 Ellingham diagram for some of metals used in FSW tools [12]

2.2 Tool geometry

Heat generation rate, torque and traverse force are affected by the tool geometry [12]. The flow of solid state stirred material is affected by the tool geometry as well as the linear and rotational motion of the FSW tool. Important factors in tool geometry are shoulder diameter, shoulder surface angle, pin geometry etc. The shoulder produces most of the heat and its grip on the solid state stirred or plastically deformed materials largely affect the flow field. Both sliding and sticking generate heat. The material must be adequately softened, the tool must have adequate grip on the stirred material. Triangular pins with concave shoulders provide high strength weld. The shape of the tool probe affects the flow of plasticized material. Tool shoulder influences the bulk material flow whereas the pin aided a layer by layer material flow. Figure 2-3 shows the shapes of some of the commonly used tool pins. A triangular or ‘trifluted’ tool pin enhances the material flow as compared with a cylindrical pin. The axial force on the material is influenced by the orientation of threads on the pin surface.

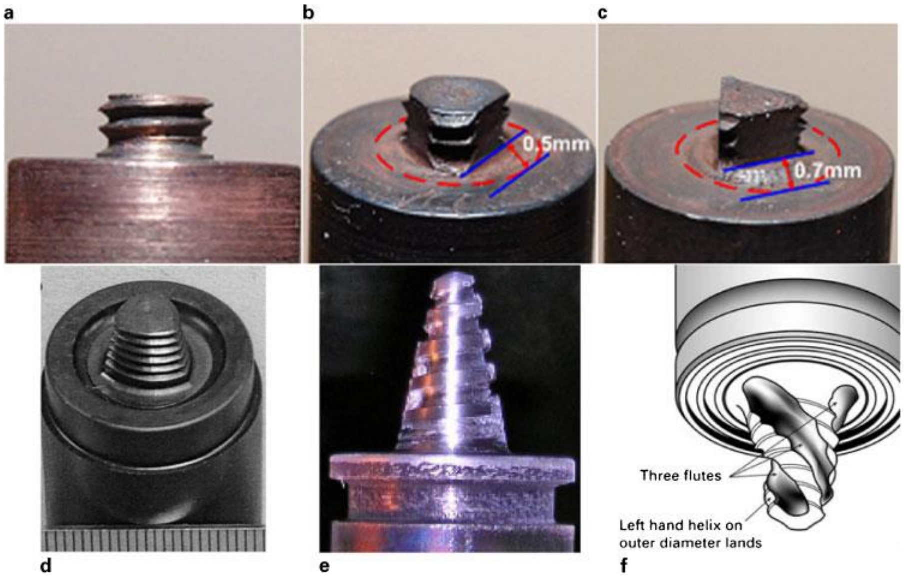

Figure 2-3 Commonly used tool pin geometries [12]

2.3 Synthesis of FSW tool materials

Synthesis of the tool materials play an important role in gauging -6the performance of the tool under sever conditions of friction stir welding of steel. Many research investigated the development of tool materials by various processing routes. Table 2-1 provides a comparison of mechanical alloying and sintering parameters for different tungsten base composites mainly consolidated by spark plasma techniques whereas Table 2-2 shows some other techniques used for the consolidation of tungsten base alloys and composites.

Table 2-1 List of tungsten base materials synthesized by various techniques

System	Temp. ºC	Sinter time min	technique	Ref.
Pure tungsten	1800	0-15	Plasma	[20]
W-25Re	2400	180	Cold press	[21]
W-Cu	-	-	-	[22]
W-7Ni-0.1Y_2O_3	1500	30 min	Cold press	[23]
W-B_4C	1700	-	Cold press	[24]
W-1%Y_2O_3	1200	3-5	SPS	[25]
W-5Y_2O_3	1700	3	SPS	[26]
W-30vol% HfC	1850	-	SPS	[27]
WC-10wt% Co	1200	12	SPS	[28]

Table 2-2 List of tungsten base composites synthesized by various techniques

parameters	Temperature ºC	Time min	Technique	Ref
W-3.6Re-0.26HfC	-	-	Arc Melted	[29]
W-3.6Re-0.3.5HfC	-	-	Arc Melted	[30]
W-4Re-0.32HfC	-	-	Arc Melted	[31]
W-1.5HfC	1800	4hrs	HIP	[32]
90W–7Ni–3Fe	1500	30	MW	[33]

E.Y. Ivanov et al [21] investigated the synthesis of nanocrystalline tungsten–rhenium alloy by mechanical alloying. They found that mechanical alloying of a W–25 wt. % Re powder mixture for 14hr in a high energy mill led to the development of nanocrystalline W–Re alloy. Jonathan et al [22] investigated the effect of temperature and holding time on the relative density of W-25%Re mixture during spark plasma sintering and it was found that with the increase of temperature and hold time, the relative density decreases as shown in Figure 2-4. This is attributed to the diffusion of carbon from graphite dies.

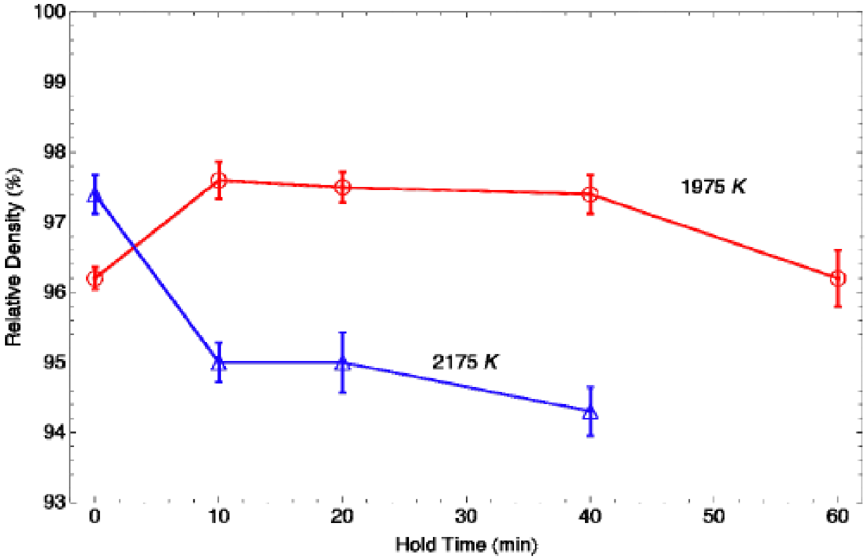

Figure 2-4 SPS of W-25%Re as a function of time and temperature [32]

M.A Yar et al [26] synthesized Nano-crystalline W-1%Y_2O_3 powder by a modified solution chemical reaction of ammonium paratungstate (APT) and yttrium nitrate. Spark plasma sintering (SPS) was used to consolidate the powder at 1100 and 1200 °C for various holding times. It was found that dispersion of yttrium oxide enhanced the sinterability of W powder as compared to lanthanum oxide. Park et al [29] synthesized dense, ultrafine WC-10 wt.%Co tool materials by SPS and shaped the tool to perform FSW on steel. They also investigated the mechanical and microstructural investigation of the tool as well as steel. Luo et al [30] investigated the mechanical properties of W-3.6Re-.26HfC composite at 1700-2980K and found that HfC play very important role in strengthening the alloy up to 2960 K due its outstanding thermal stability at very high temperature. Mingqui et al [31] studied the growth behavior of HfC dispersed in the W-Re matrix and investigated the effect of its dispersion on the strength of the alloy at temperature above 2200K and they found that from 2200 K to 2600K there was little growth of HfC with very slow growth rate. Rapid growth occurs after 2600K due to enhanced diffusion along the grain boundaries. John et al [32]studied the high temperature creep behavior of tungsten-4 wt%

rhenium-0.32 wt% hafnium carbide at temperatures ranging from 2200 to 2400 K at 40-70MPa. The stress exponent for secondary stage creep was 5.2. Activation energy for this stage was found to be 594 kJ/mol. Rea et al [33] consolidated the W-1.3wt% HfC by hot isostatic pressing. High resolution transmission electron microscopy (HRTEM) of the consolidated sample is indicated the uniform dispersion of nanosize HfC in the tungsten matrix.

Anhua et al [36] presented the effects of rhenium concentration on the strength properties of the W-Re-ThO_2 alloys at high temperatures and the yield strength of the alloys decreased with increasing temperature due to strengthening effect of Re in the system. Liu et al [37] investigated the effect of micro-size(0.2% Zr) alloying and nano-sized (1% Y_2O_3) oxide dispersion in tungsten and then sintered by SPS. Oxygen at W grain boundaries reacts with Zr to form zirconia.

S.K. Rakhunathan et al [38] studied the high energy and high rate consolidation of W and W based composites. The pure tungsten compact exhibited a ductile failure of the infiltered copper matrix. Z. Zak Fang et al [39] reviewed the synthesis, sintering, and mechanical properties of nanocrystalline cemented tungsten carbide. They also discuss the effect of addition of grain growth inhibitor such as VC on the grain size. They reported that there was almost no grain growth upto 1100^oC and addition of VC inhibits the grain growth at higher temperatures.

David et al [40] studied the dislocation density as a result of implantation of ions on W-Re ions. Increase in hardness measured by nanoindentation was attributed to the interaction between irradiation loop and dislocations. Dongju et al [42] investigated the effect of milling and sintering on the phases of HfC-W composite. This class of composite was spark plasma sintered at 1800^{o}C. Ozherelyev et al [41] discussed the X-Ray Diffraction studies of Hf-W alloys. They found that with the increase of tungsten contents, positions of the peaks shift from right to left suggesting solid solution formation.

2.4 Characterization of FSW welded microstructure

Shuaib et al [18] reported the results of friction stir welding of tube-tubesheet joints made of steel. Void defects were reported at the root of some welded regions. Larger voids were observed at the joints having holes without chamfers compared to those with holes with chamfers. Chung et [51] conducted a study of FSW (WC tool) for high carbon steel below and above eutectoid temperature. These authors reported the presence of a mixture of pearlite and cementite structure present below A1 (A1 temperature below which there will be no phase transformation) whereas all other conditions show martensite plus pearlite structure. In this investigation it was found that below A1 with 100 mm/min welding speed and 100 rpm rotation speed, the microstructure is totally pearlite and cementite whereas when conditions were changed to 200mm/min and 400 rpm the microstructures at locations of joints were different at the top 65% was the martensite which decreases to 20% at the bottom.

B.W Ahn et [44] investigated the FSW of 409L SS by using a silicon nitride tool. The base metal (BM) has hot rolled ferrite grain structure and stir zone (SZ) had an equiaxed ferrite grain structure with a diameter of approximately 50 µm. The equiaxed grain size was formed due dynamic recrystallization. Meshram et al [45] investigated the mechanical behavior of friction stir welding of stainless steel performed by PCBN pin tool. The base metal was found to have 608MPa UTS whereas Friction stir welded sample showed 630 MPa. The weld behaved almost similar to base metal. Konkol et al [46] compared the

Friction Stir Welding and Submerged Arc Welding of HSLA-65 Steel. The welding of the 3m length of HSLA-65 with the refractory alloy tool was done successfully. The W-Re pin showed almost no wear or change in length at the completion of the weld.

Zafar et al [47] investigated the effect of friction stir welding parameters on the weld microstructure of mild steel using a W-25%Re pin tool. The effect of tool travel speed on bead surface finish as well as bead width can be observed from Figure 2-5 where the weld bead is superimposed on the load profiles of the pin tool. In the first 30 mm length of the bead, the tool was traveling at 15 mm/min zone (A). Toward the end of zone (A), two surface defects or discontinuities, marked by dashed circles, developed, which caused an increase in the magnitude of the axial welding force.

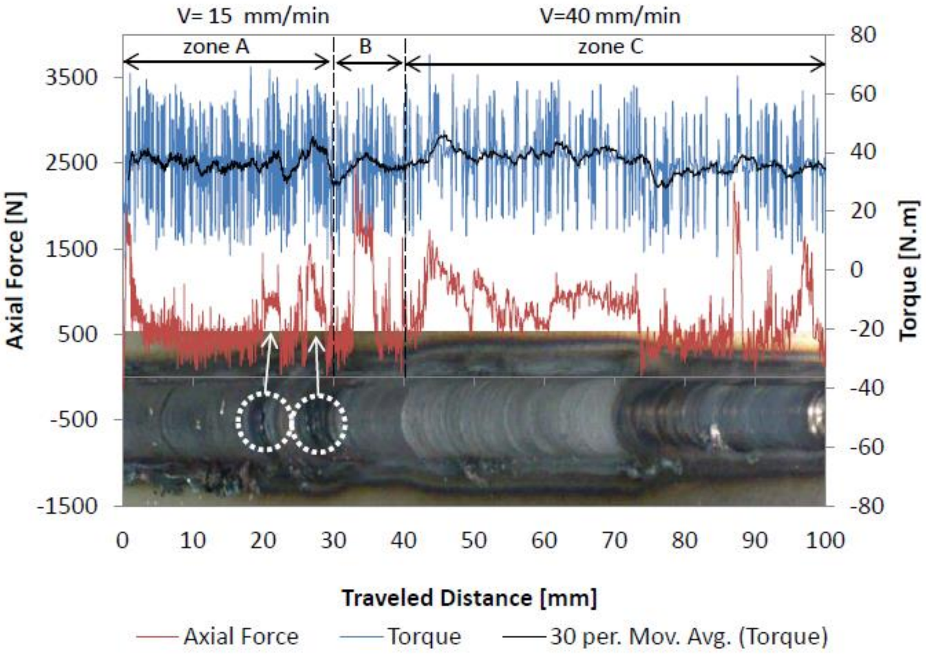

Figure 2-5 Weld bead quality along traveled distance at 2000 rpm 44]

Buffa et al [48] investigated a quantitative analysis of the tool life in FSW of 3 mm thick Ti-6V-4Al titanium alloy sheets by using W-25%Re tool and found it successful in welding the alloy. Lienert et al [54] studied the FSW for joining of mild steel by characterizing the process of friction stir welds on mild steel by using refractory tools. Park et al [29] synthesized dense, ultrafine WC-10 wt. %Co tool materials by SPS and shaped the tool to perform FSW on steel. This tool was used to friction stir weld the low carbon steel sheet of thickness 2 mm. No visible defects were present in the nugget of weld. Stir zone is the region where base material comes in direct contact with the tool and Heat affected zone is the region where grain growth can be found.

2.5 Tool wear, deformation and failure

FSW tool wear occurs when it passes through the workpiece. The reduction in yield strength of tool may happen due to high load application and elevated temperature generated during the FSW of harder metal and alloys such as steel and titanium alloys. Wear of the tool can be due to abrasion, adhesion or diffusion. Due to the involvement of high temperature, diffusional wear can play a vital role in the tool wear. From thermodynamic point of view, Ellingham diagram can help to find out relative ability of oxidation at elevated temperature for such metallic tools. In most of the cases, tool failures are related to pin rather than shoulder as pin has to face more resistance to motion when immersed in the workpiece. Moreover, the pin has lower load bearing capability when compared to shoulder part which results in higher torsional and bending stresses in the former. Steel and titanium alloys were recently friction stir welded by W–Re alloy tool as discussed earlier[12]. Although PCBN is being used on commercial scale, W–25wt-%Re alloy was recommended by different authors for its greater ductility compared to PCBN. Boron from PCBN may be dissolved in the base metal making it more prone to brittle failure. Moreover, the PCBN tool pin is more susceptible to fracture at higher speed or loads.

Thompson et al evaluated the diffusional wear of three different Tungsten base tool with same geometry for the FSW of steel and titanium alloys [111]. They found that Tungsten -Titanium workpiece cross diffusion was more rapid than Tungsten-steel cross diffusion. However, microstructural investigation showed that tungsten from the tool was diffused into the steel. They also reported that W-Re and W-Re-HfC tools showed minimal tool degradation. Barnes et al [112] investigated the effect of tool material on developed microstructure in FS welded HSLA-65 steel. The authors compared the performance of PNCB to W-25%Re, and they found that excessive level of abrasive wear occurred on the W-Re tool as compared with PNCB tool, and it found to be increasing with tool temperature.

The FSW tool failures are mainly attributed to diffusion and wears. Ellingham diagram shown in Figure 2-2, provides information about the regions of stability of oxide formation at high temperature. Figure 2-6 shows oil hardened steel tool used in friction stir welding of Al6061-20vol%Al2O3 [12] composite. It was noted that wear rate decreases (due to second phase hard particles) after the initial wear.

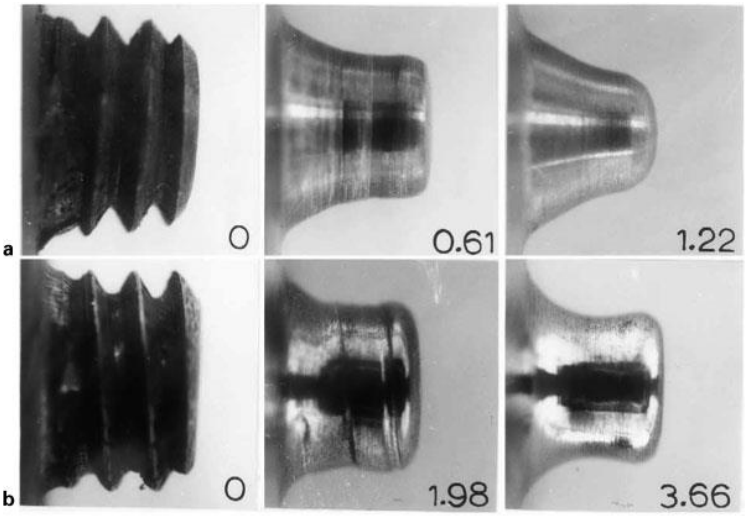

Figure 2-6 Wear of oil hardened steel tool at (a) 3 mm s^{-1} and (b) 9 mm s^{-1} [12]

From the literature review, it can be inferred that W-25%Re alloy is a potential tool candidate for the FSW of high melting point materials but so for this class of materials is only being developed by conventional techniques such casting or extrusion. These techniques will result in grain growth during synthesis which will impair the mechanical properties of these very important materials. In order to make stronger and harder W-Re alloy and composite tool, novel processing techniques such as mechanical alloying and spark plasma sintering must be employed which can retain the nano features of the developed powder and ultimately provides a new advanced route for the development of the tool for the FSW of harder metals and alloys.

CHAPTER 3

SYNTHESIS AND CHARACTERIZATION OF W-25Re POWDERS

Based on the literature review as presented in chapter 2, W-25%Re alloy was chosen as the best suitable candidate for the development of the tool. This chapter deals with the synthesis and characterization of W-25wt%Re alloy and W-25wt%Re + Xvol%HfC composites powders synthesized by mechanical alloying.

3.1 Materials & method

Semi-alloyed W-25-wt. %Re and HfC powders supplied by Rhenium Alloys, USA, were used in this investigation. Nanostructured W-25Re alloy and homogenous W-25Re-HfC composites containing 5 and 10 vol. % of HfC particles were produced using MA. The experiments were carried out in a planetary ball mill (Fritsch Pulverisette, P5, Idar-Oberstein, Germany). Since the use of steel vials and balls introduces Fe contamination [69], tungsten carbide vials (250 mL in volume) and balls (10 mm in diameter) were used to avoid contamination of the powders [70]. Milling was performed in argon inert gas to avoid oxidation of the powders. In the first stage, the as-received and semi-alloyed W-25-wt. %Re powder was milled for 5, 10, 15, and 25h until a single nanostructured solid solution was obtained. Milling conditions of ball-to-powder weight ratio of 8:1 and speed of 250 rpm were used.

In the second stage, HfC particles (5 and 10 vol. %) were dispersed in the obtained nanostructured alloy powder using milling conditions of a speed of 150 RPM, a ball to-powder weight ratio of 5:1, and a milling time up to 15 h. A summary of the parameters used in the investigation is shown in Table 3-1

Table 3-1 Mechanical alloying and milling parameters

Powder composition	Time (hrs)	Speed (RPM)	BPR
Semi-alloy W-5%Re	5, 10, 15 & 25	250	8:1
Fully alloyed W-25%Re +5vol%HfC	5,10 & 15	150	5:1
Fully alloyed W-25%Re +10vol%HfC	5,10 & 15	150	5:1

Field Emission Scanning Electron Microscope (FE-SEM), Tescan Lyra-3, equipped with Energy Dispersive x-ray Spectroscopy (EDS) was used to analyze the as received powders, and mechanically alloyed powders. The dispersion of HfC particles in the synthesized powders was characterized using FE-SEM and x-ray mapping using 20 frames. X-ray diffraction experiments were carried out using a diffractometer (Bruker D8, USA, with a wavelength $\lambda = 0.15405$ nm) to characterize phases present in the samples and evaluate the crystallite size and lattice strain of the tungsten phase.

3.2 Characterization of as-received powders

3.2.1. Particles size analysis

As-received powders were characterized for particle size analysis by particle size analyzer. It was found that both the powders were in the sub-micronmeter size as shown in Figure 3-1 and Figure 3-2 respectively. The result shows that partially alloyed W-25%Re powder was in the early stages of milling.

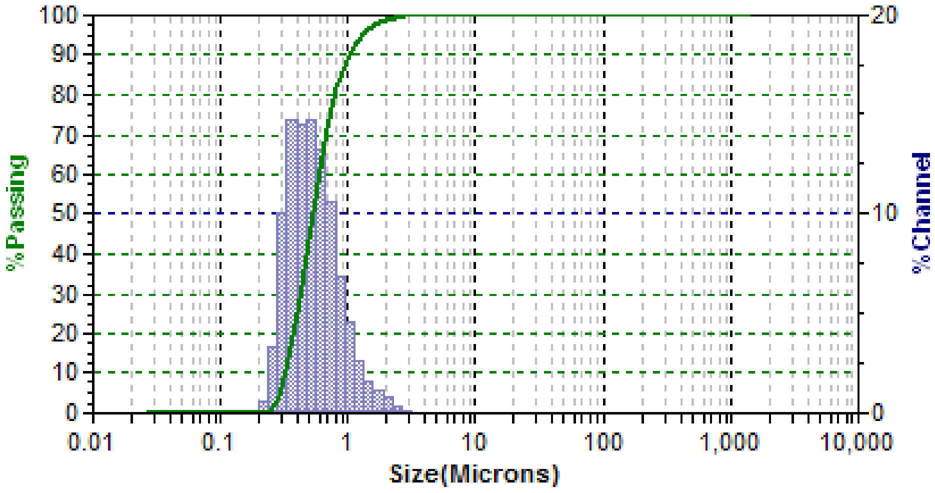

Figure 3-1 Particle size analysis of W-25%Re as-received

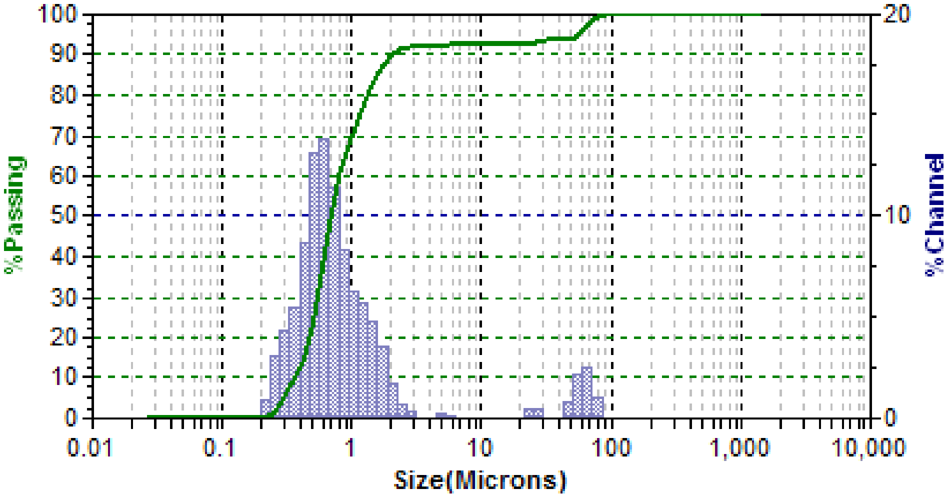

Figure 3-2Particle size analysis of HfC

3.2.2. Field Emission-SEM and XRD pattern of HfC

FE-SEM image of HfC powder is presented in Figure 3-3 (a). The particles have sub-micron size and various shapes ranging from elongated to irregular. Figure 3-3 (b) shows XRD pattern of HfC powder, the compound has a cubic crystal structure of the NaCl type.

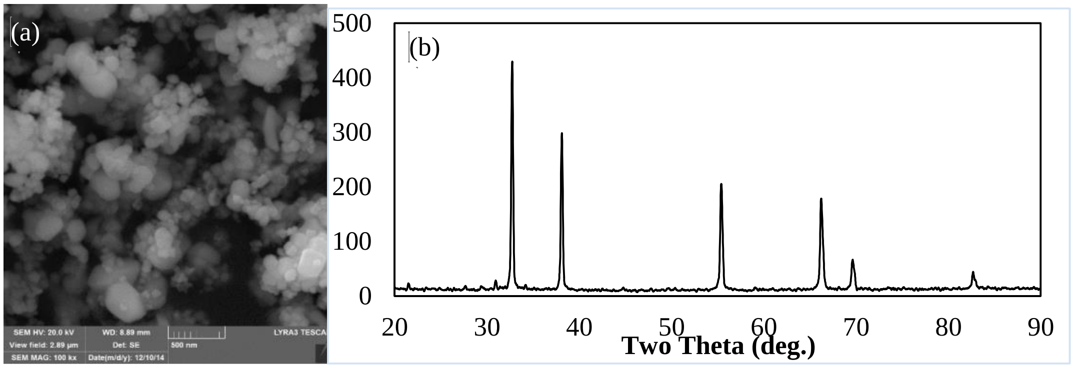

Figure 3-3 (a) FE-SEM image and (b) XRD spectrum of HfC powder

3.3 Characterization of mechanically alloyed powder

3.3.1 FE-SEM analysis of synthesized alloyed powder

The as-received semi-alloyed W-25wt%Re powder was synthesized by mechanical alloying of W and Re pure powders; a FE-SEM image showing the morphology of its particles is presented in Figure 3-4 (a). It is known that in the course of mechanical alloying particles undergo flattening, cold welding, fracturing, and rewelding. In early stage of milling, plastic deformation and cold welding dominate and leads to change in particle shape and increase in particle size, respectively [71][72]. As can be noticed, in Figure 3-4 (a), some particles have flattened shape and large particle size while others are more equiaxed and have small particle size. Since the as received W-25wt%Re powder was not fully alloyed, it was further milled for different milling times up to 25 h to achieve complete solubility and obtain a nanostructured solid solution.

Mechanical alloying of the powder for 5 hours decreased the particle size and transformed the shape of particles from flattened to equiaxed, Figure 3-4 (b) at low magnification and Figure 3-5 (b) at high magnification. With the increase in milling time to 15 and 25 hours, the ability of the particles to strain harden decreases. Therefore, fracturing of particles became significant and leads to a decrease in particle size, Figure 3-4(c, d) at low magnification and Figure 3-5(c, d) at high magnification. This is in agreement with published work [70], where it was reported that mechanical alloying of W-25%Re powder mixture starting from W and Re particles with 10 and 30 μm in size deceased the particle size and led to the formation of rounded powder particles.

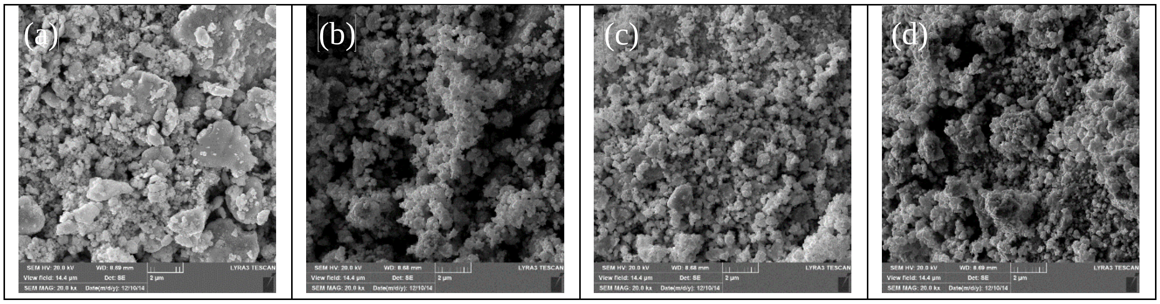

Figure 3-4 FE-SEM images of alloyed W-25wt%Re powder at low magnification

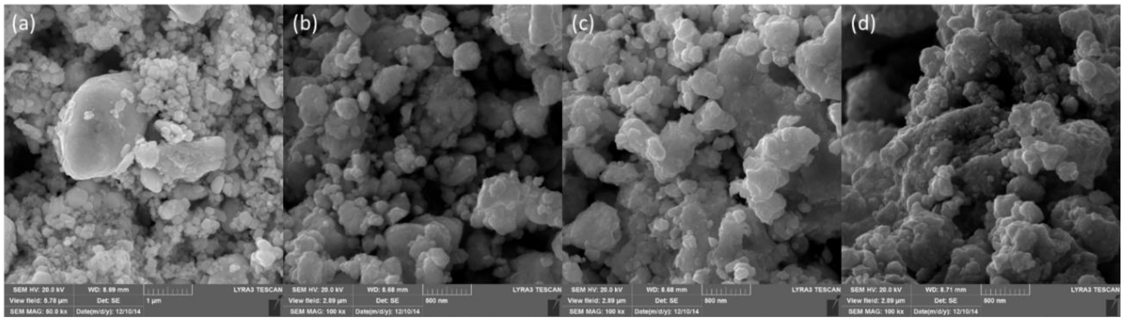

Figure 3-5 FE-SEM images of alloyed W-25wt%Re powder at high magnification.

3.3.2 XRD analysis of synthesized alloyed powder

XRD spectra of W-25wt%Re powder, mechanically alloyed for different times, are shown in Figure 3-6 (a). Analysis of XRD spectrum of the as-received W-25wt%Re powder, confirmed that it has body centered cubic crystal structure. XRD pattern has reflections both from W (bcc, a = 0.3167 nm) and Re (hcp, a= 0.2781 nm). A peak characteristic of rhenium is present along with W-Re solid solution peaks. This indicates that rhenium is not completely dissolved in tungsten. XRD spectra of W-25wt%Re powder milled for 5, 10, and 15 hours, presented in Figure 3-6(a), shows that the peak characteristic of rhenium is still present but its intensity decreased. However, with the increase of milling time to 25 h, this peak disappeared and only W-Re solid solution peaks are present. This indicates complete solubility of rhenium in tungsten and formation of a single solid solution.

The peak positions was slightly shifted indicating the solid solution formation due to inter-diffusions of these two elements. Peaks of W shifted towards lower 2 theta values indicating decrease of lattice parameters. The atomic radius of W (r_w =0.1408 nm) is greater than Re (r_{Re}=0.1375) which results in shifting toward higher 2 theta values. Peak broadening was observed in the later stages due to reduction in crystallite size. The equilibrium maximum solid solubility limit of Re in tungsten was reported to be between 24 to 37 % Re depending on the preparation method [73][74][75]. Beyond this solubility, the σ phase precipitates and leads to failure of the alloys [70]. In this work, the W-25wt%Re solid solution was obtained by MA and formation of the σ phase was not revealed. It was reported that MA could lead to the formation of stable and metastable phases including solid solutions [76][77]. The technique was used to synthesize W–25% Re single-phase solid solution using steel vial and with steel grinding medium [78] and tungsten carbide vials and balls [70].

Mechanical alloying decreased the intensity of the W-Re solid solution peaks. This decrease was accompanied with broadening of the peaks. This is due to the fact that mechanical milling of metallic powders is usually associated with a decrease in crystallite size and increase in lattice strain [79]. The XRD data of mechanically alloyed W-25%Re powder was used to calculate the crystallite size and lattice strain as reported elsewhere[80]. Figure 3-6b) shows crystallite size change of the tungsten phase as function of milling time. The as-received and partially alloyed powder has a crystallite size of 188 nm. Milling of the powder for 5 hours decreased the crystallite size to 68 nm. A further increase in milling time to 10 and 15 h led a decrease in crystallite size to 28 and 23 nm, respectively. Equation 1 relates the crystallite size D with the peak broadening β and wavelength of x-ray used λ. The value of K is usually taken as 0.9.

$$\beta_{hkl} = \frac{K\lambda}{D} + 4\varepsilon \sin\theta$$ **Equation 3.1**

A final crystallite size of 13 nm was obtained with the increase in milling time to 25 h. The decrease in crystallite size is believed to take place in three stages. Formation of large number of dislocations within shear bands, in the first stage. Recombination of these dislocations leads to the formation of small angle grain boundaries, in the second stage. Finally, the orientation of the formed grains become random, in the third stage [80]. In XRD analysis, the crystallite size usually refers to the size of very small grains (sub-grains) that leads to broadening of the peak [79].

It is evident from Figure 3-6 (b) that the major reduction in crystallite size of the W-Re solid solution took place in the first 10 h. The increase in milling time beyond 10 h only led to very small change in crystallite size. This behavior is possible in MA because the smaller grains get saturated with defects and dislocation pile-ups and, hence, the structure cannot continue to develop the same way as in large-grained metals [81]. Therefore, once the nanocrystalline structure is fully developed, further decrease in crystallite size become very difficult because of the large stress needed to deform the nano-grains. Under these conditions, creation and motion of dislocations become difficult, and the structure will continue to deform by grain boundary sliding mechanism.

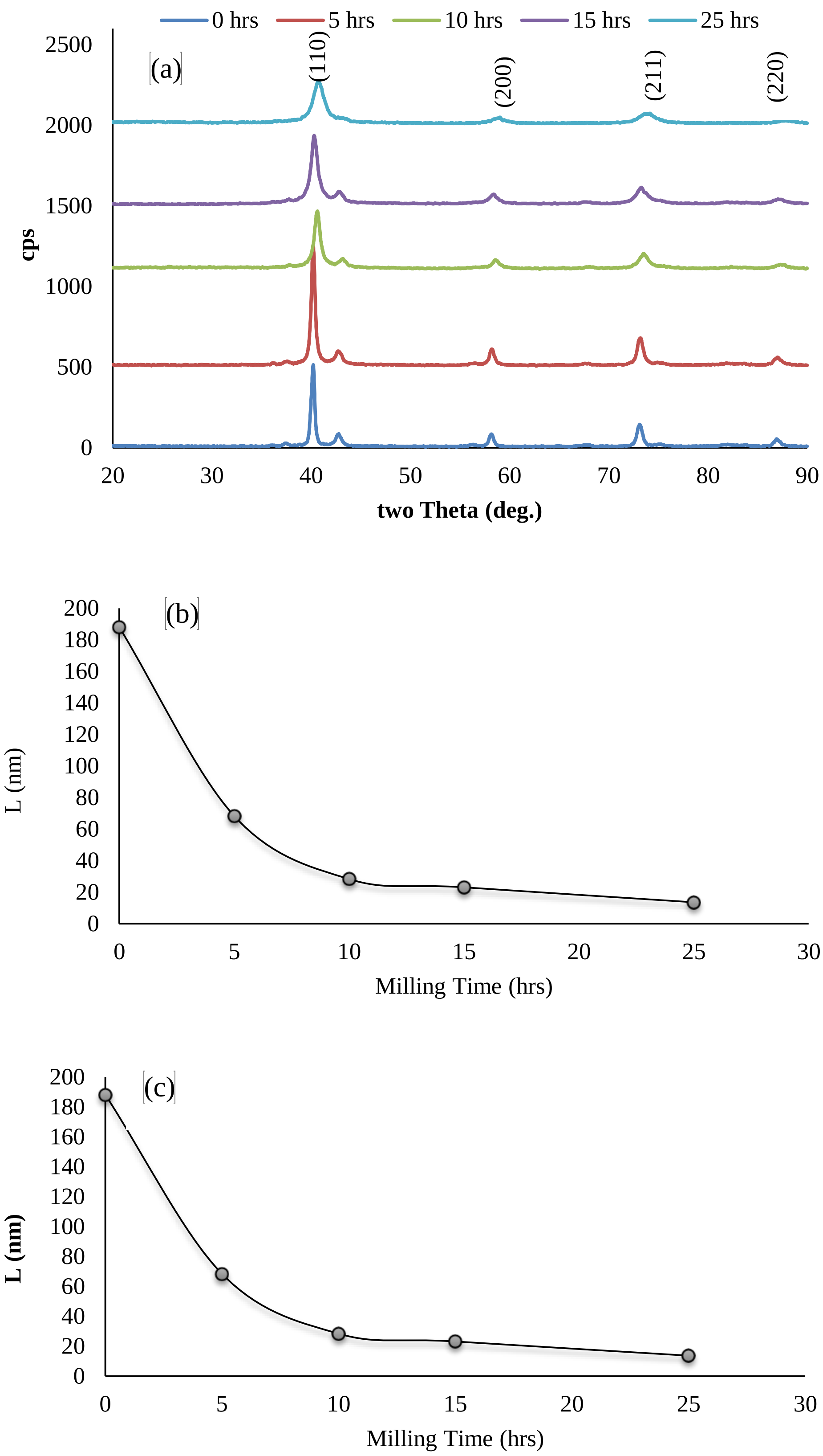

Figure 3-6 alloyed W-25%Re powder (a) XRD (b) crystallite size and (c) lattice strain.

On the other hand, grain size reduction may be hindered by recovery [82]. However, mechanical alloying time was extended to 25 h to have complete solubility of Re in W. Mechanical alloying not only decreased the particle size and crystallite size but also increased lattice strain in the tungsten phase as presented in Figure 3-6c). During mechanical alloying, particles experience heavy plastic deformation, which increases dislocation density and leads to an increase in lattice strain.

3.3.3 FE-SEM analysis of the milled composite powders

The W-25%Re alloy powder milled for 25 h was mixed with HfC particles (5 and 10 vol. %) and further milled for different milling times up to 15 h. Figure 3-7 shows FESEM images of W-25wt%Re-5HfC and W-25wt%Re-10HfC composite powders mechanically alloyed for 15h. Since the W-25wt%Re matrix alloy powder was milled for 25 h to obtain a nanostructured single solid solution, as presented in Figure 3-4d), further milling of the composite powders did not bring about significant change in the powders' particle shape and size. Elemental mapping of Hf and C in the composite powders mechanically milled for 5 and 10 h revealed that HfC particles remained relatively agglomerated as shown in Figure 3-8 (a, b) containing 5vol.%HfC and Figure 3-9 (a, b) containing 10vol.%HfC respectively. However, homogenous composite powders with uniform distribution of HfC particles was obtained with the increase in milling time to 15 h as it can be seen in typical x-ray mapping of Hf and C, in the composite containing 5 vol.% of HfC and 10vol.%HfC, presented in Figure 3-8 (c) and Figure 3-9(c) respectively.

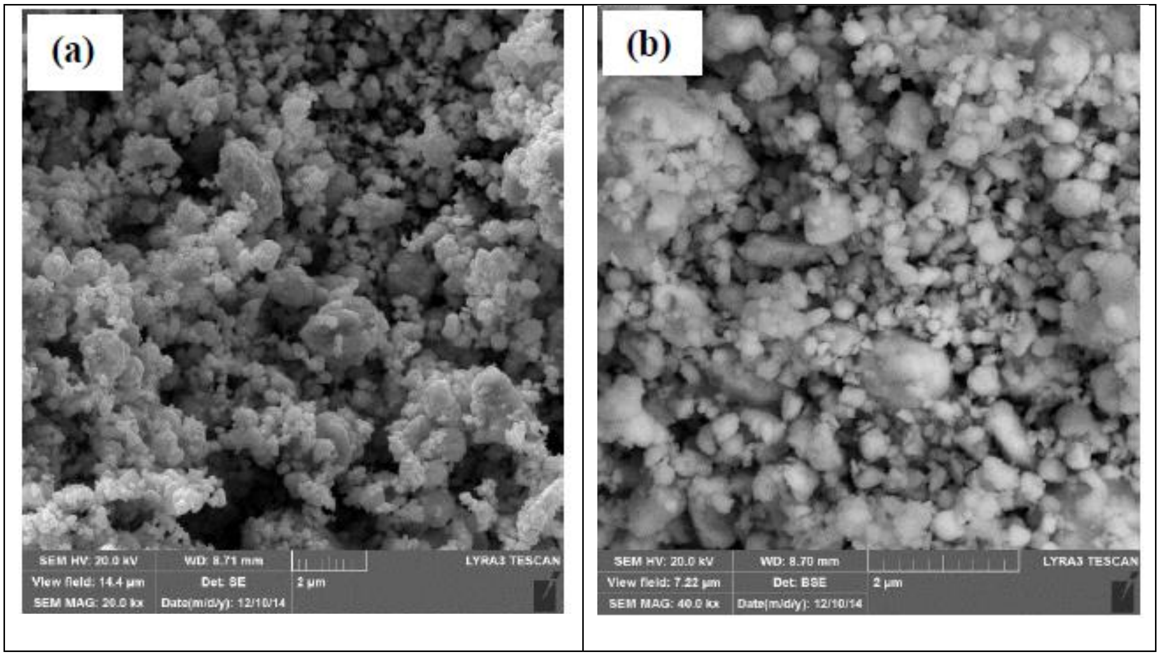

Figure 3-7 FE-SEM of 15hrs milled composite powders (a) 5% (b) 10% HfC

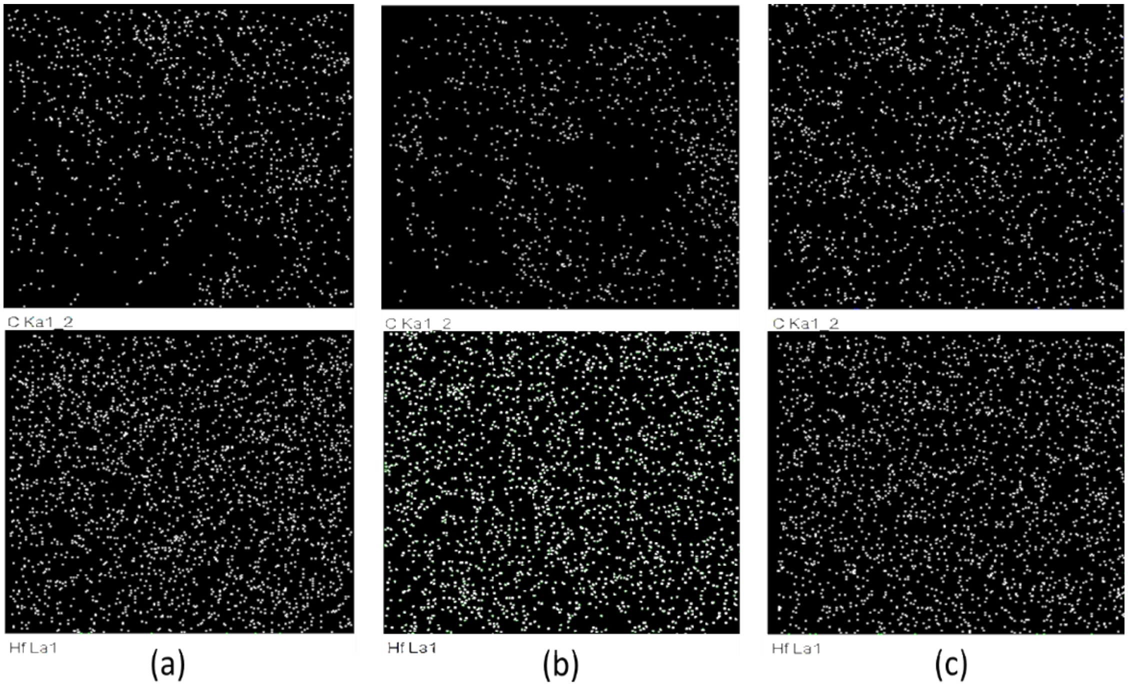

Figure 3-8 X-ray mapping of 5%HfC for (a) 5h (b) 10 and (c) 15 h.

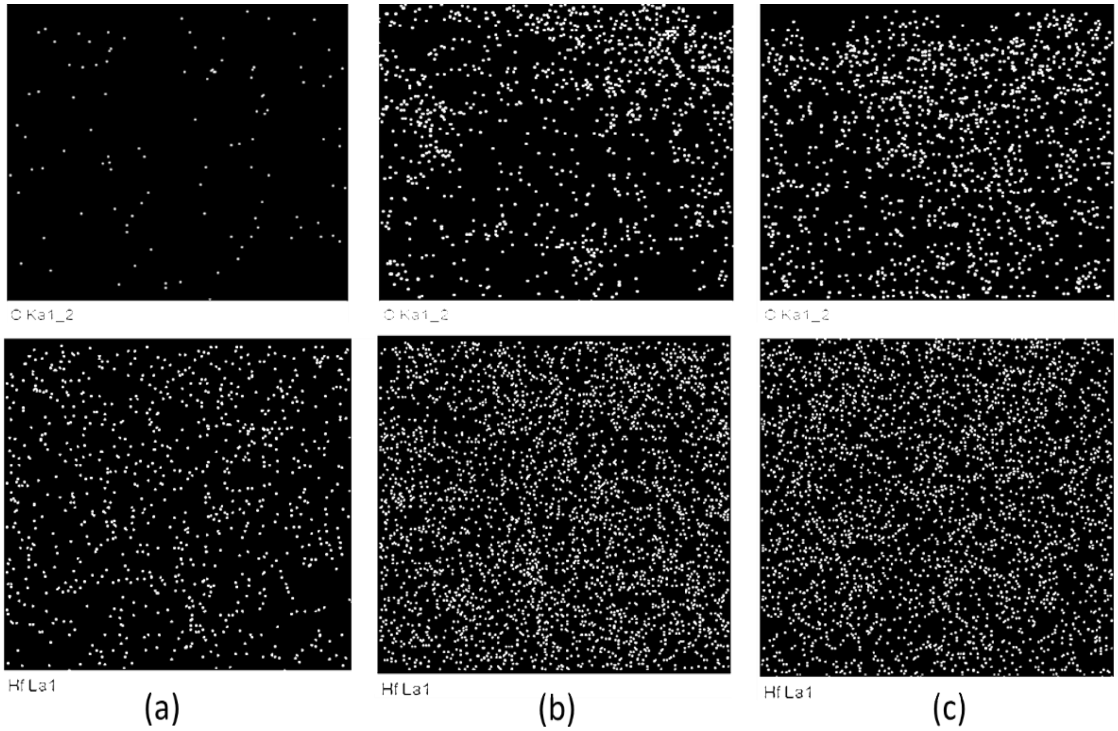

Figure 3-9 X-ray mapping of 10%HfC for (a) 5h (b) 10 and (c) 15 h.

3.3.4 XRD analysis of synthesized composite powders

Figure 3-10 shows the XRD patterns of the alloy and composites sample containing 5vol% HfC milled for different length of time. XRD pattern of monolithic W-25%Re alloy milled for 25hrs is presented in Figure 3-10a) whereas the composite containing W-25%Re + 5vol% HfC milled for 5 h and 15 h is presented in Figure 3-10b) and c) respectively. As the milling for the synthesis of composites were performed by using a ball-to-powder ratio of 5:1 with a speed of 150rpm, it did not result in the crystallite size reduction as evident from the broadening of the peaks. There is almost no broadening of peaks which confirms that the objective of uniformly distributing of second phase HfC was achieved without introducing strains in the composite powder.

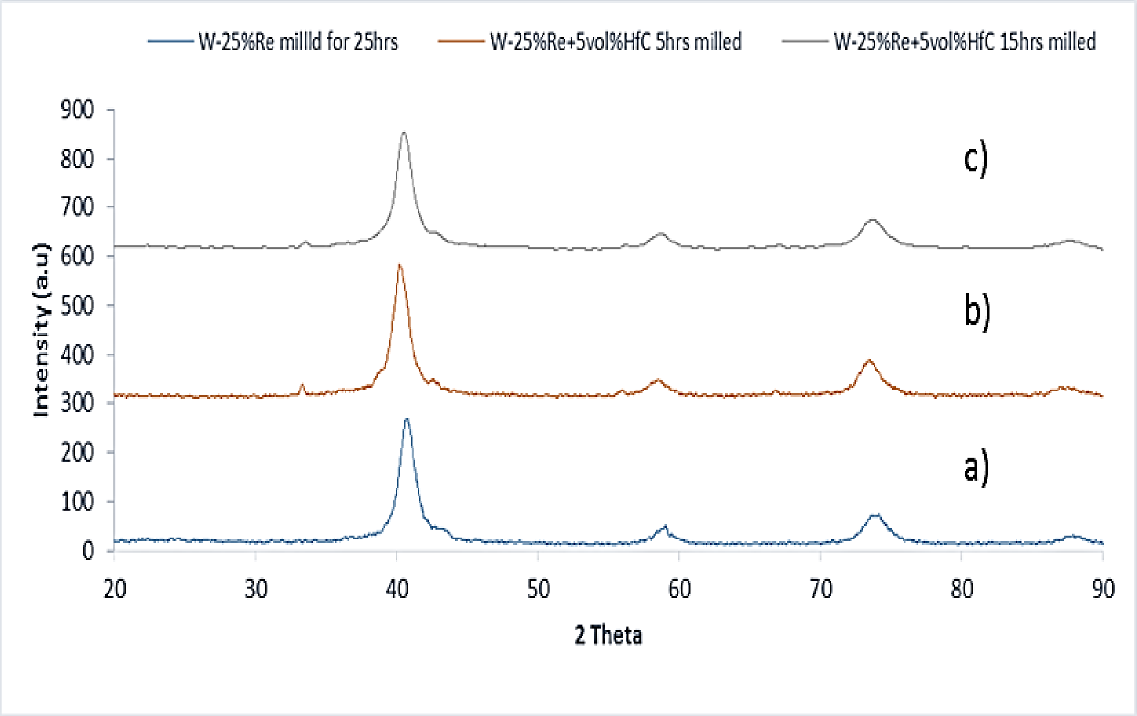

Figure 3-10 XRD (a) alloy 25h (b) 5%HfC, 5h (c) 5%HfC, 15h.

CHAPTER 4

DEVELOPMENT AND CHARACTERIZATION OF EXPERIMENTAL TOOL

This chapter deals with the consolidation of milled powders (developed previously as discussed in chapter 3) into cylindrical discs by using SPS. Spark plasma sintered specimens were characterized by metallography, field emission scanning electron Microscopy, X-ray Diffraction technique, microhardness, density determination by Archimedes and thermal conductivity. Later on, wear analysis was performed on these discs and wear morphology was studied by FESEM and optical profilometer.

4.1 Methodology

The prepared powders were consolidated using SPS equipment (FCT system, Germany), model HP D 5. More details on the SPS process were reported elsewhere [17]. Disc shaped specimens having 10 mm radius were produced with the help of a graphite die. A thermocouple was inserted through a drilled hole near the graphite die to record the temperature during the sintering process. In order to reduce the friction between the specimen powder and wall of the die, a graphite sheet was placed between them.

Compaction pressure of 50 MPa and heating rate of 100ºC /min were used in all sintering experiments. The nanostructured W-25-wt.%Re alloy powder (milled for 25h) was sintered at temperatures of 1500, 1700, and 1800ºC for 10 minutes, to determine the suitable sintering temperature; then the as-received W-25-wt.%Re powder and composites containing 5 and 10 vol.% HfC were sintered at 1800ºC for 10 minutes. Longer duration and very high temperatures were avoided [65] in order to minimize the chances of diffusion of carbon in the sintered samples. Jonathan et al [65] investigated the effect of temperature and holding time on the relative density of W-25%Re mixture during spark plasma sintering and it was found that with the increase of temperature and hold time, the relative density decreases. This is attributed to the diffusion of carbon from graphite dies.

4.2 Characterization of consolidated specimens

4.2.1. Metallography of spark plasma sintered specimens

A Hewllet Packard power supply devise, model 6216, was used to etch sintered samples. The etching process was performed in one molar concentrated solution of NaOH for 3 seconds at a voltage of 5 Volt. Tungsten base alloys and composites are generally difficult to etch by conventional etchants. Metallography feasibility of W-25%Re-HfC sintered samples were investigated by using different etchants for revealing the grain boundaries. Murakami reagent (10 g KOH or NaOH, 10 g potassium ferricyanide, 100 mL water), Lactic acid+HNO3 and NaOH were initially used in this study. Finally, sintered samples were electrolytically etched in 1 M NaOH solution. The consolidated samples were characterized microstructurally by optical microscopy and FESEM.

Sintered samples were mounted, ground and polished. W-25%Re fully alloyed sintered at 1800^{0}C was etched for 1 to 15min in Murakami reagent. Etching results in the form of optical immages are shown in Figure 4-1. The sample did not show any evidence of etching. Lactic acid+HNO3 was subsequently utilized for the same duration but this etchant was also proved ineffective in revealing the grain boundaries. This sample was etched with NaOH and results of etching are shown in

Figure 4-2. The etchants reacted with the grain bounaries after 15 min but the etching process was still sluggish.

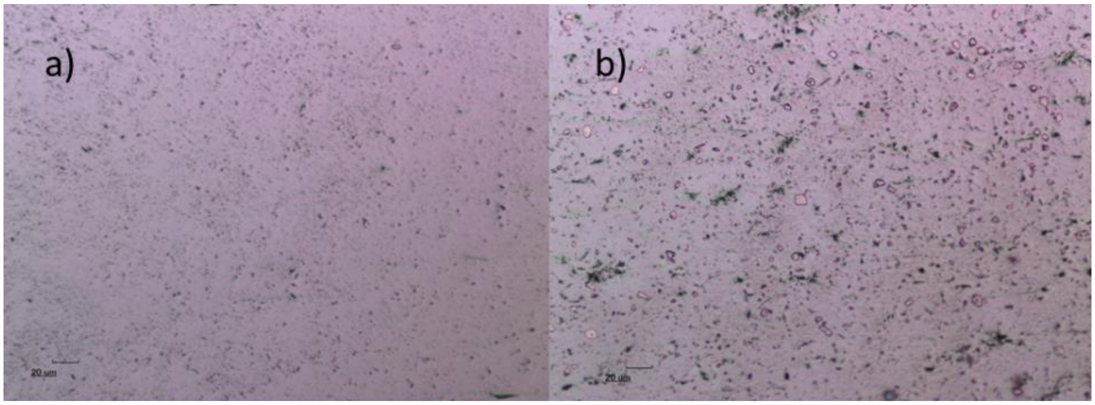

Figure 4-1 Optical images of etched W-25%Re using Murakami a) before b) 15min

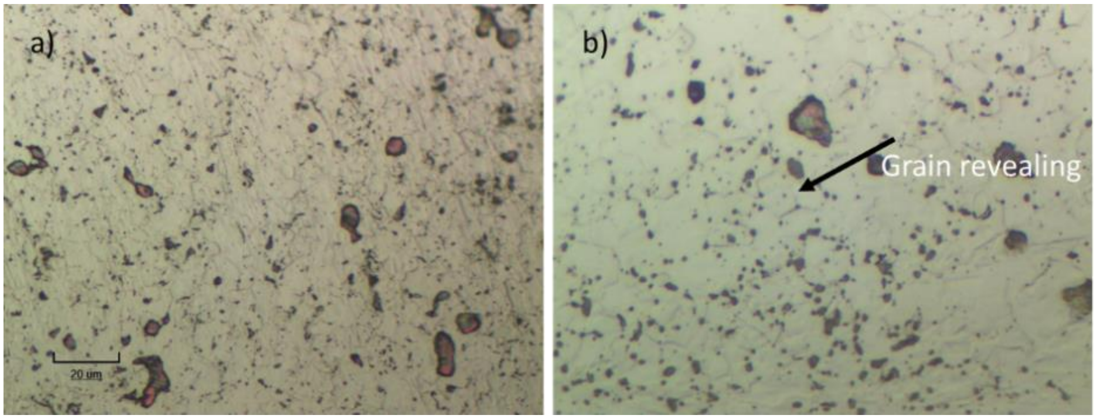

Figure 4-2 Optical images of etched W-25%Re using NaOH a) 3min b) 15min.

4.2.2. Electrolytic etching

After achieving some success in revealing grain boundaries, NaOH was chosen for further investigation. Since the etching was sluggish, electrolytic or electrochemical etching was preferred to accelerate the etching process.

FFigure 4-3 shows the setup for electrolytic etching. One molar concentrated solution of NaOH was prepared. The positive terminal of the low voltage direct current power supply was connected to the sample. The negative terminal was connected to a steel plate to make it cathode. Mounted samples were drilled small holes at the back to get connection and a screw was fitted in that hole. The screw touched the sample to make a secure connection. The sample was placed in the tank facing another plate which was attached to the cathode with a distance of 6 to 8 centimeters between them. Current flows from the sample to cathode resulting in the etching of the sample. The voltage was kept constant as 5 volt during the etching process. Specimens were etched for short time interval between 1 to 5 seconds and microstructural analysis was conducted after each etching step.

Figure 4-4 shows the electrolytically etched optical images of the monolithic W25% Re alloy sintered at 1800^{o}C. FESEM analysis of the samples conclude that optimized etching time was 3 seconds. Increasing time lead to over etching.

Figure 4-3 shows the electrolytic etching setup a) power supply b) etching setup

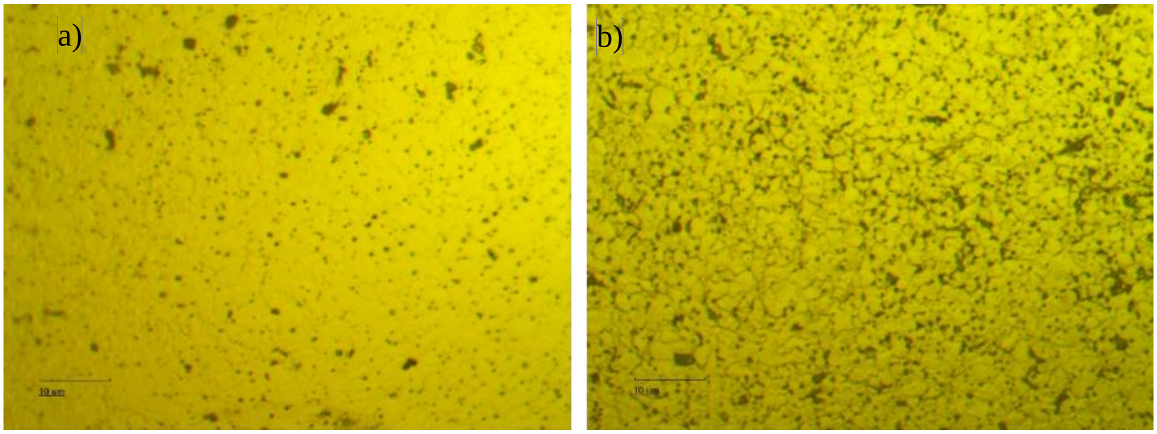

Figure 4-4 Optical images of the sintered alloy after a) 1second b) 3 seconds

4.2.3. FE-SEM analysis of SPSed specimens

Figure 4-5 shows the FE-SEM images of the W-25%Re sintered at 1800^{o}C etched for different times. Figure 4-5a) shows the FESEM image of the sample etched that was etched for 3 seconds to reveal the grain boundaries. As the time is increased, over etching happened as shown in Figure 4-5b) and c). A typical FE-SEM image of the microstructure of sample sintered at 1800^{o}C for 10 minutes is presented in Figure 4-5a).

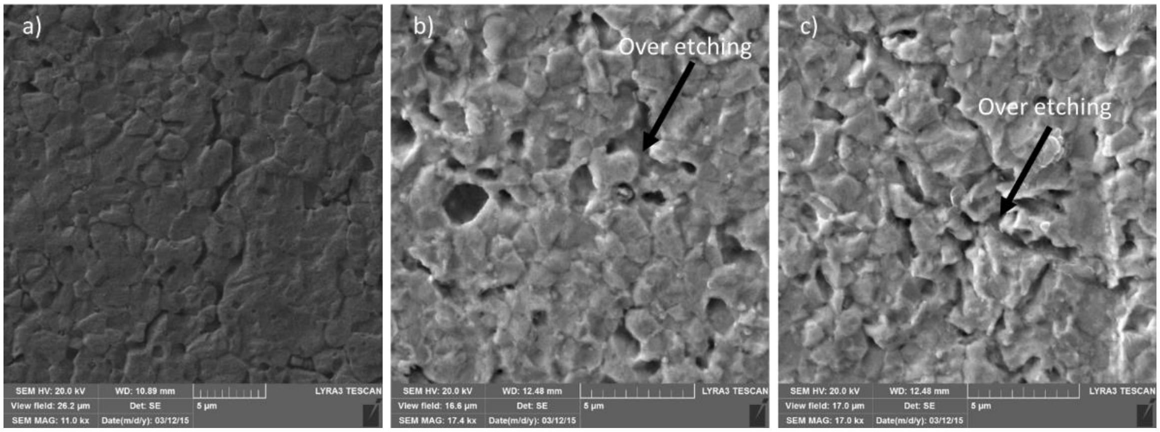

Figure 4-5 Effect of electrolytic etching time on the microstructure a) 3s b) 5s c) 7s

Figure 4-6 shows the FESEM images of the as-received pre-alloyed sample sintered at 1800^{o}C. Secondary Electron (SE) and Back SE images of the etched sample shows that average grain size is approximately 10 µm. For the composite containing 5vol%HfC, grain boundaries were revealed and HfC was found embedded in the matrix as shown in Figure 4-7. This study was carried out at relatively low temperature to achieve nanocrystalline matrix reinforced with HfC. The sintered nanocrystalline monolithic sample has an average grain size of 1-3um. Due to lower temperature and shorter sintering time, the composite and fully alloyed specimens will retain their nanocrystallinity which will be discussed in detail in later stages.

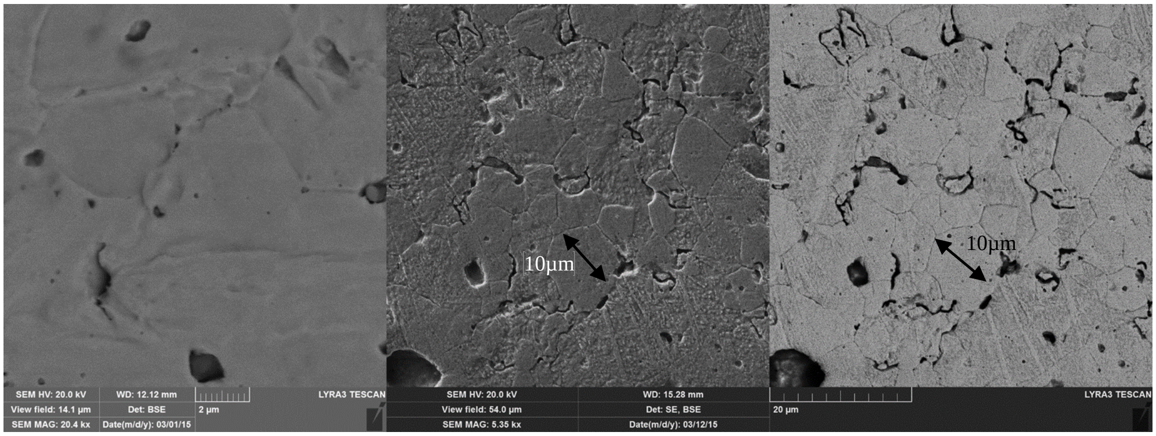

Figure 4-6 semi-alloyed specimen a) un-etched b) etched (SE and BSE) images

The microstructure of the composite containing 5 vol. % HfC sintered at 1800ºC for 10 minutes is presented in Figure 4-7. It reveals homogenous distribution of HfC in the matrix as indicated by arrows. In order to distinguish between different phases, both SE and BSE modes were used as shown in Figure 4-7 a) and b) respectively. It can be concluded that the homogenous dispersion of HfC in W-25wt%Re-5HfC obtained by mechanical alloying was maintained in the sintered sample. This homogenous dispersion of the HfC particles, in the W-25wt%Re-5HfC sintered composite, was confirmed through elemental mapping of Hf and C presented in Figure 4-9.

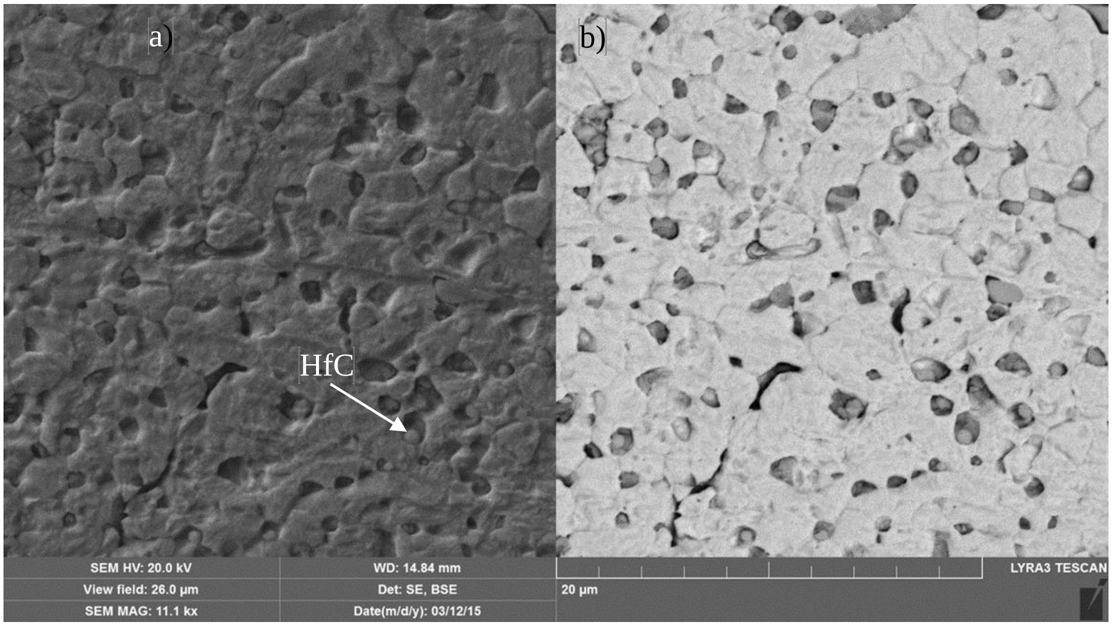

Figure 4-7 electrolytically etched 5vol%HfC composite a) SE b) BSE

In addition, to the advantage of SPS in minimizing grain growth, further inhibition of grain growth in the composites is attributed to the presence of HfC particles. It was reported that HfC particles dispersed at the W grain boundaries inhibited the growth of W grains in HfC-W composites.[83]. Detailed features for the 5vol % HfC are presented in Figure 4-8 (a, SE mode) and (b, BSE mode), which reveals the grain boundaries and homogenous dispersion of 5vol%HfC in the monolithic nanocrystalline alloy. Composite containing 10vol%HfC showed resistance to metallography (especially during polishing) due to the presence of relatively large amount of HfC contents and microstructural details were also not properly revealed as shown in Figure 4-8 (c).

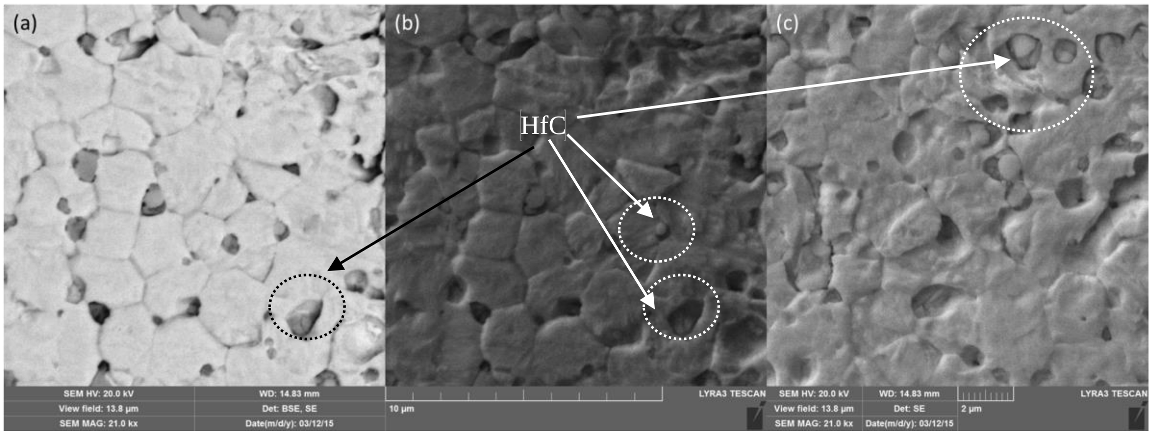

Figure 4-8 FESEM (a) 5vol%HfC in SE (b) BSE and (c) 10vol%HfC

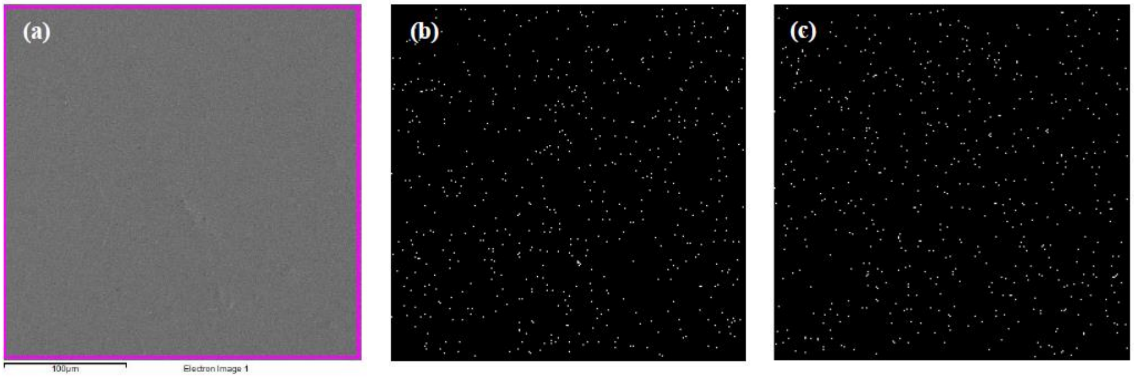

Figure 4-9 Mapping of 5vol%HfC composite (a) SEM (b) Hf, and (c) C

4.2.4. XRD analysis for consolidated monolithic alloy

Figure 4-10 (a) shows XRD spectra of W-25wt%Re alloy sintered at different temperatures for 10 minutes. It can be clearly seen that the intensity of the W-Re peaks increased and their broadening decreased with the increase in sintering temperature because of the increase in crystallite size. This is in fact the opposite of what occurred during milling. It is known that if polycrystalline materials are heated and left at high temperature, grain growth takes place to reduce the excess energy associated with grain boundaries [84]. The calculated crystallite size of sintered W-Re is presented in Figure 4-10 (b). It is worth reiterating here that, before sintering, this crystallite size was 13 nm. Sintering at 1500°C increased the crystallite size to 56 nm. The increase in sintering temperature to 1700 °C led to the increase in the crystallite size to 71 nm. Further increase in sintering temperature to 1800°C resulted in further increase in crystallite size to 80 nm. Figure 4-10 shows that the increase in sintering temperature resulted in the increase in crystallite size; and the higher the temperature, the more this growth was because of the enhanced diffusion rate. Isothermal grain growth dependence on temperature and time is generally described using the following simple equation:

$$\boldsymbol{G^n - G_0^n} = \mathbf{Kt} \qquad \textbf{Equation 4.1}$$

where G_0 and G are the grain sizes at initial time t_o and isothermal holding time t, respectively. K is the material's constant that depends on the temperature:

$$\boldsymbol{K = K_0 exp^{(\frac{-Q}{RT})}} \qquad \textbf{Equation 4.2}$$

where Q is the activation energy for grain growth, R is the gas constant and T is temperature. Although sintering led to crystallite size growth in all samples, the average crystallite size of the W-Re solid solution remained in the nanometer range and did not exceed 80 nm. In SPS, it is claimed that a local high temperature-state is generated momentarily because of spark discharge that takes place in the gap or at the contact point between particles. This leads to evaporation or melting on the surface of particles and formation of necks. In addition to the high-localized temperature, the applied pressure and current improve heating rates and reduce sintering time and temperature. Therefore, nanopowders might be consolidated using SPS without excessive grain growth [16].

Crystallite sizes of the tungsten phase in composites containing 5 and 10 vol.% HfC, sintered at 1800ºC for 10 minutes, were 71 and 64 nm, respectively, compared to the monolithic sample, sintered under the same conditions, which had a crystallite size of 80 nm.

4.2.5. Density and microhardness

The bulk density of the consolidated samples was measured according to the Archimedes principle using Metler Toledo balance density determination KIT model AG285. Digital microhardness tester (Buehler, USA) was used to measure the microhardness of the developed materials. The obtained hardness values were the average of 10 readings. Conditions of a load of 300 gf and a time of 12 s were used in all measurements.

Relative density and hardness of the fully alloyed and consolidated W-25wt%Re is presented in Figure 4-11. The sample consolidated at 1500ºC for 10 minutes had a relative density of 92 %. The increase in sintering temperature to 1700ºC increased its relative density to 96.2 %. A further increase in sintering temperature to 1800ºC increased its relative density to 97.8 %. Overall, the relative density increased with the increase in sintering temperature because of the enhanced diffusion rate [85].

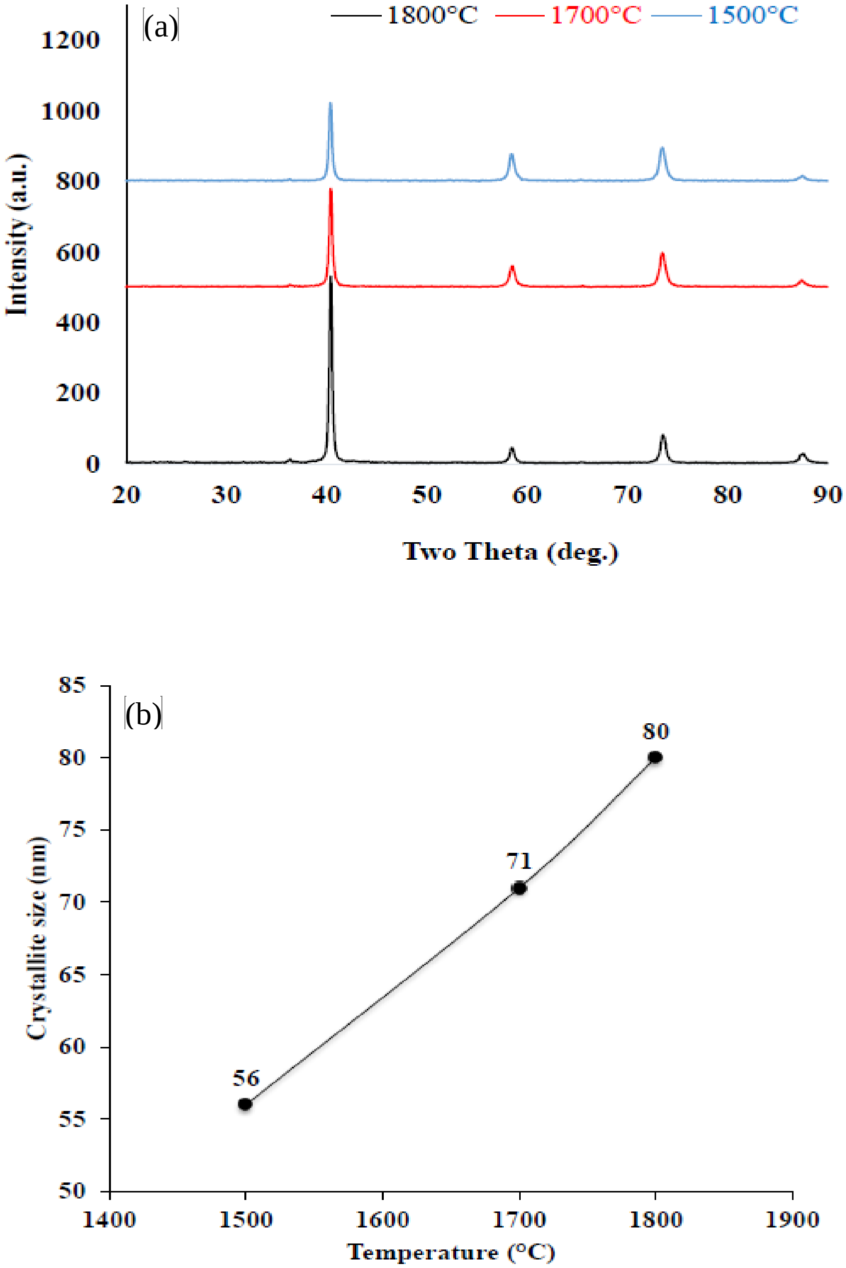

Figure 4-10 (a) XRD and (b) crystallite size of the sintered alloy

Therefore, the higher the sintering temperature, the higher the diffusion rate and the lower the remaining pores. This can be explained through the dependence of density on sintering temperature [86] as follows.

$$\rho = s\left(\frac{T}{T_m}\right) + b \qquad \textbf{Equation 4.3}$$

where, ρ is the relative density, *s* is the temperature sensitivity, *T* is the sintering temperature, and T_m is the melting temperature. On the other hand, the externally applied pressure contributes to the rearrangement of particles and breakdown of agglomerates. This leads to the increase in driving force for sintering. In addition, in SPS process, spark plasma, spark impact pressure, Joule heating, and an electrical field diffusion effect could be generated by the DC pulse discharge [87][88][89][90]. The formation of plasma enhances sintering, however, the role of current is still not clear [87][91]. It is believed that a local high temperature state momentarily occurs in the gap between particles of the powder because of the spark discharge. This induces vaporization and melting of the surfaces of the powder particles, which significantly increases diffusion rate and leads to higher densification.

The sample consolidated at 1500ºC for 10 minutes had a microhardness of 360. The increase in sintering temperature to 1700ºC increased its microhardness to 395. A further increase in sintering temperature to 1800ºC increased its microhardness to 422. The hardness of a sintered material mainly depends on its grain size and porosity. Generally, the grain size *d* dependence of the yield stress σ_{ys} is described by a general expression (Hall-Petch relationship)

$$\sigma_{ys} = \sigma_0 + kd^{-1/2}$$ **Equation 4.4**

where σ_0 is the lattice friction stress, *k* is a Hall–Petch slope. Vickers hardness of a polycrystalline material can be related to its yield strength through a simple relationship $H_v/\sigma_{ys} \approx 3$. Therefore, the hardness H_v can be related to the grain size by

$$H_v = H_0 + kd^{-1/2}$$ **Equation 4.5**

where H_0 and k are constants. It is clear from the above relationship that the increase in the grain size reduces the hardness of a material. However, hardness of the alloy increased despite the increase in the grain size because of the fact that during sintering pores are eliminated and the density of the material increases. Therefore, the hardness of the material strongly depends on its relative density and the effect of grain growth will be small. This is more meaningful, specifically with a process such as spark plasma sintering where the heating rate is high, the sintering temperature is low, and the sintering time is short compared to other conventional sintering processes [92][93][94]. This leads only to very marginal grain growth as explained above, and therefore the hardness is mainly influenced by density. Since higher density and hardness were obtained at a sintering temperature of 1800ºC, all other samples were sintered at this temperature for 10 min. Figure 4-12 shows the relative density and hardness of partially alloyed W-25wt%Re, fully alloyed W-25wt%Re, W-25wt%Re-5HfC composite, and W-25wt%Re-10HfC composites sintered at 1800ºC for 10 min. The partially and fully alloyed samples had relative densities of 98.2 and 97.8 %, respectively. The composites containing 5 and 10 vol. % of HfC processed relative densities of 96.9 and 96.2 %, respectively. The composites containing 5 and 10 vol. % of HfC displayed slightly reduced relative density by ~0.92 and ~1.63 %, respectively, with respect to the fully alloyed monolithic alloy; and by ~1.32 and ~2.03 %, respectively, with respect to the partially alloyed monolithic alloy.

Compaction of nanostructured powders or nanocomposites reinforced with hard particles is believed to be more difficult than compaction of their conventional counterparts because of the larger stresses required and the higher spring back. Therefore, nanostructured green compacts usually contain remaining pores [95][96][97], and may not sinter to full density easily. On the other hand, the addition of a reinforcement usually lowers the densification of the composite specifically at large volume fraction. As can be clearly seen in Figure 4-12the evolution of Hardness of sintered samples, as presented in Figure 4-11, followed the same trend as in densification. The partially alloyed sample had a microhardness of 360. The fully alloyed sample had a microhardness of 423. Since the two alloys possessed very close relative densities i.e. 98.2 and 97.8 %, respectively, the higher hardness of fully alloyed sample is attributed the effect of mechanical alloying because the fully alloyed sample was milled for an additional 25 h.

The addition of 5 % HfC increased the microhardness to 450. Further increase in HfC content to 10 vol. % increased the microhardness to 495. The composites containing 5 and 10 vol. % of HfC possessed improved hardness by ∼11 and ∼22 %, respectively, with respect to the fully alloyed monolithic alloy; and by ∼25 and ∼37.5 %, respectively, with respect to the partially alloyed monolithic alloy. The composite containing 10 vol. % of HfC possessed the highest Vickers hardness value of 495. As for the composites, the increase in hardness can be attributed to the same factors which lead to the increase in the strength of particle reinforced metal matrix composites. This include small grain size of the matrix (Hall Petch theory), presence of particles (Orowan strengthening), increase in dislocations' density, load transfer from the matrix to the reinforcement, and strain gradient [98][99][100][101].

The decrease in grain size leads to the increase in grain boundaries, which has a significant influence on strength. This is because grain boundaries restrict dislocation motion due to the different orientation of adjacent grains and the discontinuity at the highly disordered grain boundary region. In Orowan strengthening, the moving dislocations bow out between particles and yielding takes place when the bowed-out dislocations become semi-circular in shape, after that dislocations leaves Orowan loops around the particles. These loops hinders dislocation movement, which leads to work hardening. On the other hand, during cooling from sintering temperature to room temperature, geometrically necessary dislocations are formed due to the difference in coefficient of thermal expansion and modulus of elasticity between the reinforcement and the matrix. This leads to strain hardening of the material.

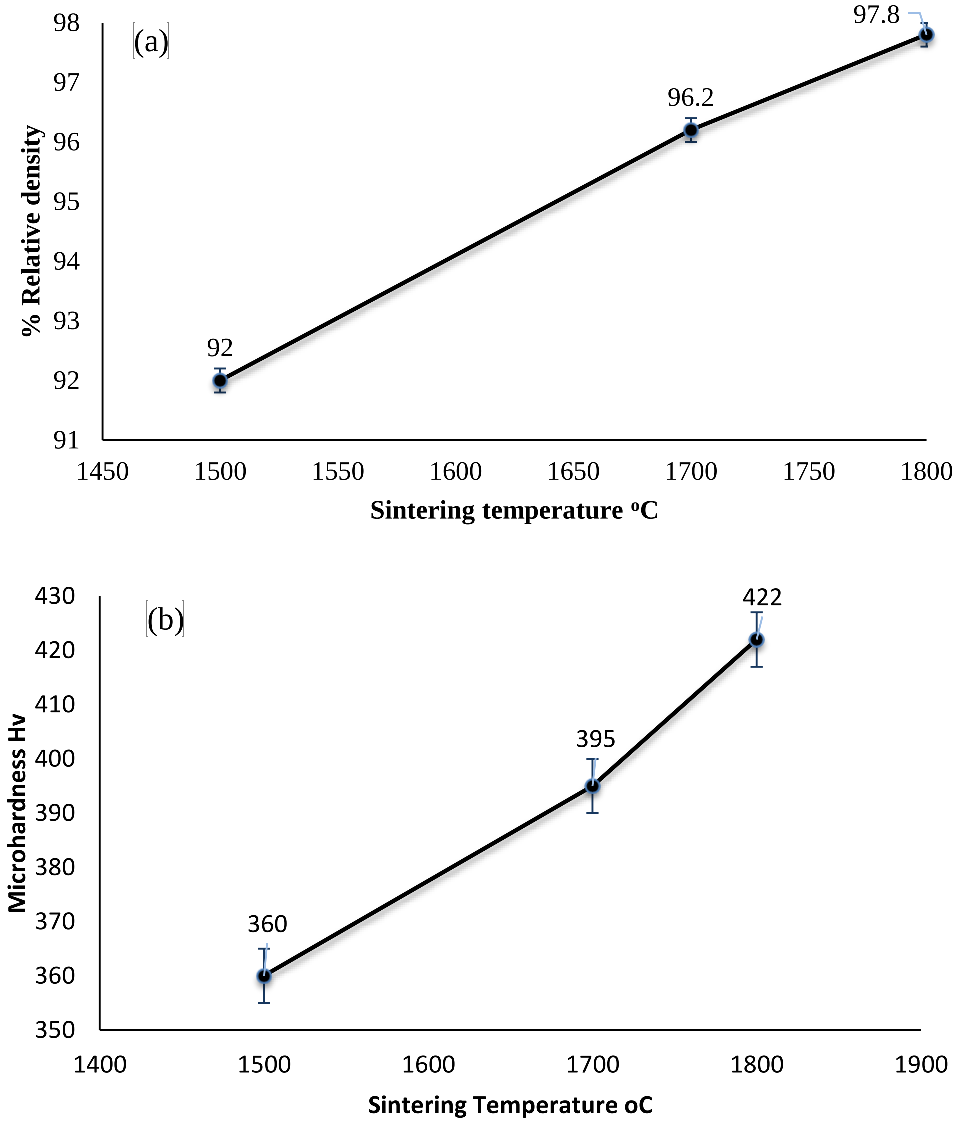

Figure 4-11 (a) Relative density (b) hardness of the alloy at different temperatures.

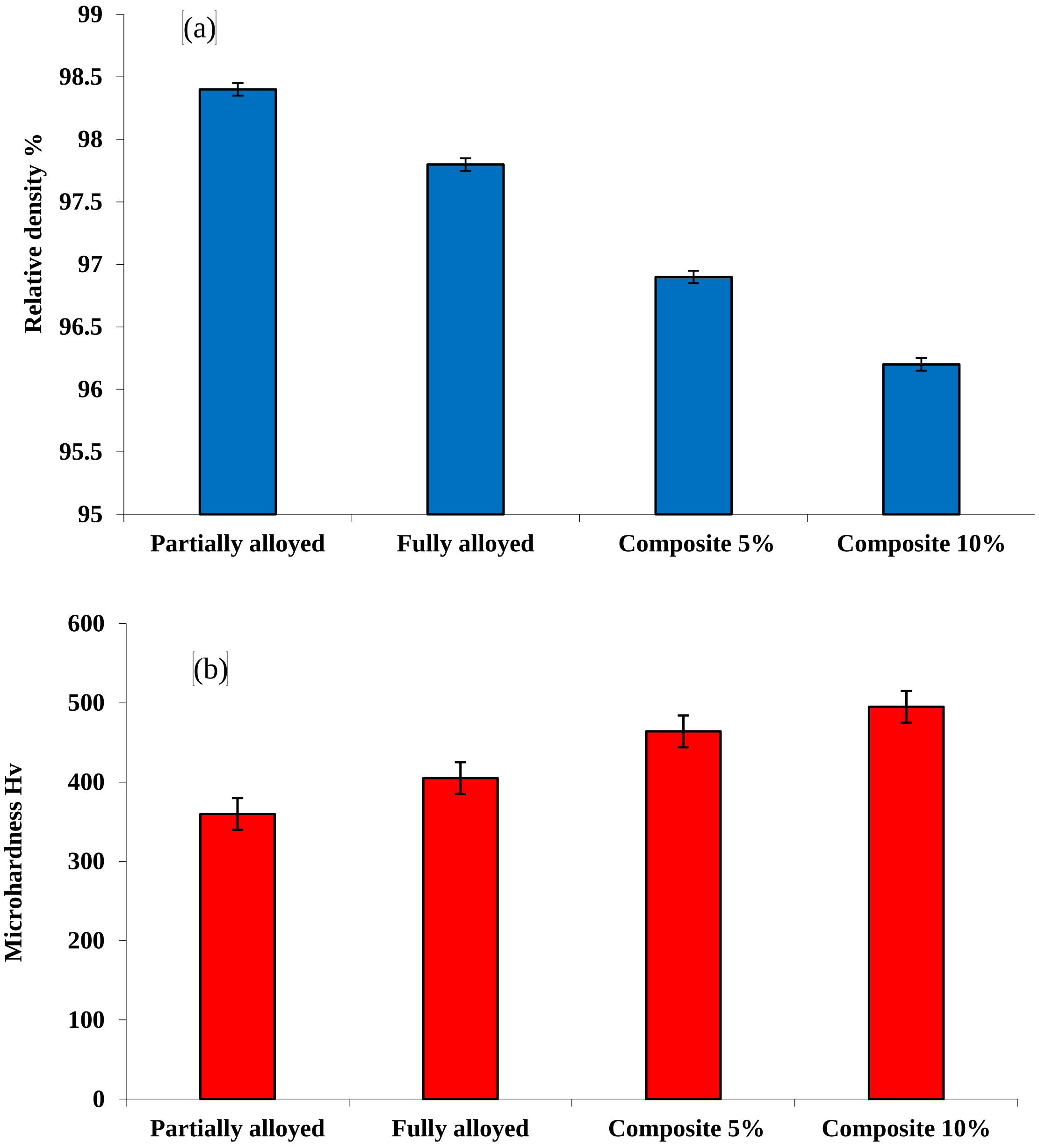

Figure 4-12 (a) Relative density and (b)hardness of samples sintered at 1800°C.

4.2.6. Thermal conductivity

Thermal conductivity analysis for the consolidated specimens were carried out by Thermal Conductivity Analyzer equipment. Thermal conductivity sensor used in the investigation is shown in Figure 4-13 (a). Three drops of water were used to make a contact between the specimen and the thermal conductivity probe. Thermal conductivity behavior of monolithic W-25wt%Re alloy sintered at 1500ºC, 1700ºC and 1800ºC is presented in Figure 4-13. It was found that thermal conductivity was increased with the rise of consolidating temperature. The increase in TC (thermal conductivity) can be attributed to the high relative density achieved at high temperature as discussed in previous section. At high temperature, degree of porosity will be reduced and particle to particle contact will be more compact and as a result thermal conductivity will be increased. Thermal conductivity of the composites consolidated samples were found to decrease with the increase of HfC contents as shown in Figure 4-14. HfC has a lower thermal conductivity than the monolithic metallic matrix as a result thermal conductivity decreases with the increase of HfC contents.

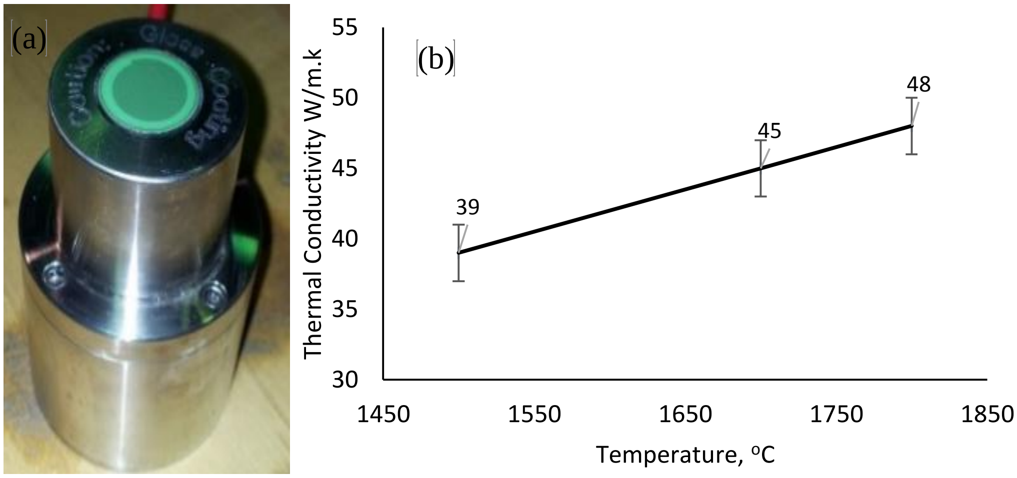

Figure 4-13 (a) Thermal conductivity sensor (b) thermal conductivity of the alloy

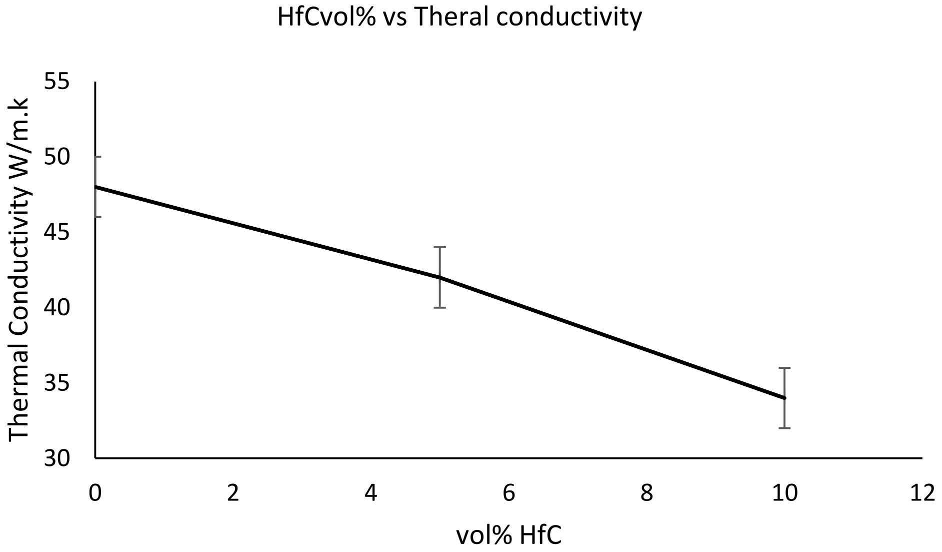

Figure 4-14 Thermal conductivity for composites as a function of HfC contents

4.3 Sliding wear behavior

Wear characteristics of monolithic W-25wt%Re alloy sintered at 1500^{o}C and 1800^{o}C and W-25%Re-5HfC composite sintered at 1800^{o}C have been investigated in dry sliding conditions against a steel counter face using a pin-on-disk equipment as shown in Figure 4-15. W-25wt%Re-10HfC composite was also tested under same conditions but it got heated and resulted in extensive wear of the pin so wear behavior of this composite is not included in this section. Cylindrical discs having diameter of 20 mm and a height of 4 mm were prepared from sintered monolithic alloy and the composite. Specimens were cut into discs for the wear tests and surface was prepared for metallography analysis. After metallography, specimens were electrolytically etched in 1 M NaOH for 3 seconds to reveal the microstructure. Before the start of each wear experiment, the specimens and the balls were both rinsed ultrasonically in acetone. Experiments were carried out by using Oscillating Tribometer Testing Machine. Tests were performed according to ASTMG 99 standards with a load of 5-15N. The linear sliding speed was 50mm/s and the total sliding distance was 100m with an angular velocity of 120 rpm. The tests were performed at ambient temperature. Wear analysis of worn out surfaces and wear debris of nine specimens was carried out by using FE-SEM and optical profilometer. Wear rate and Coefficient of Friction COF were calculated from the test data.

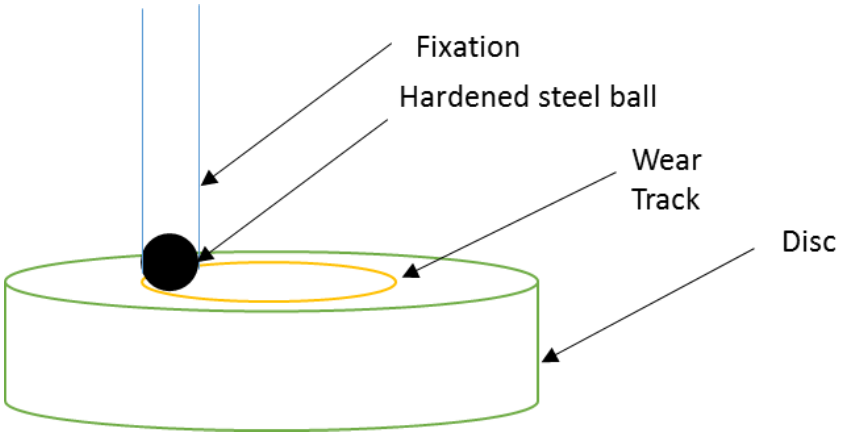

Figure 4-15 a) Schematic of Ball-on-Disc setup for the wear tests

4.3.1 Morphology of worn surfaces

Figure 4-16 shows FE-SEM images of wear tracks for monolithic and composite specimens. It can be observed that wear track profiles are different in size for the alloy SPSed at two different temperatures as shown in Figure 4-16 (a) and (b) and composite sample as shown in Figure 4-16 (c). Significant improvements in wear resistance, as indicated by the reduction in wear track width, was attained by increasing sintering temperature from 1500°C to 1800 °C. This can attributed to a reduced microcracking in the materials due improved density, hardness and reduced porosity as explained earlier and reported by other researcher [107].

Sintering is a thermally activated process controlled mainly by diffusion. Monolithic sample sintered at 1500°C shows greater amount of wear which can be attributed to extensive ploughing actions for the poorly bonded sintered sample. As porosity increases, the wear becomes more prominent because pores acts as a source of crack nucleation and propagation leading to excessive sub-surface fracturing.

Wear resistance was further enhanced by the addition of HfC in the matrix as shown in Figure 4-16 (c). The improvements in the wear resistance of the composite was attributed to improved microhardness due to the increase in the volume fraction of the relatively hard second phase reinforcement [102].

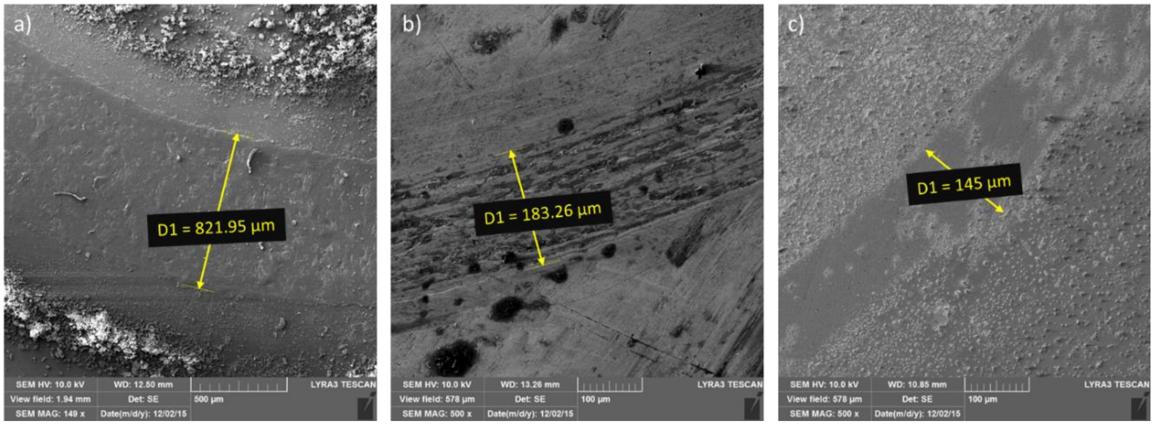

Figure 4-16 FESEM (a) alloy, 1500^{o}C (b) alloy, 1800^{o}C (c) composite, 1800^{o}C

Figure 4-17 shows the wear morphology of the monolithic alloy sintered at 1500^{o}C. It has gone for extensive wear with a width of wear track of 820 µm and a depth of 10 µm as indicated by optical profile presented in Figure 4-17 (a). The worn out material tends to buildup on the inner and outer periphery of wear track as depicted in Figure 4-17 (b). A prominent surface damage with deformed appearance can be observed on the wear track.

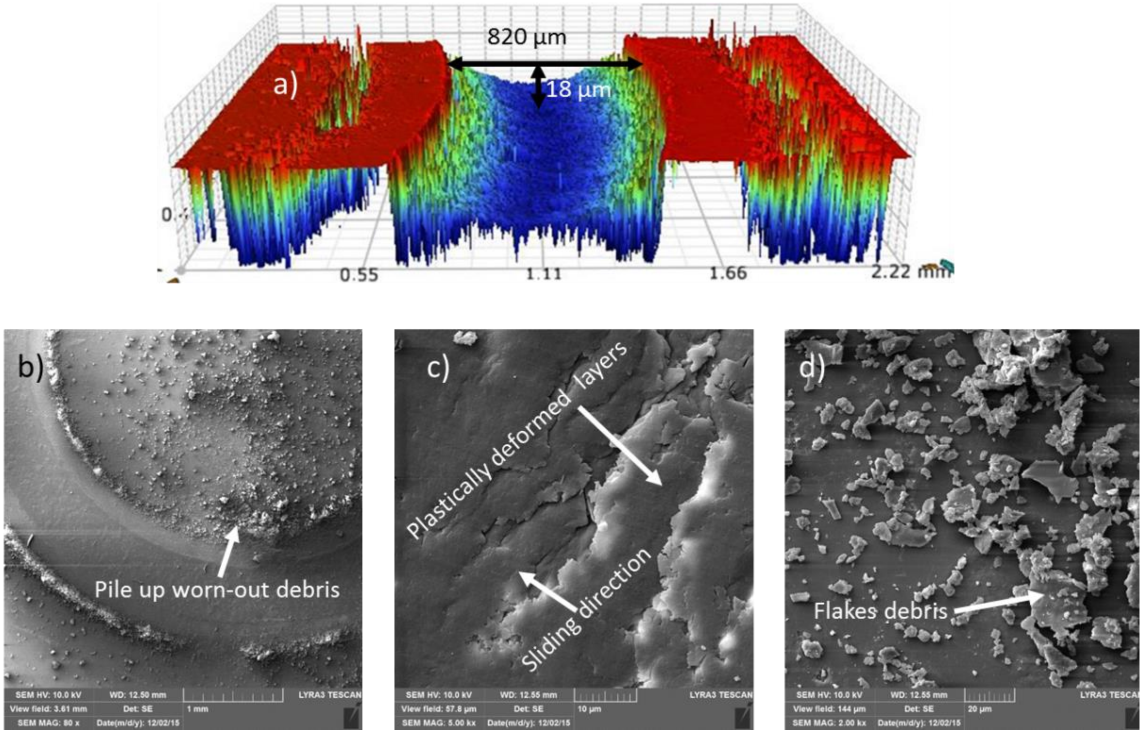

Figure 4-17 alloy sintered at 1500 ^{o}C (a) optical (b) track (c) deformation (d) debris

The shape of the debris looks like flakes as noticed in Figure 4-17 (c). To understand the wear mechanisms, surface grooves and marks were analyzed. It can be inferred from the micrographs that wear is predominantly an abrasive in nature. The specimen has lower density and has greater amount of porosity due to lower sintering temperature as discussed earlier. Moreover, it has been reported by some researchers that wear resistance of a material, synthesized by powder metallurgy, is very sensitive to the amount of pores present in the sample [110].

Figure 4-18 shows the wear track images and its detailed morphology for the monolithic sample sintered at 1800^{o}C. It is evident that material has been removed due to ploughing action of the ball on the material. In some areas, the presence of grooves on the worn surface was indicative of abrasive wear due to presence of abrasive marks, parallel grooves and stripes on the track. Pockmarks representing regions from which large chunk of material have been removed can also be observed. Figure 4-18 (b) shows optical profile image which illustrates considerable reduction of track width from 821 µm to 185 µm when sintering temperature was increased from 1500°C to 1800°C. Track depth was found to be 1.5 µm. The reduction in wear damage at 1800°C, can be explained on the bases of enhanced diffusion at high temperature and improved density due to more elimination of porosity at high temperature.

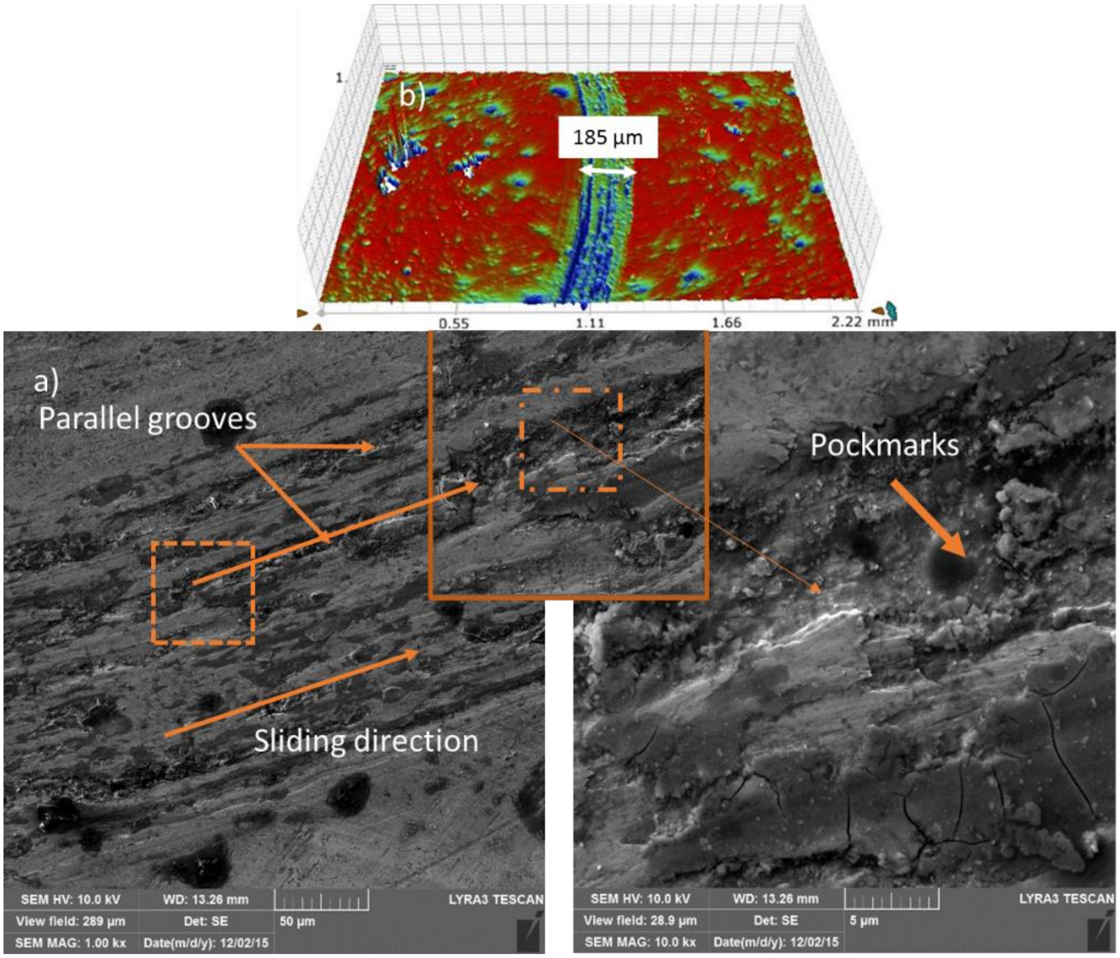

Figure 4-18 FESEM for the wear of alloy sintered at 1800°C

Figure 4-19 shows the FESEM images of the wear profile and morphology of debris of composite specimen. Figure 4-19 (a) & (b) shows that large areas were covered with wear debris. These small sized wear debris have been removed from the material by adhesive wear as shown in Figure 4-19 (c) & (d). The addition of HfC in the monolithic alloy has reduced the width of the track from 185µm to 145µm and depth from 1.5 µm to of 1.1 µm as shown in Figure 4-19 (e). The higher wear resistance of the composite can be attributed to its higher values of hardness as compared to the monolithic alloy. To further understand the difference in wear behavior between alloy and composite, debris and sliding configuration were observed. There are no marks of abrasive wear on the wear track as depicted for alloy sample.

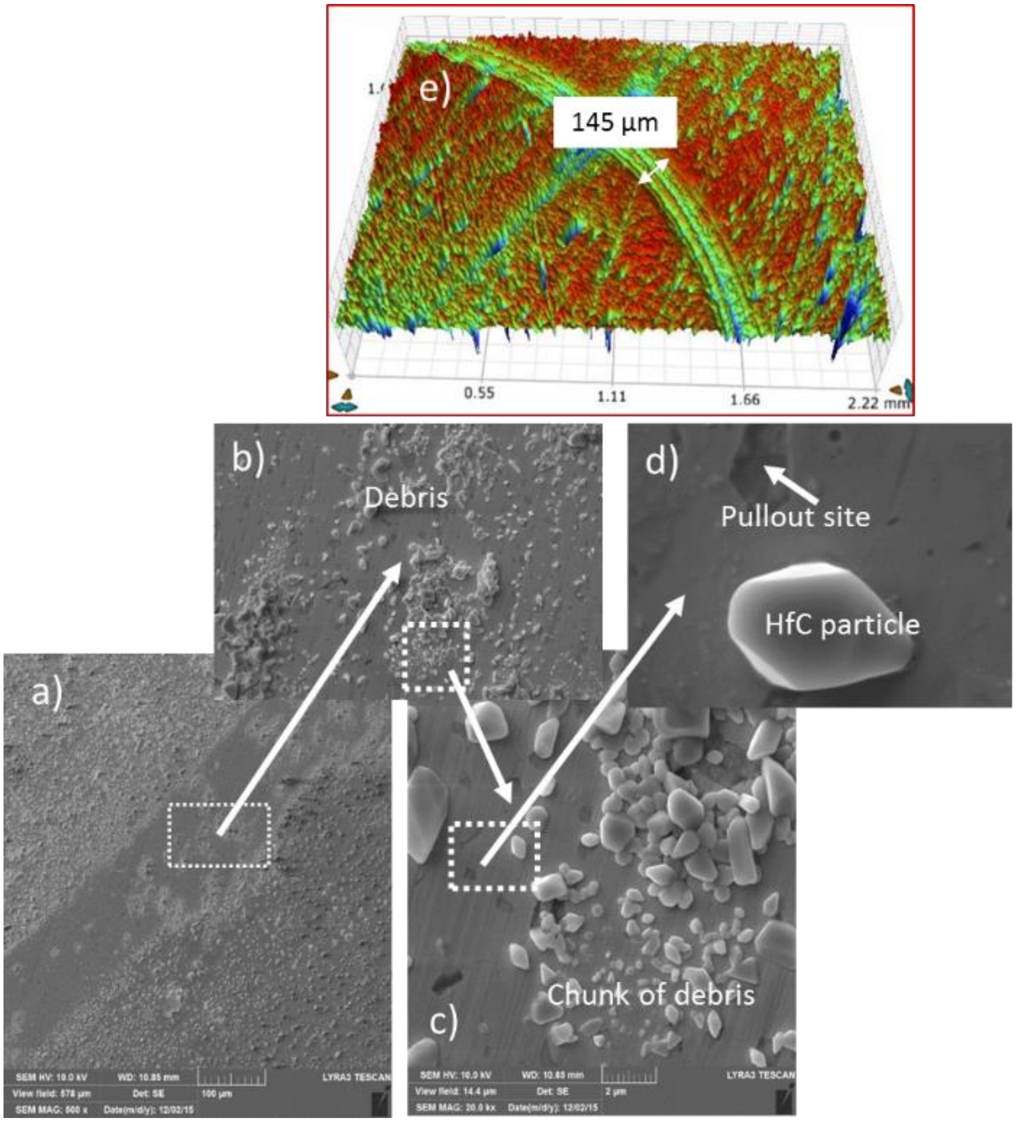

Figure 4-19 FESEM of the composite (a) wear track (b-d) debris e) optical profile

The shape of the debris were rounded chips. The wear mechanism can be identified as adhesion. Continuous sliding friction between HfC and matrix could be a source of detachment of HfC particles. It is difficult to confirm any signs for existence of abrasive wear as there were no parallel grooves on the track profile. Wear resistance dominantly rely on the dispersion of second phase and consolidation technique [108].

4.3.2 Wear rate study

Figure 4-20 shows the comparison of preliminary results of specific wear rate for different loads for a sliding distance of 10m. These results show a trend for load, sintering temperature and reinforcement contents. Wear rate increases with the increase of load and decrease with the increase of sintering temperature and reinforcement contents. Since amount of wear was not significant due to smaller sliding distance, so another set of experiments were performed to get a conclusive evidence.

Figure 4-20 shows the wear behavior of monolithic sample sintered for different temperature and composite containing 5vol%HfC sintered at 1800^{o}C. A trend for increase in wear resistance can be observed from these bar graph with the increase of sintering temperature and by the addition of HfC contents. Wear resistance was found to decrease with the increase of load. Since the wear rate order is low for 10 m sliding distance, another set of experiment was performed for a sliding distance of 100m.

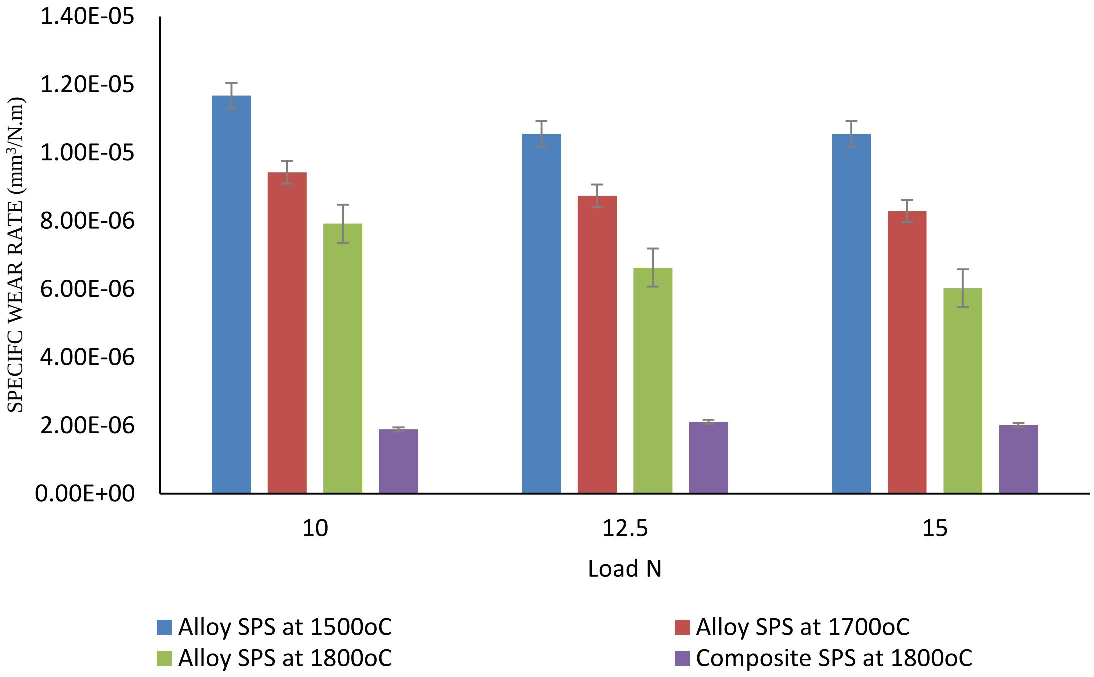

Figure 4-20 Wear rate tested at 5, 10 and 15 N for only 10 m sliding distance.

Figure 4-21 shows the comparison of wear rate of alloy and composite specimens. It also provides the effect of sintering temperature on the wear resistance of alloyed specimen. Wear resistance is improved with the increase of sintering temperature. This is in agreement with the FESEM analysis of the wear profile. This trend is also exhibited by most metallic materials [103][104][105]. Improvements in wear resistance was attained due to the enhanced consolidation and improved hardness of alloy with the increase of temperature as shown in Figure 4-21. The wear resistance was further improved for composite due to strengthening by the second phase hafnium carbide. This fact is supported by the laws of wear i.e. the wear rate of a material is inversely proportional to the hardness of the softer sliding component [106]. A comparison of relative density, microhardness and wear is presented in Table 4-1. The results showed that relative density, microhardness and consequently wear resistance was increased for monolithic alloy with the increase of sintering temperature. Wear resistance was found to improve with the addition of 5vol% HfC in W-25wt%Re matrix.

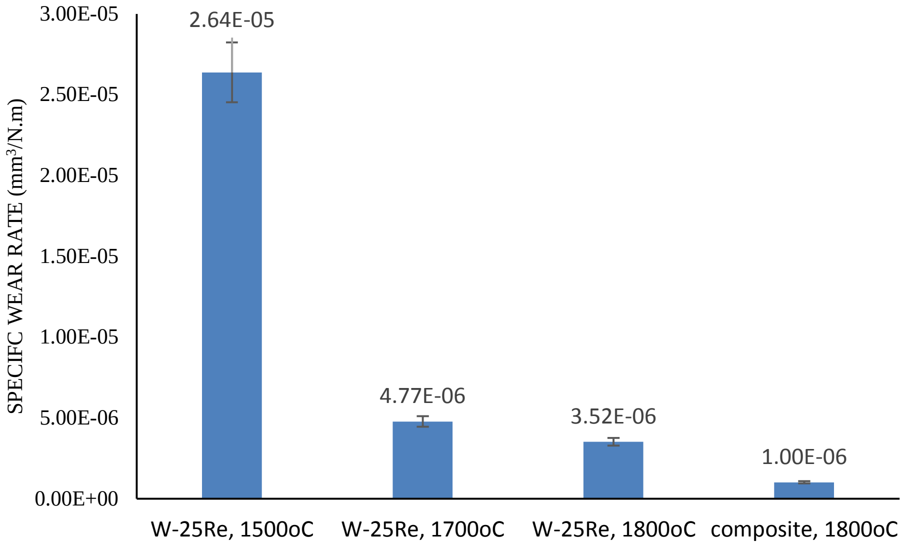

Figure 4-21 A comparison of specific wear rate for the alloy and composite

Table 4-1 Effect of sintering temperature and HfC on hardness and relative density

Composition	**Temperature (^{o}C)**	**Microhardness (Hv)**	**Relative density (%)**	**Spec. wear rate (mm^3/N.m)**
W-25%Re	1500	360	92.2	2.64E-05
W-25%Re	1700	396	96.5	4.77E-06
W-25%Re	1800	425	98.3	3.52E-06
5vol%HfC	1800	495	95.2	1.00E-06

Figure 4-22 shows the coefficient of friction (COF) of monolithic alloy varies between 0.35 and 0.52 when sintered at 1500^{o}C with no evidence of steady state for these conditions. Figure 4-23 shows the coefficient of friction alloy specimen sintered at 1800^{o}C. The COF varies between 0.63 and 0.76 which can be due high contact forces between the surfaces.

Initially friction coefficient of the monolithic alloy increased continuously and remained steady for the remaining interval of the experiments.

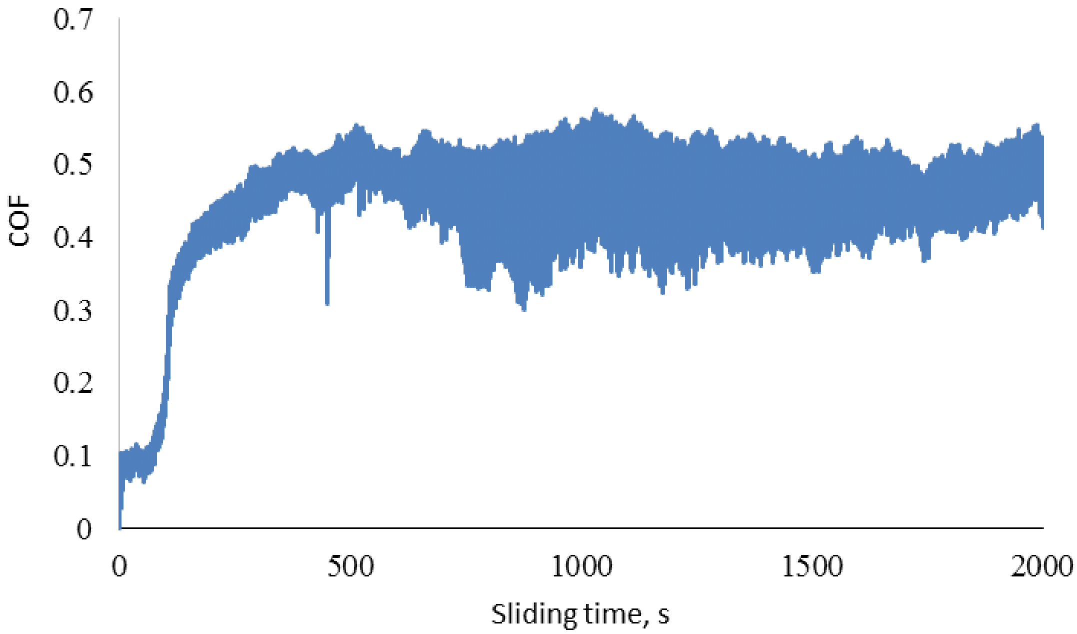

Figure 4-22 COF vs time for fully alloyed sample sintered at 1500ºC

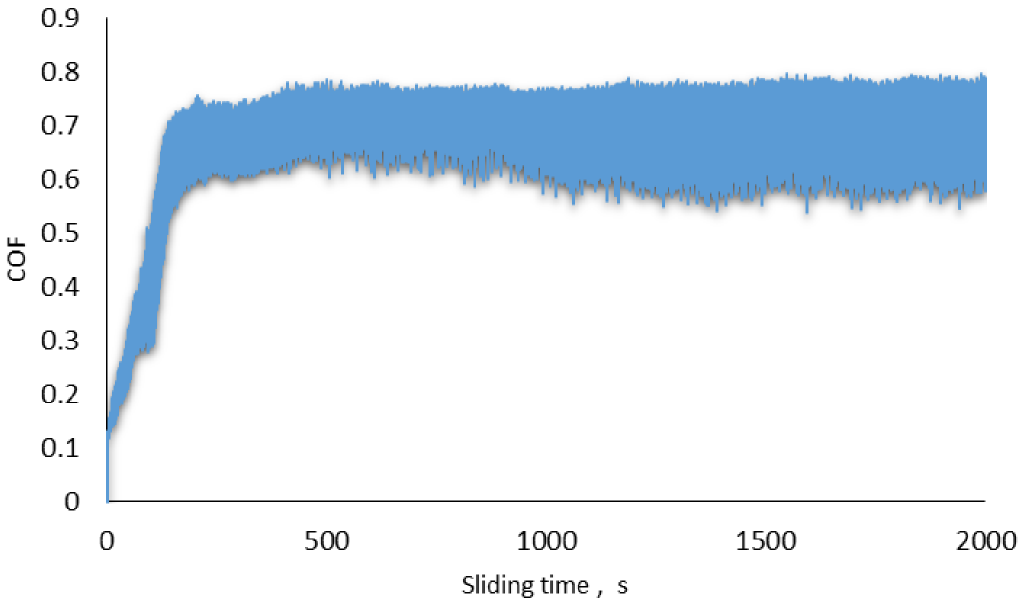

Figure 4-23 COF as a function of time for fully alloyed sample sintered at 1800ºC

Initial stage behavior can be attributed to a polishing process during the wear test, trying to establish a smooth wear track surface, by plowing away the surface asperities or roughness irregularities. However, COF remained steady at an average value of 0.39 for the remaining time interval. It is also evident that the composite's friction coefficient is not only lower but also has considerably less fluctuation as compared to the monolithic alloy.

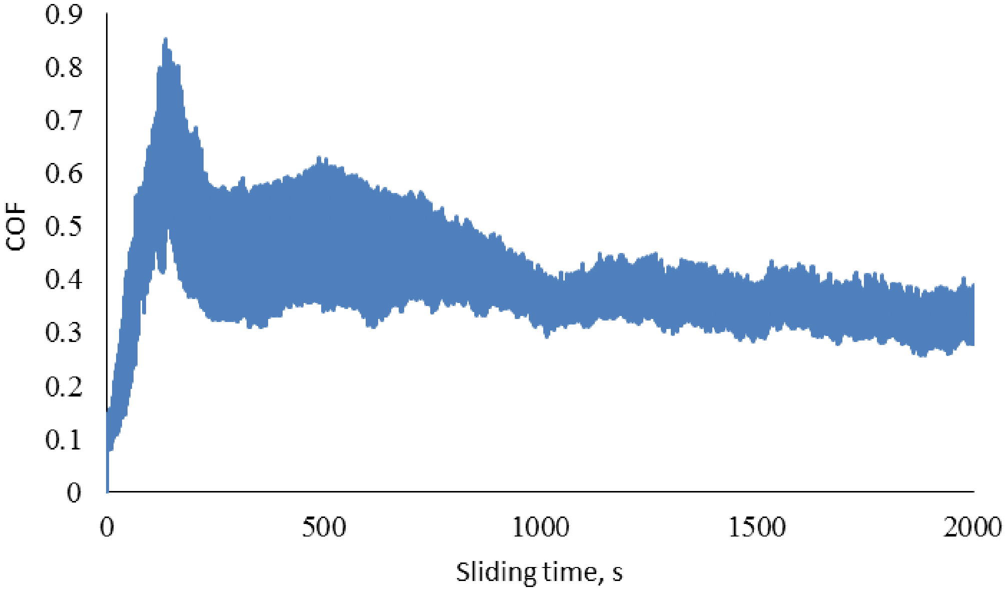

Figure 4-24 COF as a function of time for composite containing 5vol%HfC

CHAPTER 5

FRICTION STIR WELDING OF HIGH MELTING POINT MATERIALS

The main objective of this section is to study the performance of an extruded W-25%Re pin tool for the FSW of ASTM A516 Grade 70 mild steel plates. The outcome of this part will provide base line parameters for the feasibility of newly developed pin tool in FSW of steel in later stages. The pin tool was designed by Edison Welding Institute (EWI) and manufactured using extrusion by Rhenium Alloys Inc., in the USA. Main emphasis will be put on the wear behavior of the tool. It will also cover the effect of Friction Stir Welding (FSW) process parameters such as tool rotation speed on the quality of the bead. Tool reactions forces, microstructural features along with microhardness behavior were investigated by varying tool rotational speed.

5.1 Experimental set-up

A set of single-pass partial penetration bead on plate (BOP) were produced using fully instrumented MTI (Manufacturing Technology Inc.) Model RM-1 friction stir welding machine. Proprietary W-25 wt. % Re tool was used to produce the beads on ASTM A516 Grade 70 carbon steel plates containing 0.25%C and 0.24% Si. ASTM A516 Grade 70 is widely used in producing pressure vessels and heat exchangers.

A schematic diagram presenting the initial tool pin-shoulder dimensions is shown in Figure 5-1 (a) Tool shape and (b) geometry [mm] along with FSW tool photograph. The tool consists of a simple tapered tool pin and a flat shoulder. This tool geometry was adopted for seal welding applications where full penetration is not required. In all tests, welding speed was ramped from 15 mm/min to a final velocity of 40 mm/min (15 mm/min (0-5mm), 30 mm/min (5-15 mm), 40 mm/min (15-end mm), with a combination of tool rotational speeds of 800, 1500 and 2000 rpm. Speed was gradually increased to avoid tool-pin fracture. The machine tilt angle was 0.1o and the dwell time was fixed to 3 seconds. Argon shielding gas was used during the friction stir welding of these beads in order to avoid oxidation of the base metal, as well as to prevent deterioration of the tool pin surface.

Tool axial force and torque were recorded using the machine built-in sensors as well as data recording system. Tool axial force and torque were recorded using the machine built-in sensors as well as data recording system. The data collected during the process was used to (1) study the effect of tool rotational speed on the dependent process parameters (i.e. tool axial load and torque), (2) find the relationship between weld quality (surface integrity) and load profiles, and (3) estimate the heat input or line energy E as shown in Eq. (5.1)

$$E = \frac{2pNT}{u\left(1 + f\right)}$$ **Equation 5.1**

Where f is the tool/workpiece heat ratio, N is the tool rotational speed in rpm, T is averaged measured tool torque in N.m, and u is the tool traverse speed (welding speed) in mm/sec. The tool/workpiece heat fraction f can be estimated using Bastier's model [55] that describes one-dimensional steady-state heat transfer from a point heat source located at the interface of dissimilar metals presented in Eq. (5.2).

$$f = \frac{J_T}{J_W} = \sqrt{\frac{\left(krC_p\right)_T}{\left(krC_p\right)_W}}$$ **Equation 5.2**

where k is the thermal conductivity, ρ is the density, and C_p is the specific heat. Subscripts *T* and *W* indicates tool and workpiece, respectively.

In order to perform microstructural, microhardness and chemical analysis and investigate the effect of tool rotational speed on weld quality, fabricated beads were transversely sectioned in zones where final welding speed (40 mm/min) was achieved. Samples were mounted, grinded, polished and etched using 2% Nital solution to examine microstructural features and then perform microhardness measurements.

Optical magnifier was also utilized to study the nugget soundness of the developed bead by revealing the processed zone and developed volumetric defects if any. Optical microscopy analysis of the bead sections was conducted at different magnifications in order to investigate the microstructural details of the developed bead zones. Microhardness of bead was measured using Vickers microhardness tester. The indenter load was set at 300 g for a period of 15 seconds. The hardness was measured across the bead and the depth from the bead's centerline. Moreover, spectroscopy analysis was performed to study the chemical composition in the processed zone, and to understand the effect of tool rotational speed on tool diffusion wear.

The setup for workpiece fixture shown in Figure 5-2 consists of backing plate for supporting the workpiece fixture, clamps and screws for holding the workpiece. Argon shielding gas was used to avoid the oxidation of the base metal at high temperature developed during the process.

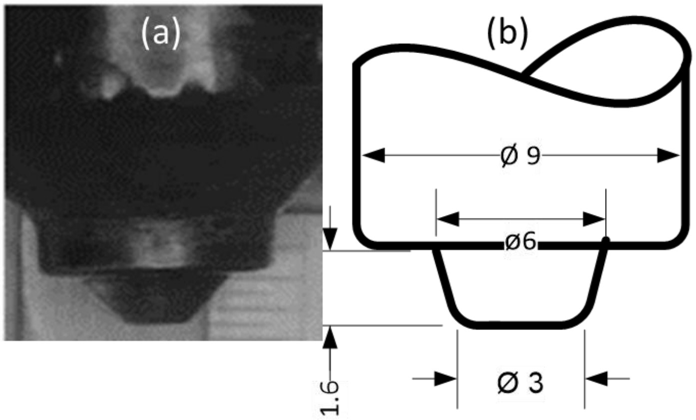

Figure 5-1 (a) Tool shape and (b) geometry [mm]

The spindle and the tool were cooled by ethylene glycol coolant to avoid the overheating of the tool assembly. Loads profiles were recorded at different welding conditions. They were found to be strongly coupled to bead surface quality.

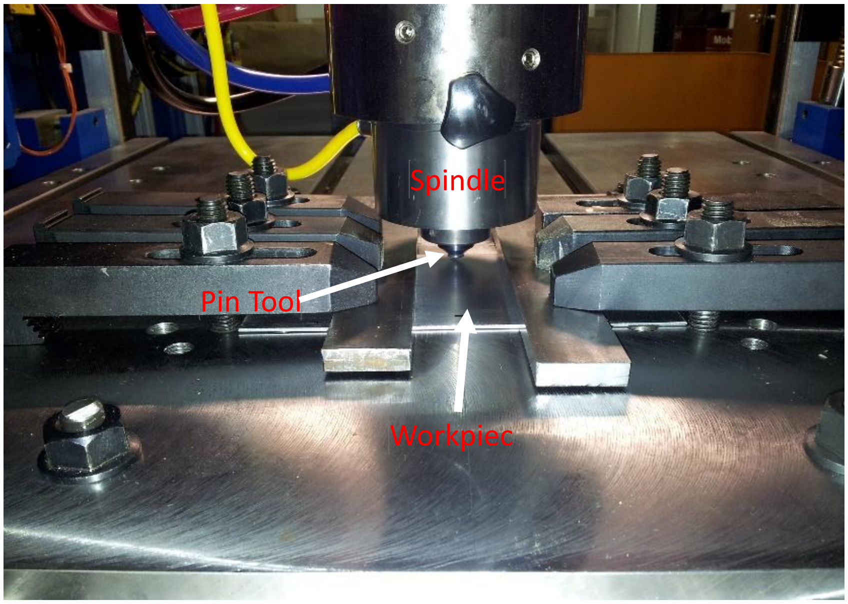

Figure 5-2 Friction Stir Welding setup for developing beads on steel plate.

5.2 Development and characterization of FSW Bead-on-Plate (BoP)

5.2.1 Influence of rotational speed on bead quality and reaction loads

Figure 5-3, Figure 5-5 and Figure 5-6 show developed beads surface, with measured tool reaction loads at process conditions mentioned in the previous section. It can be seen from recorded tool loads that steadiness of tool axial force and torque indicated a stabilized process, which is reflected on bead surface quality (Figure 5-3 a) and c)). Tool axial force and torque-displacement profiles were found to be strongly coupled to bead surface quality. As mentioned previously, three different tool rotational speeds were investigated in this work. Three beads were produced at 800 rpm, shown in Figure 5-3 (a-c), while 2 more samples produced at 1500, and 2000 rpm shown in Figure 5-5 and Figure 5-6 respectively.

Although the same welding conditions were used for the first three beads, some discrepancies in outcome findings were observed. They were brought by material build-up on the tool shoulder and pin. In Figure 5-3 a, the trend of the performed welding indicated a uniform pattern in the beginning. After the tool traveled a distance of 50 mm, fluctuations in torque and axial force accompanied with repeated pattern surface defect were noticed as indicated by the dashed circle.

After welding, the tool was examined by visually and Scanning Electron Microscope SEM as shown in Figure 5-4. Visual inspection shows large amount of steel deposition accumulated on the tool. The deposited steel resulted in creating an eccentric tool profile. The tool with built-up (or accumulated debris) was used to produce the second bead shown in Figure 5-3b. Uniform (repeated) surface defects pattern was obtained at every shoulder advancement (10 mm). These defects were accompanied by fluctuations in tool loads. Surface defect were similar to those formed at the end of the first bead in Figure 5-3a.

Similar deposition was found on the tool after completion of the second bead, which support that the formed surface defects were resulted from the tool built-up. To remove the deposited material (built-up), a small bead was intentionally produced with larger over plunging depth, in order to increase the process temperature. As a result, a clean tool surface emerged. Using the clean tool a third bead was produced with a smooth and defect free surface manifesting a stable tool reaction loads as shown in Figure 5-3c.

The built-up of working material on the tool is extremely critical; as it modifies the tool profile that may result in reducing the weld quality. However, there are many parameters that control the work material build-up; namely, the tool temperature and its surface condition. Enhancing the tool surface quality may reduce the problem of the build-up material.

Increasing the tool rotational speed from 800 to 1500rpm and then to 2000rpm resulted in excessive fluctuations in tool reaction loads, with an increase in peak-to-peak axial force and torque values (Figure 5-5 and Figure 5-6). Fluctuations in torque could be attributed to the stick slip action between the tool and the workpiece. Bead surface pattern produced at rotational speed of 1500 rpm was not uniform. It can be seen from Figure 5-5(a) that a smoother surface was generated at the end of the bead, with signs of excessive heat input (change in surface colors) at the bead sides (Figure 5-5 b).

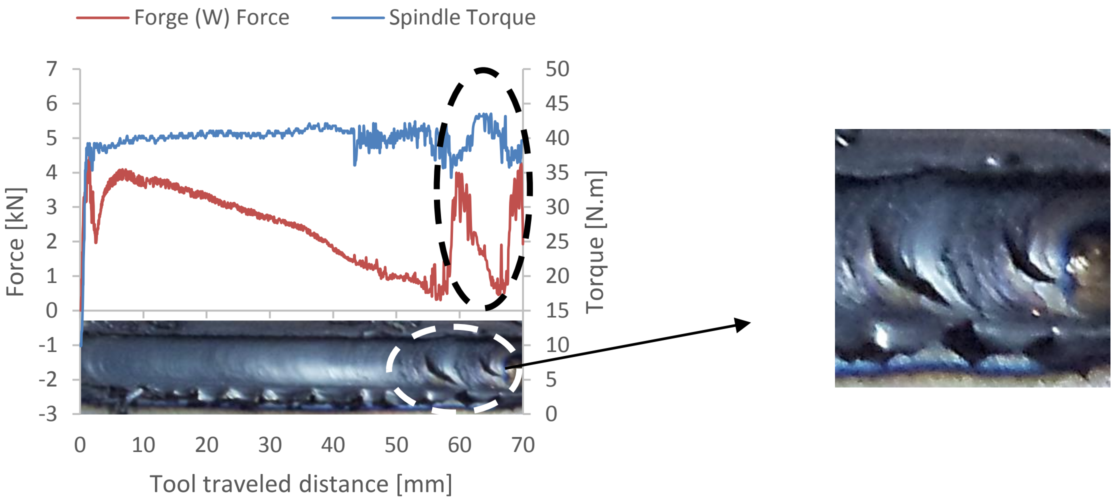

(a) Welding speed: 15 (5mm), 30 (10 mm), 40 mm/min, Plunging depth 1.65 mm

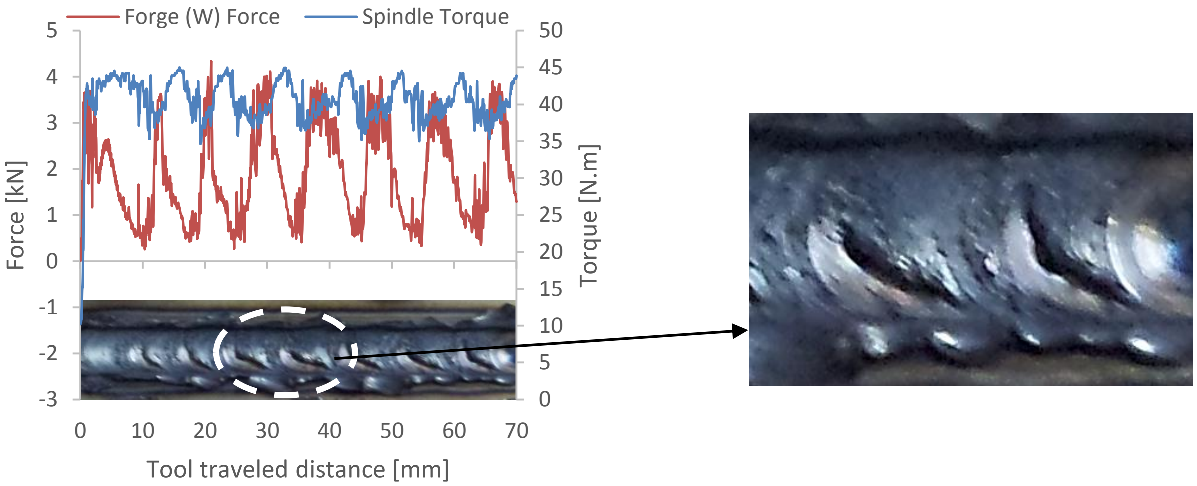

(b) Welding speed 15 (5mm), 30 (10 mm), 40 mm/min, Plunging depth 1.65 mm

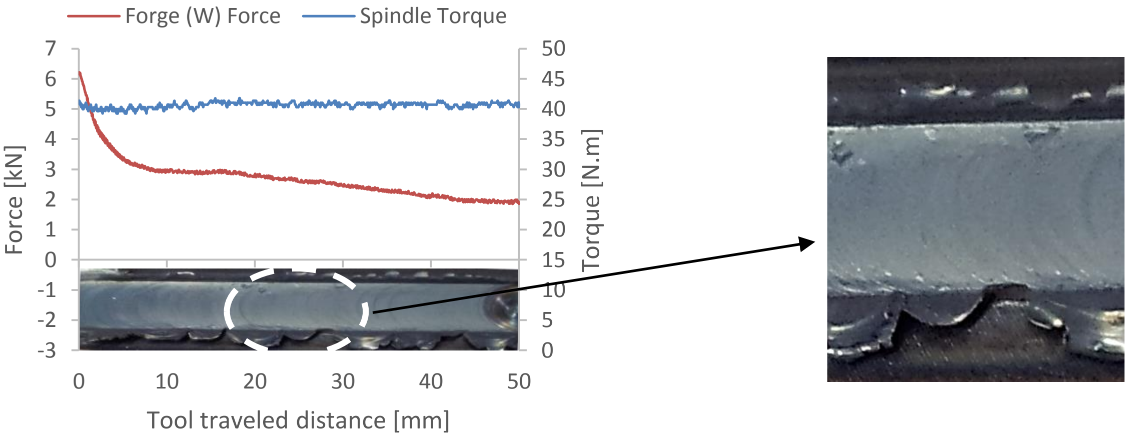

(c) Welding speed 15(5mm), 30(5mm), 40 mm/min, plunging depth 1.6 mm

Figure 5-3 Photographs of the weld beads with torque and axial force at 800 rpm

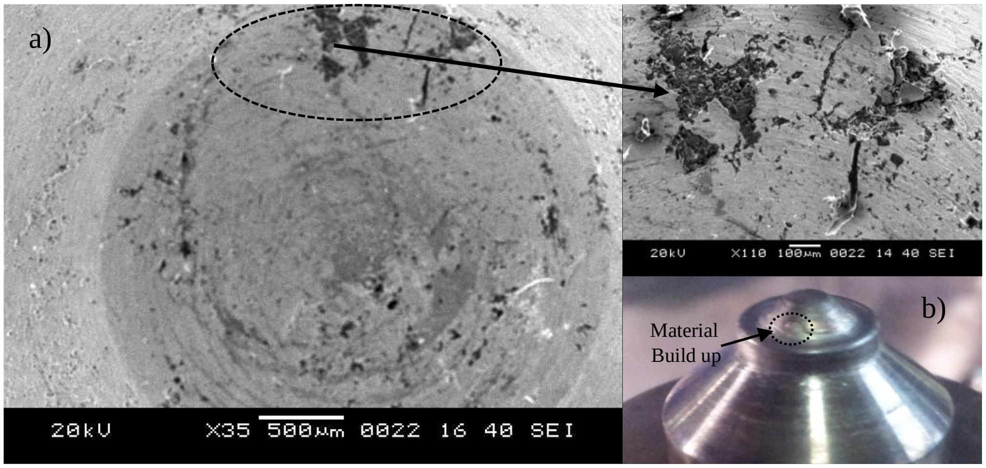

Figure 5-4 a) FESEM of tool b) builtup of base metal on tool

Moreover, the formed flash was larger and thicker as compared to other performed bead. At 2000 rpm, the generated bead surface shows repeated patterns of shoulder marks (Figure 5-6b). It may indicate that tool-machine dynamic characteristics play a role in identifying optimum process conditions and controlling joint and surface quality. From the obtained tool load- displacement results and bead surface images, it can be concluded that a more stable process could be achieved with better surface finish and smaller shoulder marks at lower tool rotational speeds. However, risk of material build up is more susceptible to occur in this case.

In welding, heat input or line energy is considered one of most important parameters that may affect weld quality. It is always preferable to perform welding at low heat input in order to avoid temperature related problems and defect, for example, residual stresses. Using the average recorded tool torque and rotational speeds together with Equations and (5.2), the line energy was calculated and presented in

Table 5-1 along with measured tool reaction loads. From

Table 5-1, the average recorded spindle torque in all beads was found to fall in the range of 30 and 40 N.m. Varying the tool rotational speed did not result in major changes in average torque, but it exhibited excessive fluctuations in tool loads, as mentioned previously. On the other hand, recorded axial force was found to decrease with increasing the tool rotational speed, where the average axial force was about 2500 N at 800 rpm. However, at higher rotational speeds (1500, 2000 rpm) it was dropped to 1000 N, but the heat input had increased.

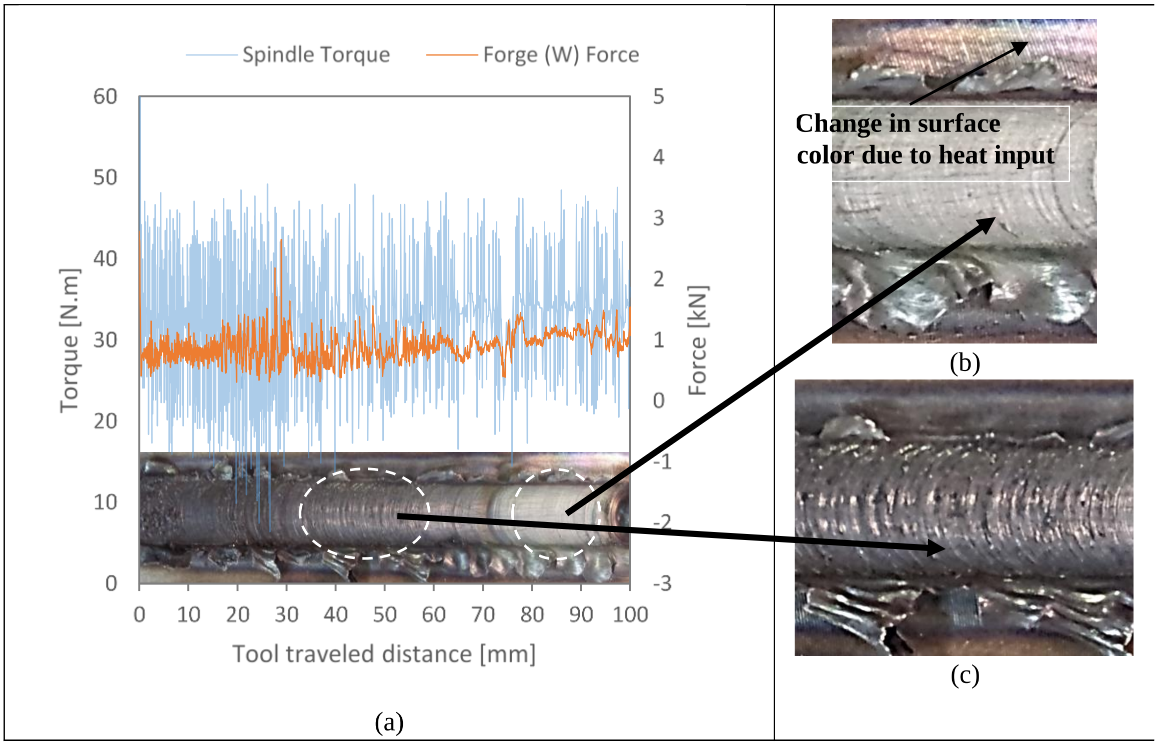

(a)

(b)

(c)

Figure 5-5 (a) welds with torque and axial force, 1500 rpm (b-c) onsets

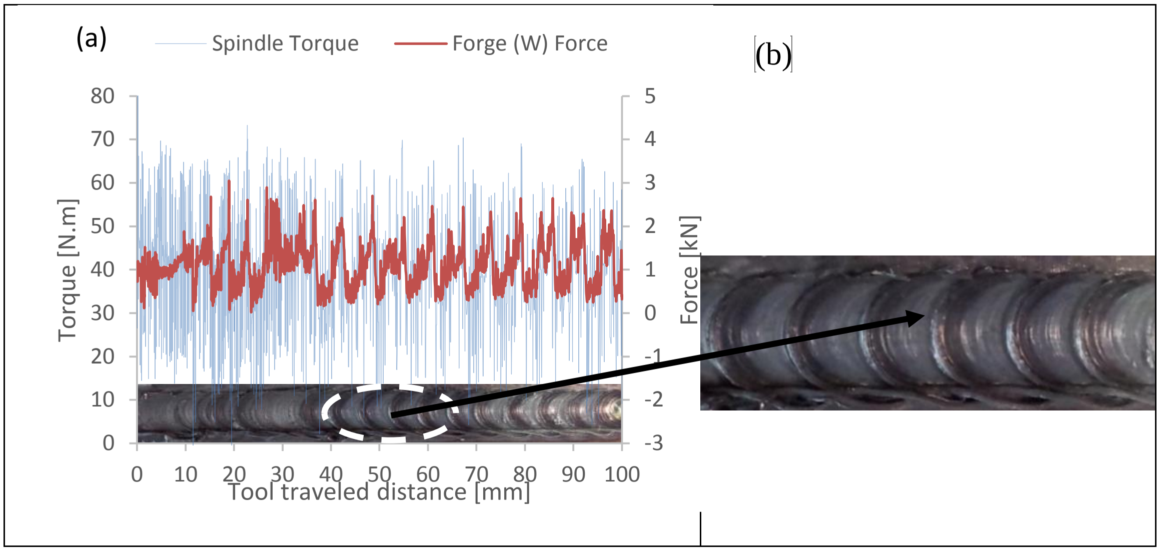

Figure 5-6 (a) welds with torque and axial force at 2000 rpm (b) onsets.

Table 5-1 Average recorded tool reaction loads and calculated heat input.

Tool Rotational Speed [rpm]	Average Tool Axial Force [N]	Average Tool Torque [N.m]	Average Heat Input [kJ/mm]	Maximum Tool Torque [N.m]
800	2443	41	1.8	41.7
1500	945	33	2.8	49
2000	1095	39	4.4	69

5.2.2 Influence of tool rotational speed on the microstructure

Figure 5-7 shows cross sections of the produced beads captured using optical magnifier. Beads were sectioned at locations where steady state condition was achieved (at welding speed of 40 mm/min) in order to study the impact of the tool rotational speed alone on the quality of the nugget. Optical magnifier and optical microscope were used to examine the different developed microstructural zones, material flow, and volumetric defects. At 800 rpm a sound bead was developed with no visible defect as shown in Figure 5-7a. Moreover, material flow contours were not visible. The welding process conditions may have resulted in a stable process for this bead. At higher rotational speeds, however, root defects in the nugget were observed, as shown in Figure 5-7b and Figure 5-7c. These defects may have been developed because of insufficient material flow at the tip of the tool pin. It can also be noticed that flow lines are more visible, due to excessive interruption in metal flow, which was ~~also~~ reflected on measured tool torque and axial force.

The nugget produced at low rotational speed has better smooth bead formation with small Heat Affected Zone (HAZ) due to stable and optimized process conditions. On the other hand, the nugget developed at high rotational speed (1500 and 2000 rpm) showed defects in the stir zones (SZ) below the tool pin toward the retreating side. The HAZ was about 0.9 mm in width for 800 rpm whereas it was found to be 1.8 mm for 1500 rpm and 2.4 mm wide for 2000 rpm. Similar behavior was reported in another study for welding speed used in tube-tubesheet welds where they found that increasing welding speed increases the size of the void formed in the nugget [18].

In all beads, the HAZ in the advancing side was wider as compared to the retreating side. This could be attributed to the asymmetry in temperature distribution about the weld centerline, as the temperatures at the advancing side are higher than those of the retreating side [57]. Moreover, HAZ was also found in wider at high rotational speeds as compared to lower ones. This was expected due to the increase in heat input. It was also evident that there is change in color around the bead indicating larger HAZ area around the nugget.

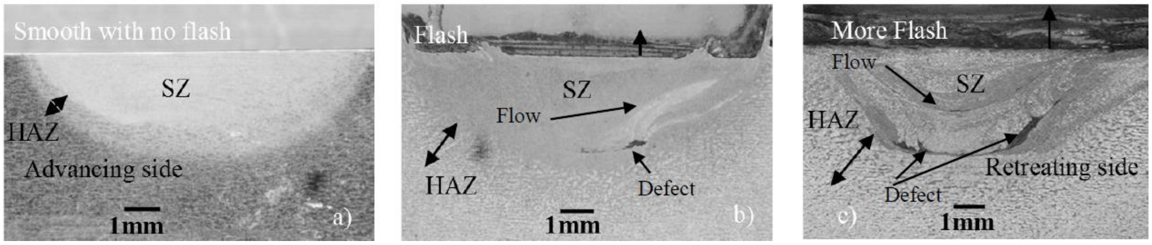

Figure 5-7 Quality of the bead at a) 800 rpm b) 1500 rpm c) 2000 rpm

Optical micrographs of the weld beads were examined at different regions of the bead to assess the effect of the pin tool rotation speed on microstructural features. Figure 5-8 shows the optical images of the base metal and friction stirred bead produced at 800 rpm. Figure 5-8 (a) and (b) depict the optical microscopic images of the parent metal, showing typical distinct phases of ferrite and pearlite. The as-received base metal exhibited a microstructure of ferrite grains approximately 20 to 30 µm in diameter ad smaller grains of fine pearlite. Grain size refining was observed in the SZ at all welding conditions and in all weld beads.

At 800 rpm tool rotation speed, equiaxed grains of almost 5 µm were generated as a result of thermomechanical actions during the welding process as shown in Figure 5-8c. When the rotational speed is increased to 1500 rpm, the grain-coarsening took place, which could be attributed to the increase in temperature and hence to increase in heat input. Further increase in rotation speed to 2000 RPM resulted in higher temperature softening and grain coarsening as compared to 1500 rpm conditions. The obtained results also confirm that axial forces were found to decrease with the increase of rotational speed resulting in a softening of the workpiece which is attributed to grain coarsening. Intense plastic deformation and heat input have resulted in recrystallization of the bead nugget at all investigated welding conditions. The recrystallization of the SZ produced fine grain microstructure, which is of significant importance in post-weld hardness.

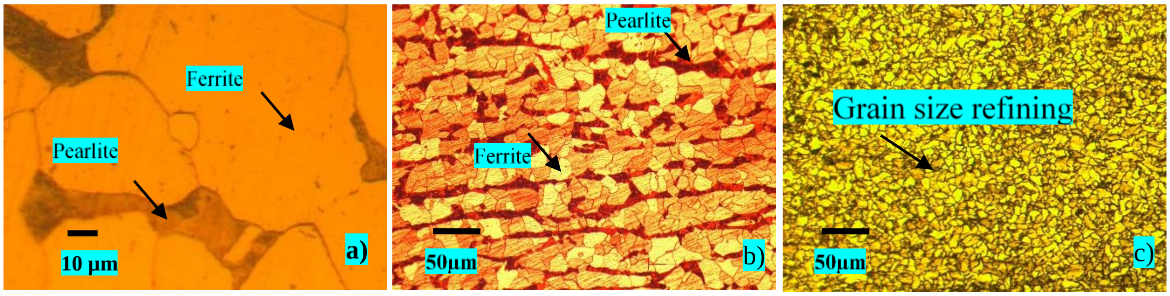

Figure 5-8 Optical images (a) base metal, 500X (b) 200X (c) SZ 800 rpm, 200X.

Figure 5-9 shows microstructurally distinct regions namely SZ along the bead centerline, HAZ around the SZ of the beads. No TMAZ (Thermomechanical Affected Zone) was seen in the steel beads, which is unlike to aluminium alloys. In Figure 5-9a, ferrite and pearlite on the advancing side were partially dissolved showing no distint phases of ferrite and pearlite due to higher temperature on the advancing side. At higher rotational speed, however, more grain coarsening was observed in the HAZ region adjacent to SZ as shown in Figure 5-9c and Figure 5-9d. It is believed that temperature of the SZ is greater than that of the HAZ. Normally FSW processes of steel generates temperature arouund around 1200°C [58].

The HAZ has no apparent deformation during FSW. Therefore, microstructural evolution in the various regions of the HAZ of the steel can be compared to Fe-Fe_3C phase diagram. It was also reported that grain coarsened region of HAZ experienced the highest temperature and results of the some other researcher showed that temperature is above A3 line temperature in the phase diagram meaning that the grain growth of the austenite will be inevitable[59]. Existence of any TMAZ was probably lost due to decomposition of austenite during cooling.

The microstural investigation of the SZ is not an easy task as it is depicted in HAZ. It is also worth mentioning that microstural evolution in FSW of steel is consistent with continous cooling curve of the arc welding of similar steels [60]. In fact, the HAZ bears only a thermal cycle, whereas the SZ experiences both thermal and mechanical cycles so both processes will be considered to discuss the evolution of phases in the SZ. Actually during FSW of steel, dynamic recovery, dynamic recrystallization, and metadynamic recrystallization in those regions, which are near the tool shoulder that bears large strain near the surface [61]. Large strain will increase the grain size refinement. Therefore, the SZ will experience an increase in grain size refinement as compared to other bead zones. For the remaining zones including the bottom of the bead, they will experience lower strain and slow cooling rates resulting in an increase in grain coarseing.

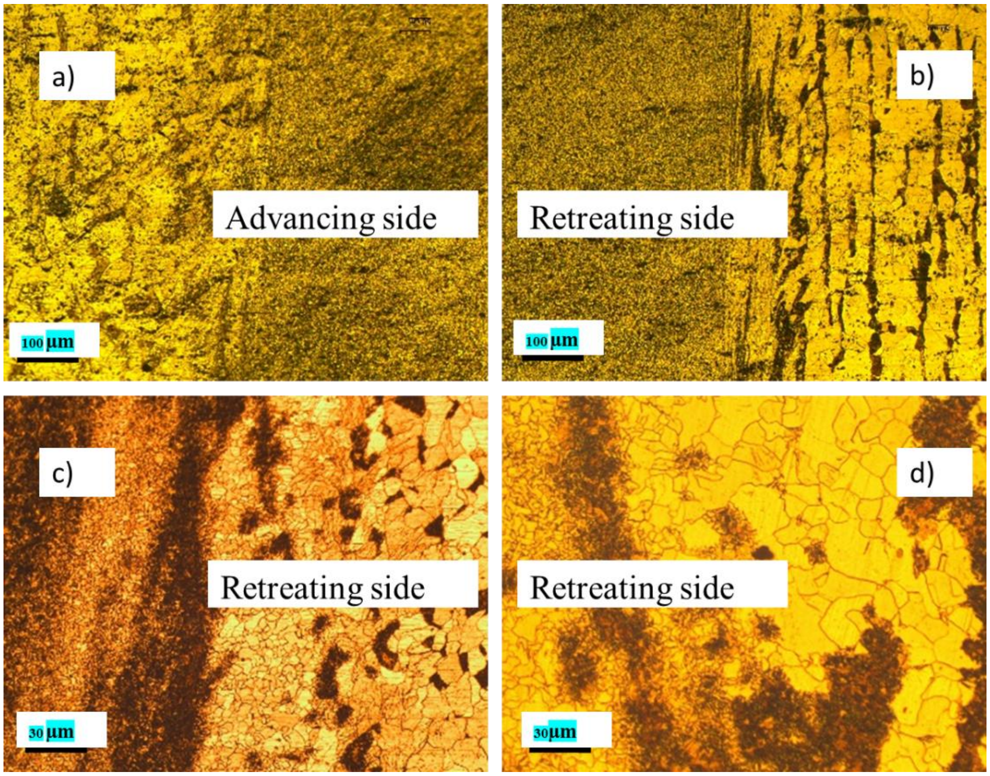

Figure 5-9 Optical images of HAZ (a &b) 800 rpm, c)1500 rpm d) 2000 rpm

5.2.3 Influence of tool rotational speed on bead Microhardness

Figure 5-10 shows hardness of beads produced at different rotational speeds and constant welding speed of 40mm/min. The hardness of the base metal was 135±3 VHN. Microhardness of the SZ portion of the weld bead was found to be greater than those of the surrounding zones including the BM and the HAZ. This was expected due to the grain size refinement that resulted from thermomechanical cycles in the SZ. The highest microhardness values were obtained at 800 rpm. Microhardness values ranges from 275-310 VHN for 800 rpm. The increase in hardness values could be attributed to refined microstructure. Moreover, lower rotational speed will generate lower temperature that will prevent grain growth. At higher rotational speed (2000 rpm), however, grain coarsening occurred and hardness decreased drastically. Hardness values recorded in the SZ were found to vary from 200 to 240 VHN.

Similar observations were found by A. Pradeep and S. Muthukumaran [64]. Same trends were observed when hardness analysis was conducted along the depth of the bead as shown in Figure 5-11. Microhardness values decrease from top to bottom of the bead. Higher hardness at top surface could be attributed to high strain and high cooling rates due to direct contact of tool shoulder with the workpiece. The remaining regions were having lower hardness due to low strain and cooling rates.

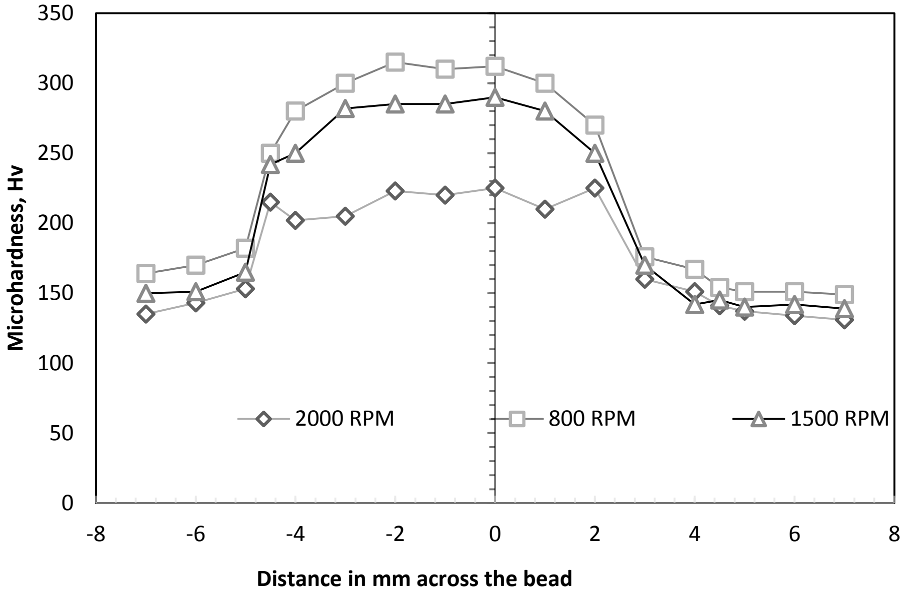

Figure 5-10 Microhardness across the weld bead made at different rotation speeds

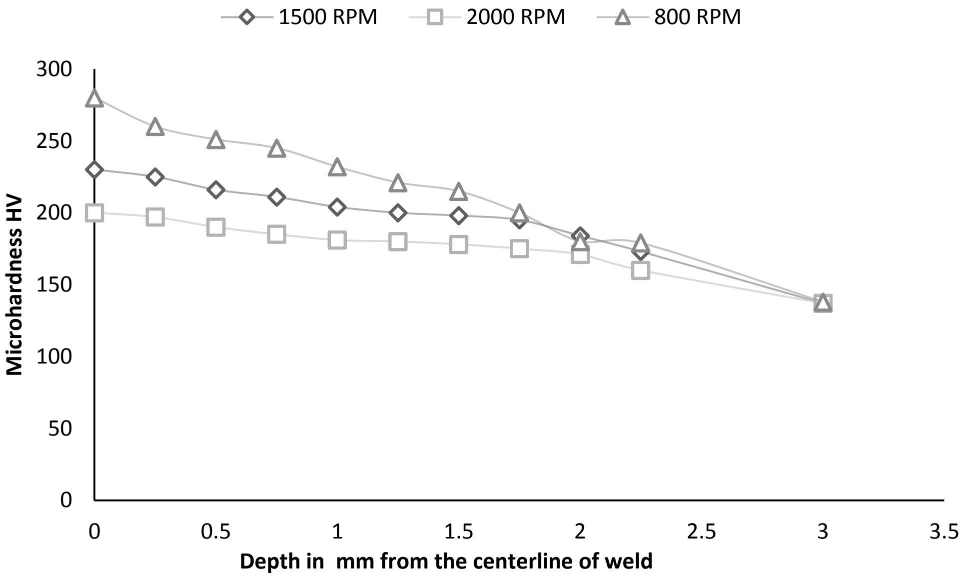

Figure 5-11 Microhardness along the depth at different rotational speed

5.2.4 Influence of tool rotational speed and travel distance on tool wear

The W-25%Re tool under investigation has traveled almost 3.5 m, and performed over 50 plunges. The tool pin plunging depth was initially 1.60 mm, and after traveling for more than 3 meters, the plunging depth increased to about 2.2 mm, this is due to changes in the diameters and lengths of the shoulder and pin. Figure 5-12 shows the average values of the axial force, traverse (welding) force, and torque on the travel distance, i.e. the length of the beads made by the tool, when friction steel welding the steel plates at welding speed of 40 mm/min and spindle rotation of 800 rpm. The rotational speed is proportional to the tool life in service. The Figure 5-12 indicates that traverse (welding) force increases with the tool life whereas the torque decreases with the increase in tool life. This is due to the wear and mechanical deformation of the pin tool.

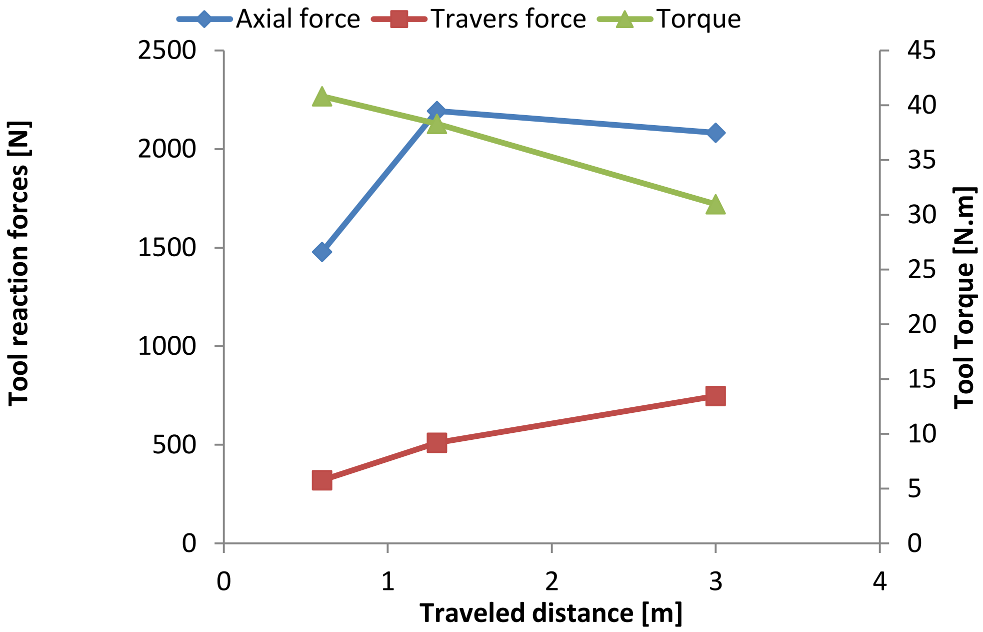

Figure 5-12 Effect of pin tool travel distance on pin tool forces and torque

Table 5-2 shows chemical analysis of the base metal and weld bead used in the present work. The analysis of the base metal shows that it has typical mild steel composition. The chemical analysis was perfored using spectrometer. The analysis was conducted to study and understand the effect of rotational speed on tool wear. The analysis of the base metal shows that it has 0.0209wt% tungsten.

Figure 5-13 shows the graph for the corresponding Table 5-2 It is noticed that increasing the rotational speed resulted in an increase in the Tungsten contents of the weld bead. This phenomenon could be attributed to the rise in temperature with the increase of rotational speed. As a result, more diffusion of tool material to the weld nugget is obtained.

Table 5-2 Spectroscopy analysis of the bead developed

Specimens	**wt% C**	**wt% Si**	**wt% Mn**	**wt% P**	**wt% S**	**wt% W**
Base Metal	0.244	0.241	1.09	0.011	0.008	0.0209
800 RPM	0.261	0.200	0.912	0.0053	0.0031	0.0951
1000 RPM	0.294	0.263	0.912	0.0077	0.0048	0.119
1500 RPM	0.250	0.225	0.917	0.0081	0.0057	0.4825
2000 RPM	0.264	0.238	0.909	0.0062	0.0048	0.855

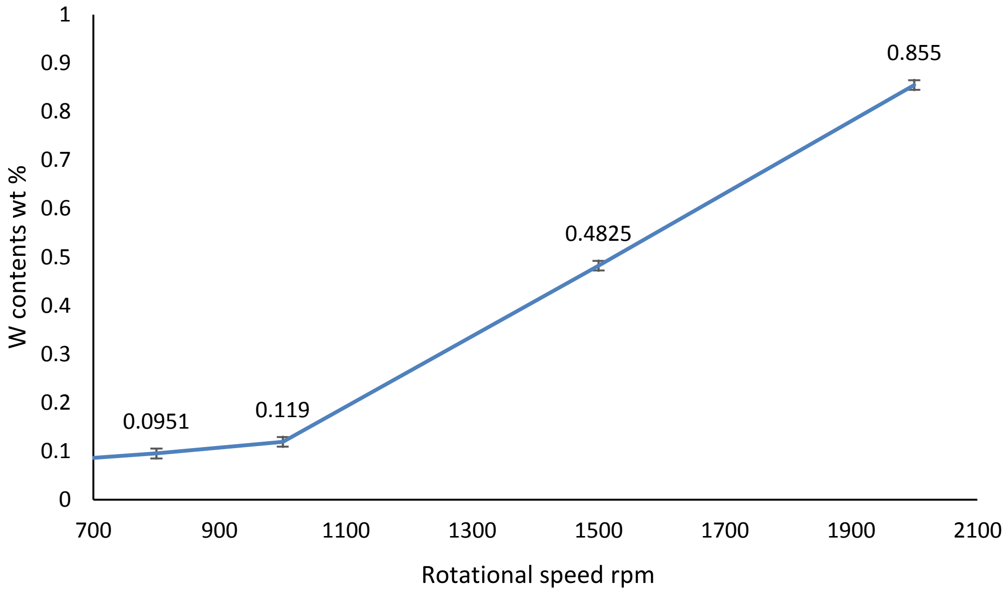

Figure 5-13 Effect of rpm on the diffusion of tungsten from the tool to bead nugget

Figure 5-14 (a) and (b) shows the initial tool tip pin and shoulder length. Overall, the tool had experienced severe conditions of fluctuating forces and higher thermal input which resulted in wear out and plastic deformation of the tool shoulder and pin. After covering a

3.5m distance in more than 50 plunges, the tool shoulder shank deformed significantly as it was shortened by 0.8 mm as shown in Figure 5-14 (c) after the tool had traveled an accumulative welding distance of 3.5 meter. It is well known that tool shoulder is mainly responsible for the frictional heat generation. Therefore, it is subjected to severe thermal and mechanical harsh conditions of FSW. It can be seen that the length of the pin increased by 0.6 mm as shown in Figure 5-14 (d).

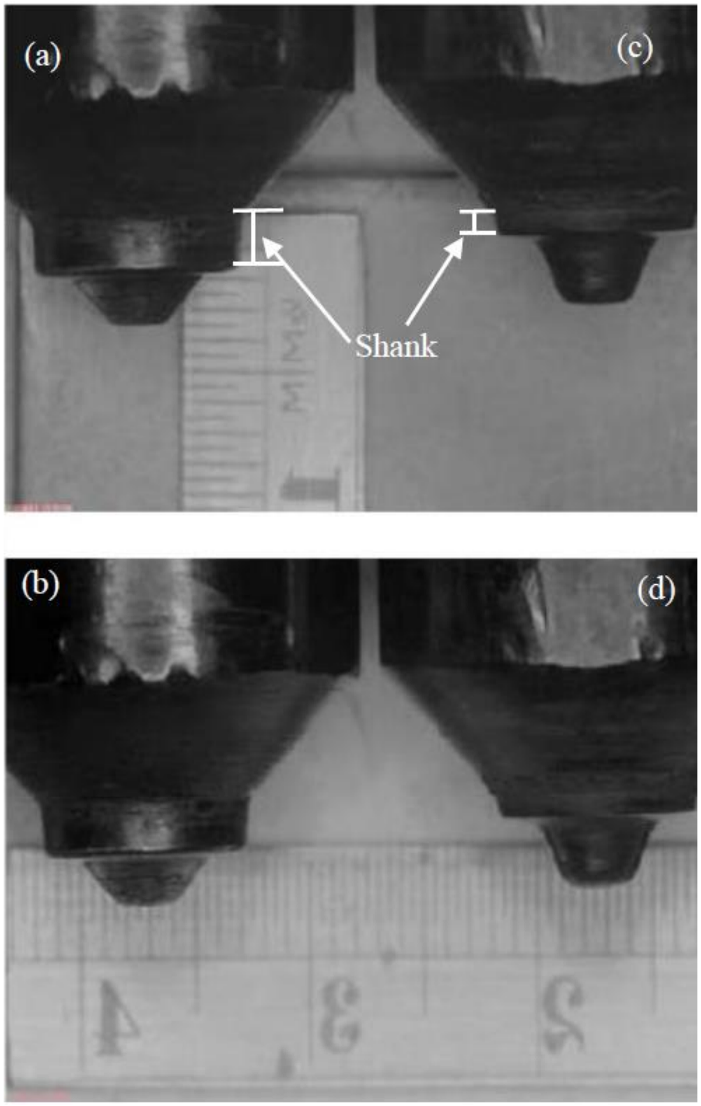

Figure 5-14 (a) and (b) initial shape of the tool (c) and (d) worn tool

This change in length is due to the wear of the tool shoulder shank and the effects of competing mechanical deformation mechanisms acting on the pin tool. By calculating the tool pin and shoulder shank volume for the tool in its initial use and after 3 m of welding, it was found that the tool pin shoulder volume dropped by 40%. Similar observations on excessive wear of W-25% Re tool were reported by Shuaib et al. [65] where it was stated that abrasion wear was the main wear mechanism. In addition, creep may also take place due to excessive process temperature while welding steel.

5.3 Findings

Table 5-3 shows the base line parameters which may be consulted for the newly developed nanocrystallline tool.

Table 5-3 Base line parameters obtained during the FSW of mild steel

Category	**Parameter/Process**	**Category**	**Parameter/Process**
Process	FSW	Tool Material	W-25wt%Re
Spindle rotational speed	800 RPM	Materials Joined	ASTM A516 Grade 70
Spindle tilt angle	0.1°	Type of weld joint	Butt joint
Dwell time	3 sec	Control	Displacement control
Penetration depth	1.6mm	Torque	40 N.M
Plunging rate	5 mm/min	Forging force, Fz	2500 N
Welding speed	15 mm/min to 40 mm/min	Traverse forces, Fx and Fy	400 N
Microhardness Hv	286 ± 3	Thermal conductivity	45-50 $Wm^{-1} k^{-1}$

Conclusions that can be drawn from this investigation include:

1. Using small pin tool, defect free bead-on plate, with good surface finish and intensive grain refinement was achieved at 800 rpm. Low rotational speeds are recommended for the newly developed tool.
2. At high rotational speeds grain growth occurs due to increase in temperature and consequently, axial force decreases. In HAZ, more grain growth was observed at high rotational speed.
3. The spectroscopy results have shown the presence of W in the weld bead in the range of 0.0951 to 0.855 wt%. This is due to tool material transfer to the weldment through competing wear mechanisms including diffusion, abrasion, and chipping. This requires additional future studies to identify the dominant wear mechanisms and to evaluate the effects of welding parameters. Lower rotational speed will reduce the diffusional wear.
4. Stick and slip actions during the FSW results adhesive wear of the tool
5. Moreover, shoulder found to be more prone to wear compared to tool pin

5.4 Important considerations

The wear of the tool shoulder could be attributed to abrasive wear (removal of material or thinning of shoulder height), adhesive wear (due to stick slip action during the FSW process) and diffusional wear (as indicated by the spectroscopy analysis of the beads).

The wear resistant of the tool materials can be improved by synthesizing them using a combination of novel techniques such MA and SPS. W-25% Re can be reinforced with HfC to improve the abrasive wear resistance. Tool life is depended on the tool degradation during friction stir welding. Metallurgical challenges which will affect tool life are crystallite size of the matrix, homogenous dispersion of second phase in the matrix. Nanocrystallinity of the alloy is difficult to retain by conventional consolidating techniques as it involves longer sintering duration. So these challenges are difficult to address by using these techniques. Therefore, the author proposes using such techniques as mechanical alloying and spark plasma sintering to prepare W-xRe pin tools to overcome these challenges during welding steels.

5.5 Performance evaluation of fully alloyed nanocrystalline tool

In the last part of the thesis, Friction Stir Spot Welding FSSW preliminary tests were conducted on thin mild steel sheets by using disc shape nanocrystalline tool in order to investigate its feasibility for the process. Most of the base line parameters used in this investigation were consulted from the outcome of the previous chapter.

5.5.1 Friction stir welding of thin mild sheet

In order to evaluate the performance of the developed tool material under the harsh conditions of Friction Stir Spot Welding of steel, preliminary results are presented here. Fully alloyed W-25wt%Re tool in cylindrical disc shape was used in Friction Spot Welding of 2mm thin mild steel in order to confirm the soundness and suitability of tool for FSW of steel. AISI 4140 alloy steel holder was manufactured to grip the tool during the process. Fully instrumented MTI (Manufacturing Technology Inc.) Model RM-1 friction stir welding machine was used to perform the FSSW tests. Welding speed was 40 mm/min, with tool rotational speeds of 400, 500 and 600 rpm for all the experiments. The machine tilt angle was 0^o and dwell time was fixed to 5 seconds. Argon gas was used as shielding gas during the friction stir welding in order to avoid the oxidation of the base metal as well as the surface of the tool. Temperature was recorded during the process using telemetry system installed with the set up.

Initially, fully alloyed W-25%Re disc sintered at 1800°C was used as a tool to join the thin sheets. The disc type tool and the tool holder shank were manufactured in the machine lab as shown in Figure 5-15 (a-d). A provision for the thermocouple in the tool holder was created near the tool surface for the measurement of temperature developed during the process. It was difficult to machine and grip the tool in machining set up as the tool was only 4 mm in height as presented in Figure 5-15 (b). Milling operation was successful on composite disc containing 5vol% HfC however it offered a resistance to machining due the presence of hard HfC particle as shown in Figure 5-15e). Composite samples have also lower thermal conductivity as discussed in earlier section. Lower thermal conductivity of the tool can produce localized heating of the workpiece resulting in hotspot in the welds.

Figure 5-15 a) Tool shape b) machining (c-d) tool holder e) 5vol% HfC

Figure 5-16 (a-c) shows W-25%Re tool along with the tool holder assembly. The test was performed using a rotational speed of 400 rpm and with a welding speed of 40mm/min.

During this process tool holder became soft due to frictional heat between tool and workpiece and finally it deformed in later stages as shown in Figure 5-16 d). It happened because the tool holder was not at all heat treated and does not have sufficient strength to sustain the load during the process. It is also evident that the process did not develop the sufficient heat input in the early part of the experiment and the disc tool was slipped from the tool holder as shown in Figure 5-16 e) however, sufficient heat was generated at the end of the process to produce a spot weld as shown in Figure 5-16 f). Maximum temperature was recorded around 750^{o}C during the process. However during this sever damage of the tool holder, tool showed excellent resistance to any damage or wear except some slippage marks as shown in Figure 5-17. Tool pin was 2 mm in height and it did not change after the experiment.

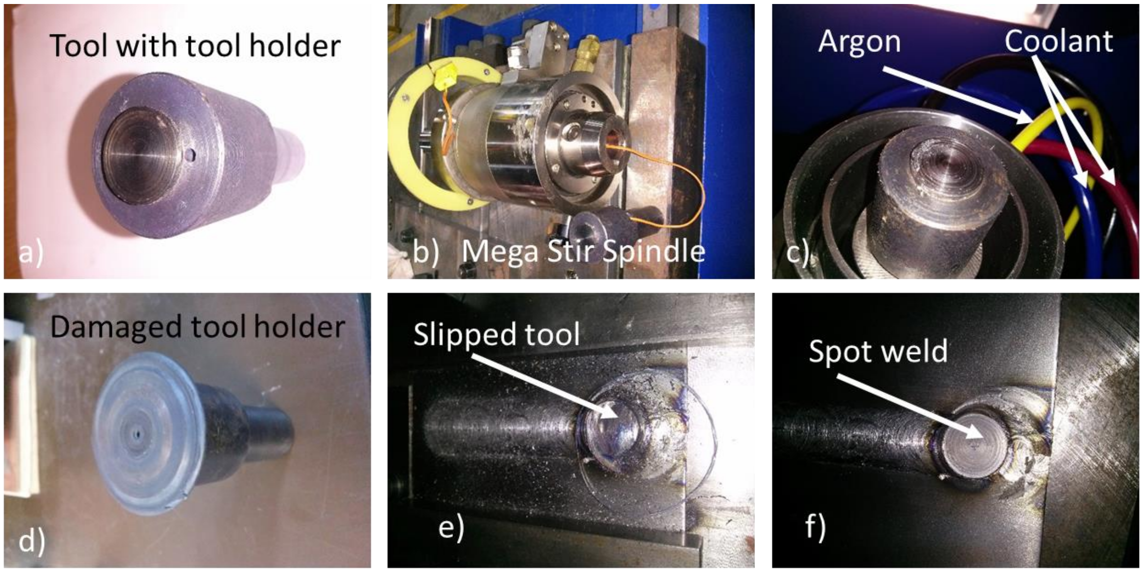

Figure 5-16 a) press-fit tool b) assembly c) Fitted tool d) holder e) slipping f) FSSW.

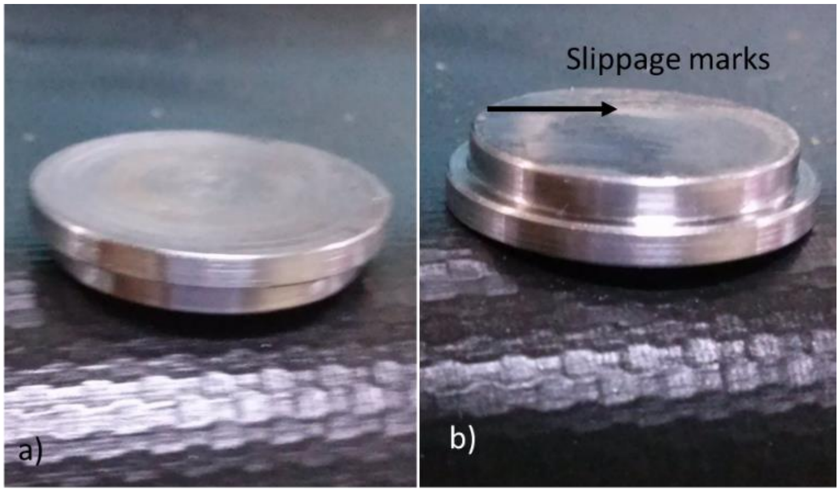

Figure 5-17 Tool appearance a) before b) after the first test.

5.5.2 Friction stir spot welding of thin mild sheet

New tool holder was manufactured from AISI 4140 alloy steel. A heat treatment was performed on the tool holder to make it harder and stronger. Tool holder was heated at 845°C (1550°F) followed by quenching in oil. After hardening the alloy was given as tempering treatment to get an appropriate hardness of 54 HRC. The tool was retraced and machined with new geometry as shown in Figure 5-18 a). Friction Stir Spot Welding was performed on the workpiece with a rotational speed of 500 and 600 rpm as shown in Figure 5-18b). The process produced good quality spot welds. Spot weld 1 was performed with a rotational speed of 600rpm that shows a wider heat affected zone when compared to spot weld 2 produced at 500 rpm. There were no visible defects in weld zones. The tool showed an excellent resistance to any physical or dimensional changes after these tests.

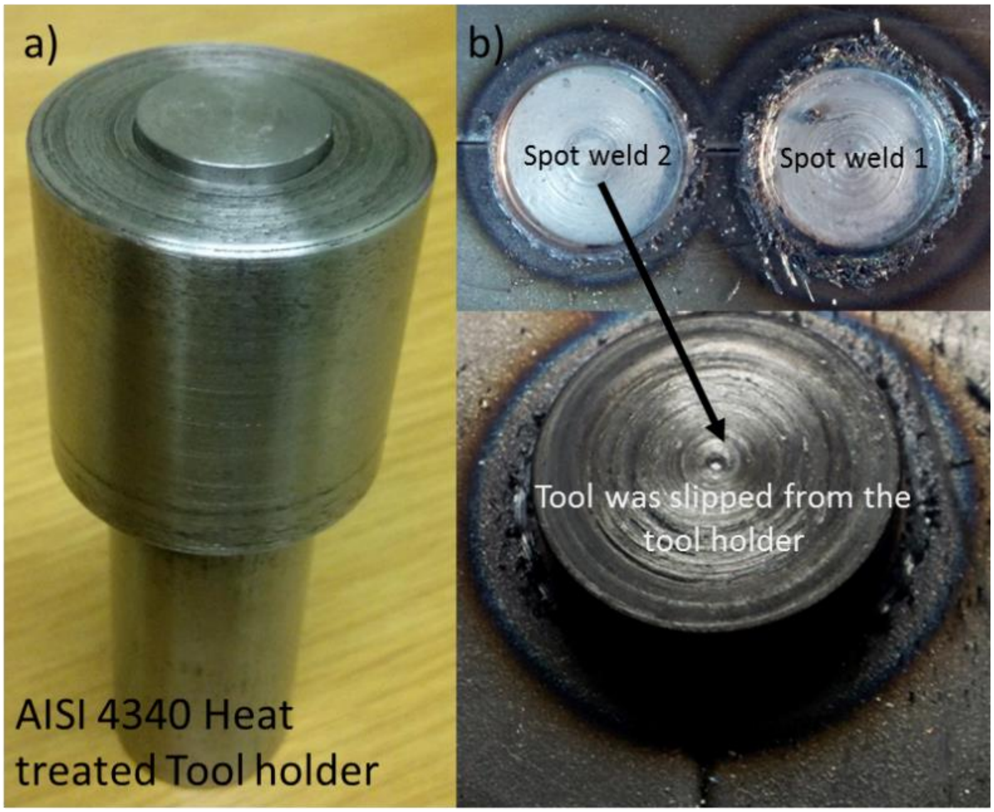

Figure 5-18 a) Tool along with tool holder b) Spot welds with overlying slipped tool.

5.5.3 Optical microscopy

Figure 5-19a) shows the optical image of the base metal and nugget junction of friction stir weld produced at 600 rpm. Parent base mild steel shows typical distinct phases of ferrite and pearlite. Grain size refining was observed in the SZ which could be attributed to the increase in temperature during the process as shown in Figure 5-19 (b-c). The process temperature of SZ must be in austenitic zone of Fe-Fe carbide diagram in order to justify the grain size refining phenomenon.

Figure 5-20 (a, b) shows cross sections of the spot weld produced at rotational speed of 500 and 600 rpm respectively. Both conditions produced sound weld cross sections with no visible defect. It was also observed that HAZ was in large spread for FSW spot welded at 600 rpm compared to 500 rpm.

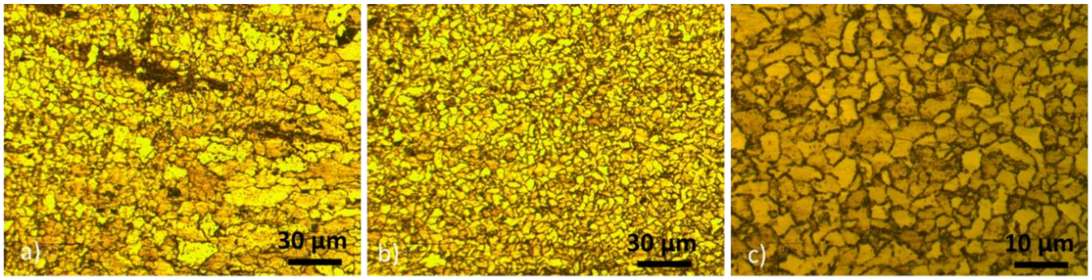

Figure 5-19 Optical images of FSSW at 800RPM (a) junction (b-c) SZ.

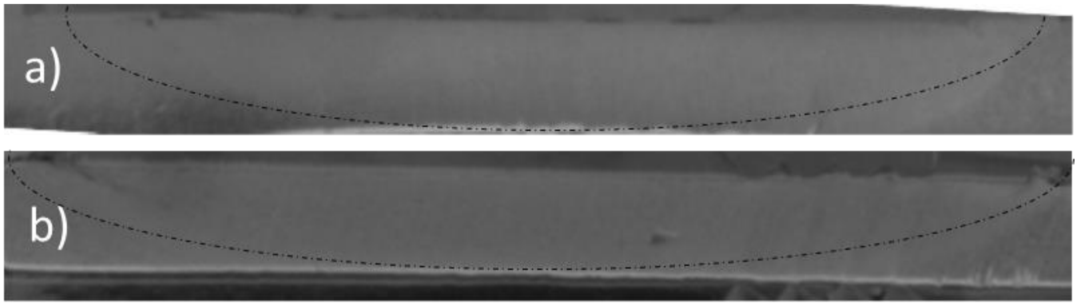

Figure 5-20 Quality of the bead at different conditions a) 500 rpm b) 600 rpm

Figure 5-21 shows the effect of rotational speed on the diffusion of W contents into the weld. It can be pointed out that when the rotational speed was increased, relatively increase in tungsten contents was observed in the base metal. This phenomena was attributed to the increase in temperature with the increase of rotational speed and hence more diffusion of the tool material to the base metal.

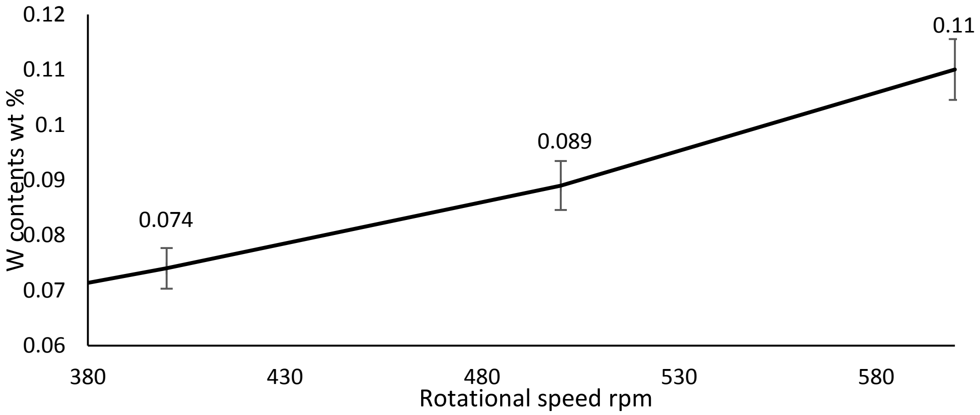

Figure 5-21 Diffusional wear vs rotational speed

CHAPTER 6

CONCLUSIONS AND RECOMMENDATIONS

In this research work, mechanical alloying and spark plasma sintering techniques were used to develop an experimental pin tool disc for friction stir welding of steels. The specific conclusion from the investigation are summarized in the following points:

1. Dense nanocrystalline W-25%Re alloy and W-25%Re-HfC composite material with nanostructured matrix and uniform distribution of the reinforcement was successfully developed by mechanical alloying and spark plasma techniques.
2. A single nanostructured W-25wt%Re solid solution with a crystallite size of 13 nm was developed.
3. The crystallite size of the matrix phase in the sintered composites remained in the nanometer range and did not exceed 100 nm.
4. The composite containing 10 vol. % of HfC possessed the highest Vickers hardness value of 495 but with lowest thermal conductivity.
5. Wear resistance of monolithic SPSed fully alloyed was improved with sintering temperature.
6. The dominant wear mechanisms for the W-25Re alloy and the composite were found abrasive and adhesive respectively. Specific wear resistance of the alloy was further improved with the addition of 5vol% HfC.
7. The developed composite showed lower average coefficient of friction compared to its monolithic counterparts.

8. The newly developed experimental nanocrystalline fully alloyed W-25wt%Re tool disc was used for friction stir spot welding of mild steel. The tool showed excellent resistance to abrasion, adhesion and diffusional wear during the severe and harsh conditions of FSW of steel.
9. Good quality spot welds with no visible defects were produced using low tool rotational speeds of 400, 500 and 600 rpm at constant welding speed of 40 mm/min.

6.1 Key contribution

The present research work has successfully addressed one of the key challenges in the development of tool for high temperature applications such as Friction Stir Welding (FSW) of steels. W-25%Re based tool materials are difficult to synthesize and consolidate by conventional means. Nanocrystalline W-25%Re tool was successfully developed by a combination of mechanical alloying and spark plasma sintering. The tool was used in real time experiments for friction stir spot welding of steel. The tool has shown excellent performance under the harsh condition of FSW of steel.

6.2 Recommendations

In future, it would be recommended to carry out a comprehensive study on fracture toughness of SPSed W-Re alloy and W-Re-HfC composites. Fracture toughness is one of the most important property of FSW tool design specially during plunging stage. Fracture toughness will provide a quantitative analysis of the FSW tool to resist crack propagation. A variant of temperature and reinforcement contents would be utilized to explore the ability of the tool to resist the failure.

Titanium carbide (TiC) coatings on monolithic nanorcystallline W-25wt%Re alloy and composite would enhance the performance of the FSW tool. The coating could be deposited by Physical Vapor Deposition (PVD) or Chemical Vapor Deposition (CVD). TiC is extremely hard refractory ceramic material and it could be used for FSW of steel and titanium alloys at high welding and rotational speed due its high elastic modulus (400GPa) and shear modulus (188GPa).

REFERENCES

[1] W. Konig and A. Neises: ‘Wear mechanisms of ultrahard, nonmetallic cutting materials’, Wear, 1993, 162, 12–21.

[2] M. Senmweldi and C. Metals, “ADVANCES IN TOOLING MATERIALS FOR FRICTION,” pp. 1–11, 1991.

[3] Y.Gao, and R. H. Wagoner, "A simplified model for heat generation during the uniaxial tensile test", Metallurgical Transactions, 18A: 1001–1009,1987.

[4] H. C. Braga, , and R. A. Barbosa, "Simulation of the increase in temperature due to adiabatic heating in hot deformation processes", Proceedings of 47th Brazilian Association of Metallurgy and Materials (ABM) Annual Conference, pp. 441–457, ABM,1992

[5] A. C. Nunes, E. L. Jr., Bernstein, and J. C. McClure, "A rotating plug model for friction stir welding", 81st American Welding Society Annual Convention. Chicago, IL; April 26-28, 2000.

[6] L. E. Murr, G. Liu, and J. C. McClure, "A TEM study of precipitation and related microstructures in friction stir welded 6061 aluminum" Journal of Materials Science, 33: 1243–1251, 1998.

[7] C. G. Rhodes, M. W.Mahoney, W. H. Bingel, R. A.Spurling, and C. C. Bampton, "Effects of friction stir welding on microstructure of 7075 aluminum" Scripta Materiala, 36(1): 69–75, 1997.

[8] M. W. Mahoney, C. G. Rhodes, J. G. Flintoff, W. H. Bingel, and R. A. Spurling, "Properties of friction stir welded 7075 T651 aluminum" Metallurgical and Materials Transactions 29A: 1955–1964, 1998.

[9] T. Weinberger, N. Enzinger, and H. Cerjak, “Microstructural and mechanical characterisation of friction stir welded 15–5PH steel” Sci. Technol. Weld. Join, vol. 3, no. 14, pp. 210–215, 2009.

[10] S. Park, Y. Sato, H. Kokawa, K. Okamoto, S. Hirano and M. Inagaki: ‘Boride formation induced by pcBN tool wear in friction-stir-welded stainless steels’, Metall. Mater. Trans. A, 2009 40A, (3), 625–636.

[11] P. L. Raffo, “Yielding and fracture in tungsten and tungsten rhenium alloys ” J. Less Common Met., vol. 2, no. 17, pp. 133–149, 1969.

[12] R. Rai, H. K. D. H. Bhadeshia, and T. Debroy, “Review : friction stir welding tools,” Sci. Technol., vol. 16, no. 4, pp. 325–342, 2011.

[13] S. Campbell and W. Kaczmarek, “Mössbauer Spectroscopy Applied to Materials and Magnetism,” (G. J. Long F. Gd. Eds.) Plenum Press. New York, vol. 2, p. 273

[14] C.Y. Xu, S.S. Jia, Z.Y. Cao, Synthesis of Al–Mn–Ce alloy by the spark plasma sintering, Mater. Charact. 54 (2005) 394–398.

[15] X.L. Shi, H. Yang, S. Wang, Spark plasma sintering of W–15Cu alloy from ultrafine compositepowder prepared by spray drying and calcining continuous reduction technology, Mater. Charact. 60 (2009) 133–137.

[16] Saheb, N., Iqbal, Z., Khalil, A., Hakeem, A.S., Al-Aqeeli, N., Laoui, T., Al-Qutub, A., Kirchner, R., Spark plasma sintering of metals and metal matrix nanocomposites: A review, Journal of Nanomaterials, Volume 2012, Article ID 983470, 1-13, 2012.

[17] W.M. Thomas, E.D. Nicholas, J.C. Needham, M.G. Murch, P. Templesmith, and C.J. Dawes, International Patent pplication PCT/GB92/02203 and GB Patent Application 9125978.8, 1991

[18] F. A. Al-Badour, N. Merah, A. N. Shuaib, and A. Bazoune, “Experimental Investigation of Friction Stir Seal Welding of Tube-Tubesheet” Journal of Pressure Vessel Technology, Vol. 137/ 011402, 2015.

[19] K. Brookes, “There ’ s more to hard materials than tungsten carbide alone,” Met. Powder Rep., vol. 66, no. 2, pp. 36–37,39–45, 2011.

[20] K. Cho, L. Kecskes, R. Dowding, B. Schuster, Q. Wei, and R. Z. Valiev, “Nanocrystalline and Ultra-Fine Grained Tungsten for Kinetic Energy Penetrator and Warhead Liner Applications,” Mater. Res., no. June, 2007.

[21] E. Y. Ivanov, C. Suryanarayana, and B. D. Bryskin, “Synthesis of a nanocrystalline W – 25 wt .% Re alloy by mechanical alloying,” vol. 251, pp. 255–261, 1998.

[22] Jonathan A. Webb Indrajit Charit Cory Sparks Darryl P. Butt Megan Frary Mark Carroll, “SPS Fabrication of Tungsten-Rhenium Alloys in Support of NTR” Fuels Development, Nuclear and Emerging Technologies for Space 2011, INL/CON-10-20354

[23] S. N. Alam, “Synthesis and characterization of W–Cu nanocomposites developed by mechanical alloying,” Mater. Sci. Eng. A, vol. 433, no. 1–2, pp. 161–168, Oct. 2006.

[24] F. Jing-lian, L. Tao, C. Hui-chao, and W. Deng-long, “Preparation of fine grain tungsten heavy alloy with high properties by mechanical alloying and yttrium oxide addition,” J. Mater. Process. Technol., vol. 208, no. 1–3, pp. 463–469, Nov. 2008.

[25] N. Ünal, “Mechanical means help make better tungsten matrix composites,” Met. Powder Rep., vol. 63, no. 10, pp. 28–33, Nov. 2008.

[26] M. a. Yar, S. Wahlberg, H. Bergqvist, H. G. Salem, M. Johnsson, and M. Muhammed, “Spark plasma sintering of tungsten–yttrium oxide composites from chemically synthesized nanopowders and microstructural characterization,” J. Nucl. Mater., vol. 412, no. 2, pp. 227–232, May 2011.

[27] Y. Kim, K. H. Lee, E.-P. Kim, D.-I. Cheong, and S. H. Hong, “Fabrication of high temperature oxides dispersion strengthened tungsten composites by spark plasma sintering process,” Int. J. Refract. Met. Hard Mater., vol. 27, no. 5, pp. 842–846, Sep. 2009.

[28] J. Lee, J.-H. Kim, and S. Kang, “Advanced W-HfC Cermet using In-Situ Powder and Spark Plasma Sintering,” J. Alloys Compd., Oct. 2012.

[29] H. Park, H. Youn, J. Ryu, H. Son, H. Bang, and I. Shon, “Fabrication and mechanical properties of WC-10 wt .% Co hard materials for a friction stir welding tool application by a spark plasma sintering process,” vol. 13, no. 6, pp. 705–712, 2012.

[30] Luo, K. S. Shin, and D. L. Jacobson, “Hafnium carbide strengthening in a tungsten-rhenium matrix at ultrahigh temperatures,” Acta Metall. Mater., vol. 40, no. 9, pp. 2225–2232, Sep. 1992.

[31] M. Liu and J. Cowley, “Hafnium carbide growth behavior and its relationship to the dispersion hardening in tungsten at high temperatures,” Mater. Sci. Eng. A, vol. 160, no. 2, pp. 159–167, Feb. 1993.

[32] J. J. Park, “Creep strength of a tungsten–rhenium–hafnium carbide alloy from 2200 to 2400 K,” Mater. Sci. Eng. A, vol. 265, no. 1–2, pp. 174–178, Jun. 1999.

[33] K. E. Rea, V. Viswanathan, a. Kruize, J. T. M. De Hosson, S. O’Dell, T. McKechnie, S. Rajagopalan, R. Vaidyanathan, and S. Seal, “Structure and property evaluation of a vacuum plasma

sprayed nanostructured tungsten–hafnium carbide bulk composite," Mater. Sci. Eng. A, vol. 477, no. 1–2, pp. 350–357, Mar. 2008.

[34] A. Mondal, A. Upadhyaya, and D. Agrawal, "Effect of heating mode and sintering temperature on the consolidation of 90W–7Ni–3Fe alloys," J. Alloys Compd., vol. 509, no. 2, pp. 301–310, Jan. 2011.

[35] J. A. Webb, C. Sparks, D. P. Butt, and M. Carroll, "SPS Fabrication of Alloys in Support of NTR Fuels Development Nuclear and Emerging Technologies for Space," Proc. Nucl. Emerg. Technol. Sp., vol. Proceeding, p. 3274, 2011.

[36] A. Luo, K. Shin, and D. Jacobson, "High temperature tensile properties of W- Re- ThO 2 alloys," Mater. Sci. Eng. A, 1991.

[37] R. Liu, Z. M. Xie, T. Hao, Y. Zhou, X. P. Wang, Q. F. Fang, and C. S. Liu, "Fabricating high performance tungsten alloys through zirconium micro-alloying and nano-sized yttria dispersion strengthening," vol. 451, pp. 35–39, 2014.

[38] S. K. Raghunathan, C. Persad, and D. L. Bourell, "High-energy , High-rate Consolidation of Tungsten and Tungsten-based Composite Powders," Mater. Sci., vol. 131, pp. 243–253, 1991.

[39] Z. Z. Fang, X. Wang, T. Ryu, K. S. Hwang, and H. Y. Sohn, "Int . Journal of Refractory Metals & Hard Materials Synthesis , sintering , and mechanical properties of nanocrystalline cemented tungsten carbide – A review," Int. J. Refract. Met. Hard Mater., vol. 27, no. 2, pp. 288–299, 2009.

[40] D. E. J. Armstrong and T. B. Britton, "Effect of dislocation density on improved radiation hardening resistance of nano-structured tungsten–rhenium," Mater. Sci. Eng. A, vol. 611, pp. 388–393, Aug. 2014.

[41] V. V. Ozherelyev, a. I. Bocharov, a. V. Bondarev, and Y. V. Barmin, "X-ray diffraction study of atomic structure of Hf–W amorphous alloys," Int. J. Refract. Met. Hard Mater., vol. 48, pp. 141–144, Jan. 2015

[42] D. Lee, M. A. Umer, H. J. Ryu, and S. H. Hong, "The effect of HfC content on mechanical properties HfC–W composites," Int. J. Refract. Met. Hard Mater., vol. 44, pp. 49–53, May 2014.

[43] C. Y. Dong, F. Hidetoshi, N. Kazuhiro, and N. Kiyoshi, “Friction Stir Welding of High Carbon Tool Steel (SK85) below Eutectoid Temperature †,” Young, vol. 38, no. 1, pp. 37–41, 2009

[44] B. W. Ahn, D. H. Choi, D. J. Kim, and S. B. Jung, “Microstructures and properties of friction stir welded 409L stainless steel using a Si 3 N 4 tool,” Mater. Sci. Eng. A, vol. 532, pp. 476–479, 2012

[45] M. P. Meshram, B. K. Kodli, and S. R. Dey, “Friction Stir Welding of Austenitic Stainless Steel by PCBN Tool and its Joint Analyses,” Procedia Mater. Sci., vol. 6, no. Icmpc, pp. 135–139, 2014.

[46] Konkol, “Comparison of Friction Stir Weldments and Submerged Arc Weldments in HSLA-65 Steel,” no. July, pp. 187–195, 2007.

[47] Z. Iqbal, A. N. Shuaib, F. Al-badour, N. Merah, and A. Bazoune, “Microstructure and hardness of friction stir weld bead on steel plate using W-25 % Re pin tool,” Proc. ASME 2014 12th Bienn. Conf. Eng. Syst. Des. Anal. ESDA June 25-27, 2014, Copenhagen, Denmark, pp. 1–6, 2014.

[48] G. Buffa, L. Fratini, F. Micari, and L. Settineri, “On the Choice of Tool Material in Friction Stir Welding of Titanium Alloys,” vol. 40, 2012.

[49] J. A. Webb, C. Sparks, D. P. Butt, and M. Carroll, “SPS Fabrication of Alloys in Support of NTR Fuels Development Nuclear and Emerging Technologies for Space,” Proc. Nucl. Emerg. Technol. Sp., vol. Proceeding, p. 3274, 2011.

[50] T. Liyanage, J. Kilbourne, A. Gerlich, and T. North, “Joint formation in dissimilar Al alloy/steel and Mg alloy/steel friction stir spot welds” Sci. Technol. Weld. Join, vol. 6, no. 14, pp. 500–508, 2009.

[51] C. Y. Dong, F. Hidetoshi, N. Kazuhiro, and N. Kiyoshi, “Friction stir welding of high carbon tool steel (SK85) below Eutectoid temperature” Transactions of JWRI, vol. 38, no. 1, pp. 37–41, 2009.

[52] P. J. Konkol and M. F. Mruczek, “Comparison of Friction Stir Weldments and Submerged Arc Weldments in HSLA-65 Steel” Welding Research, Supplement to the Welding Journal, July,2007, pp. 187–195, 2007.

[53] G. Buffa, L. Fratini, F. Micari, and L. Settineri, “On the Choice of Tool Material in Friction Stir Welding of Titanium Alloys" Proceedings of NAMRI/SME, Vol. 40, 2012.

[54] T. J. Lienert, W. L. Stellwag, Jr., B. B. Grimmett, and R. W. Warke, “Friction Stir Welding Studies on Mild Steel” Welding Research, Supplement to the Welding Journal, January, pp. 1–9. 2003.

[55] Bastier A, Maitournam Mh, Dang Van K, and Roger F., 2006, "Steady state thermo-mechanical modeling of friction stir welding", Science and Technology of Welding & Joining, 11, pp. 278-288.

[56] H. Park, H. Youn, J. Ryu, H. Son, H. Bang, and I. Shon, “Fabrication and mechanical properties of WC-10 wt .% Co hard materials for a friction stir welding tool application by a spark plasma sintering process” Journal of Ceramic Processing Research, vol. 13, no. 6, pp. 705–712, 2012.

[57] M.Wade, & A. P. Reynolds, "Friction stir weld nugget temperature asymmetry" Science and Technology of Welding & Joining, Vol. 15(1), pp. 64-69, 2010.

[58] G. E. Linnert, "Welding Metallurgy: Carbon and Alloy Steels" American Welding Society, 3rd ed., Vol. 2. pp. 312–325.,1967.

[59] T. H. Courtney, "Mechanical Behavior of Materials". pp. 309–317. New York. N.Y.: McGraw-Hill, 1990.

[60] K. E. Hughes, K. D. Nair, and C. M. Sellars, "Temperature and flow stress during hot extrusion of steel" Metals Technology, Vol.1(4), 161–169, 1974.

[61] W. M. Thomas, P. L. Threadgill, , and E. D. Nicholas, "Feasibility of friction stir welding of steel" Science and Technology of Welding and Joining 4(6): 365–372, 1999.

[62] B. K. Jasthi, W. J. Arbegast and S. M. Howard, "Thermal expansion coefficient and mechanical properties of friction stir welded invar (Fe-36%Ni)" J. Mater. Eng. Perform,18,(7), 925-934,2009.

[63] W. Gan, Z. T. Li and S. Khurana, "Tool materials selection for friction stir welding of L80 steel" Sci. Technol. Weld. Join., 12, (7), 610-613, 2007.

[64] A. Pradeep, S. Muthukumaran, "Two modes of metal transfer phenomenon in friction stir welding of low alloy steel plates" Proceedings of the 1st International Joint Symposium on Joining and Welding, Pages 305-312, 2013.

[65] Shuaib, A. R., Al-Badour, F., & Merah, N. (2015, July). Friction Stir Seal Welding (FSSW) Tube-Tubesheet Joints Made of Steel. In ASME 2015 Pressure Vessels and Piping Conference (pp. V06BT06A005-V06BT06A005). American Society of Mechanical Engineers

[66] T.Hartman, M.P.Miles, S.-T.Hong, R.Steel, S.Kelly, "Effect of PCBN tool grade on joint strengthand tool life in friction stir spot welded DP 980 steel" Journal of Wear, 328-329, 2015, 531-536

[67] E. Y. Ivanov, C. Suryanarayana, and B. D. Bryskin, “Synthesis of a nanocrystalline W – 25 wt .% Re alloy by mechanical alloying,” vol. 251, pp. 255–261, 1998.

[68] F.H. Froes, B.D. Bryskin, C.R. Clark, C. Suryanarayana, E.G. Baburaj, Mechanical alloying of W–25 wt.% Re powder, in: B.D. Bryskin (Ed.), Rhenium and Rhenium Alloys, TMS, Warrendale PA, 1997, pp. 569–583.

[69] M.S. Boldrick, E. Yang, C.N.J. Wagner J. Non-Cryst. Solids, 150 (1992), pp. 478–482.

[70] E.Y Ivanov, C Suryanarayana, , B.D Bryskin, Synthesis of a nanocrystalline W–25 wt.% Re alloy by mechanical alloying, Materials Science and Engineering: A Volume 251, Issues1–2, 15 August 1998, Pages 255–261.

[71] M.R. Akbarpour, E. Salahi, F. Alikhani Hesari, A. Simchi, H.S. Kim, Microstructure and compressibility of SiC nanoparticles reinforced Cu nanocomposite powders processed by high energy mechanical milling, Ceramics International 40 (2014) 951-960.

[72] C. Suryanarayana, Mechanical alloying and milling, Prog. Mater. Sci. 46 (2001) 1-184.

[73] J.M. Dickinson, L.S. Richardson Trans. ASM, 51 (1959), pp. 758-771.

[74] E.M. Savitskii, M.A. Tylkina, K.B. Povarova, Rhenium alloys, Izv. Nauka, Moskva (1965); Israel Program for Scientific Translations, Jerusalem, 1970, pp. 139–334.

[75] R.I. Jaffee, C.T. Sims, J.J. Harwood, The effect of rhenium on the fabricability and ductility of molybdenum and tungsten, in: 3rd Plansee Seminar Proceedings, Pergamon, New York, 1959, pp. 380-411

[76] C. Suryanarayana, Metals Mater., 2 (1996), pp. 195–209.

[77] C. Suryanarayana, Bibliography on mechanical alloying and milling, Cambridge International Scientific Publishing, Cambridge, 1995

[78] F.H. Froes, B.D. Bryskin, C.R. Clark, C. Suryanarayana, E.G. Baburaj, Mechanical alloying of W–25 wt.% Re powder, in: B.D. Bryskin (Ed.), Rhenium and Rhenium Alloys, TMS, Warrendale, PA, 1997, pp. 569–583.

[79] Y. Waseda, K. Shinoda, E. Matsubara, X-Ray Diffraction Crystallography, Springer-Verlag, Berlin Heidelberg, 2011.

[80] Saheb N, Aliyu IK, Hassan SF, Al-Aqeeli N. Matrix Structure Evolution and Nanoreinforcement Distribution in Mechanically Milled and Spark Plasma Sintered Al-SiC Nanocomposites. Materials. 2014; 7(9):6748-6767.

[81] A.S. Khan, B. Farrokh, L. Takacs, Mater. Sci. Eng A, 489 (2008) 77.

[82] S. Hwang, C. Nishimura, P.G. McCormick, Mater. Sci. Eng. A, 318 (2001) 22.

[83] Dongju Lee, Malik Adeel Umer, Ho J. Ryu, Soon H. Hong, The effect of HfC content on mechanical properties HfC-W composites, Int. Journal of Refractory Metals and Hard Materials 44 (2014) 49-53.

[84] J.M. Tao, X.K. Zhu, R.O. Scattergood, C.C. Koch, Mater. Design, 50 (2013) 22.

[85] R.M. German, Sintering Theory and Practice. New York, John Wiley, (1996).

[86] J. E. Garay, "Current-Activated, Pressure-Assisted Densification of Materials," Annual review of materials research, vol. 40, pp. 445-468, 2010. ORRÙ R, LICHERI R, MARIO A LOCCI, CINCOTTI A, CAO G.

[87] Consolidation/synthesis of materials by electric current activated/assisted sintering. Mater Sci Eng R, 2009, 63: 127–287.

[88] VISWANATHAN V, LAHA T, BALANI K, AGARWAL A, SEAL S. Challenges and advances in nanocomposite processing techniques. Mater Sci Eng R, 2006, 54: 121–285.

[89] ADACHI J, KUROSAKI K, UNO M, YAMANAKA S. Porosity influence on the mechanical properties of polycrystalline zirconium nitride ceramics. J Nucl Mater, 2006, 358: 106–110.

[90] JIN X, GAO L, SUN J. Preparation of nanostructured $Cr_{1-x}Ti_xN$ ceramics by spark plasma sintering and their properties [J]. Acta Mater, 2006, 54: 4035–4041.

[91] KIM Y H, SEKINO T, KUSUNOSE T, NAKAYAMA T, NIIHARA, K, KAWAOKA H. Electrical and mechanical properties of K, Ca ionic-conductive silicon nitride ceramics [J]. Ceram Trans, 2005, 165: 31–38.

[92] K. Rajeswari, U.S. Hareesh, R. Subasri, D. Chakravarty, R. Johnson, Science of Sintering, 42 (2010) 259.

[93] V. Pouchly, K. Maca, Y. Xiong, J.Z. Shen, Science of Sintering, 44 (2012) 169.

[94] D. Veljović, G. Vuković, I. Steins, E. Palcevskis, P.S. Uskoković, R. Petrović, D. Janaćković, Science of Sintering, 45 (2013) 233.

[95] Grácio, J.; Picu, C.R.; Vincze, G.; Mathew, N.; Schubert, T.; Lopes, A.; Buchheim, C. Mechanical Behavior of Al-SiC Nanocomposites Produced by Ball Milling and Spark Plasma Sintering. Metallurgical and Materials Transactions A 2013, 44, 5259-5269.

[96] Kamrani, S., Razavi Hesabi, Z., Riedel, R., Seyed Reihani, S.M. Synthesis and characterization of Al-SiC nanocomposites produced by mechanical milling and sintering, Advanced Composite Materials 2011, 20, 13-27.

[97] Candido, G.M.; Guido, V.; Silva, G.; Cardoso, K.R. Effect of the Reinforcement Volume Fraction on Mechanical Alloying of AA2124-SiC Composite, Materials Science Forum 2012, 660-661, 317-324.

[98] Munoz-Morris, M.; Garcia Oca, C.; Morris, D. An analysis of strengthening mechanisms in a mechanically alloyed, oxide dispersion strengthened iron aluminide intermetallic. Acta. Mater. 2002, 50, 2825–2836.

[99] Dai, L.; Ling, Z.; Bai, Y. A strain gradient-strengthening law for particle reinforced metal matrix composites. Scripta Mater. 1999, 41, 245–252.

[100] Chawla, N.; Shen, Y.-L. Mechanical behavior of particle reinforced metal matrix composites. Adv. Eng. Mater. 2001, 3, 357–370.

[101] Casati, R.; Vedani, M. Metal matrix composites reinforced by nano-particles-a review. Metals 2014, 4, 65–83.

[102] M.Y. Nazmy, in: N.S. Stoloff, V.K. Sikka (Eds.), Physical Metallurgy and Processing of Intermetallic Compounds, Chapman & Hall, New York, 1996, p. 120

[103] J. Halling, Wear 35 (1975) 239.

[104] J.F. Archad, J. Appl. Phys. 24 (1953) 981.

[105] A.J. Clegg, A.A. Das, Brit. Foundryman 70 (1977) 333.

[106] A.D. Sarkar, Wear of Metals, Pergamon Press, Oxford, 1976, p. 49.

[107] B.K. Prasad, K. Venkateswarlu, O.P. Modi, A.H. Yegneswaran, J. Mater. Sci. Lett. 15 (1996) 1773.

[108] I.-Y. Kim, J.-H. Lee, G.-S. Lee, S.-H. Baik, Y.-J. Kim, Y.-Z. Lee, Friction and wear characteristics of the carbon nanotube–aluminum composites with different manufacturing conditions, Wear 267 (2009) 593–598.

[109] N. Saheb, Spark plasma sintering of Al6061 and Al2124 alloys, Advanced Materials Research 284–286 (2011) 1656–1660.

[110] H.-L. Lee, W.-H. Lu, S.L.-I. Chan, Abrasive wear of powder metallurgy Al alloy 6061-SiC composites, Wear 159 (1992) 223–231.

[111] Thompson, B., Babu, S.S., 2010, Tool degradation characterization in the friction stir welding of hard metals, Welding Journal (Miami, Fla), 89 (12): 256s-261.

[112] Barnes, S. J., Bhatti, A. R., Steuwer, A., Johnson, R., Altenkirch, J., & Withers, P. J. (2012). Friction stir welding in HSLA-65 steel: part I. Influence of weld speed and tool material on microstructural development. Metallurgical and Materials Transactions A, 43(7), 2342-2355.

APPENDIX

Journal publications from thesis dissertations

1. N. Saheb, **Zafar Iqbal**, A. Khalil, A. S. Hakeem, N. Al-Aqeeli et al "Spark Plasma Sintering of Metals and Metal Matrix" Nanocomposites: A Review Hindawi Publishing Corporation Journal of Nanomaterials Volume 2012, Article ID 983470, 13 pages DOI:10.1155/2012/983470
2. **Zafar Iqbal**; Nouari Saheb; Abdel Rahman Shuaib," W-25%Re-HfC Composite Materials for Pin Tool Material Applications: Synthesis and Consolidation" Published in Journal of Alloys and Compounds, March 2016. DOI: 10.1016/j.jallcom.2016.03.030
3. **Zafar Iqbal**, Fadi A.A. Al-Badour, Abdelrahman Nasr Shuaib, Nesar Merah, and Abdelaziz Bazoune "Friction Stir Welding of ASTM A516-70 using W-25% Re Tool" submitted in Journal of Advanced Manufacturing Technology. JAMT-D-16-01170
4. **Zafar Iqbal,** Nesar Merah, Abdel Rahman Shuaib, "Sliding wear behavior of W-Re-HfC composites for Pin tool applications to be submitted soon in Journal of Wear.

Conference Publications from thesis dissertations

5. **Zafar Iqbal,** A.N. Shuaib1, F. Al-Badour, N. Merah, and A. Bazoune, "Microstructure and hardness of friction stir weld bead on steel plate using W-25%Re pin tool", Proceedings of the ASME 2014 12th Biennial Conference on Engineering Systems Design and Analysis ESDA2014 June 25-27, 2014, Copenhagen, Denmark DOI: 10.1115/ESDA2014-20546
6. **Zafar Iqbal,** Abdel Rahman Shuaib, Fadi Al-Badour, Nesar Merah, and Abdelaziz Bazoune, "Experimental evaluation of wear features of W-25%Re pin tool used in friction stir welding mild steel" Proceedings of the ASME 2014 International Mechanical Engineering Congress & Exposition IMECE2014 November 14-20, 2014, Montreal, Quebec, Canada DOI: 10.1115/IMECE2014-38916.

Vitae

Name	Zafar Iqbal
Nationality	Pakistani
Date of Birth	8/4/1982
Email	zafariqbal@kfupm.edu.sa

Address: Department of Mechanical Engineering, King Fahd University of
Petroleum and Minerals, Dhahran 31261, Saudi Arabia

RESEARCH INTERESTS

- Tool development for Friction Stir Welding of steel
- Development and characterization of metal matrix nanocomposites by Spark Plasma Sintering
- Impressed current Cathodic protection of gas pipelines
- Electrochemical reduction of metal oxides in molten salts

EDUCATION

1. **PhD in** ***Mechanical Engineering*** (2011- 2016)

   Major: ***Material and Manufacturing***

Thesis Title: Development of Tungsten-Rhenium based tool for Friction Stir Welding of steel.

Institute: King Fahd University of Petroleum & Minerals Dhahran, Saudi Arabia

2. **M.S. in** ***Materials Science and Engineering*** (2005-2007) **Secured 1st Position**

   Thesis Title: Production and characterization of Al-Mg Matrix Composite reinforced with SiC

   Institute: Pakistan Institute of Engineering and Applied Sciences, Islamabad Pakistan

3. **B.S honors in** ***Metallurgical & Materials Engineering*** (2001-2005)

   Thesis Title: Impressed current cathodic protection of gas pipelines

   Institute: University of Engineering and Technology, Lahore, Pakistan

RESEARCH AND ACADEMIC EXPERIENCE

Lecturer-B (KFUPM) **February 2011----------June 2016**

- Developed nanocrystalline Tungsten-Rhenium material by Spark Plasma Sintering for Friction Stir Welding (FSW) of high melting point materials such as steel.
- Successfully tested the developed tool for FSW of mild steel using Friction Stir Welding CNC machine.
- Published 3 journal and 3confernce papers
- Taught lab courses
- Active member for ABET committee.
- Participated and presented my two papers in the Proceedings of the ASME 2014 and 2015

- Involved in research oriented projects NSTIP 13-ADV-2155-04 & NSTIP # 11-ADV2130-04 project
- Four year experience of operating CNC machine used in the FSW of steel.
- Hand-on-Experience on characterization Techniques such as X-ray Diffraction, Field Emission Scanning electron microscope, tensile, compression, hardness, fatigue, impact creep, TGA, metallography, casting, machining, welding, metrology and cold working techniques.
- Experience of conducting corrosion monitoring and testing experiments.

Assistant Professor (PIEAS) October 2007--------February 2011

1. Taught core courses in the field Metallurgy and materials science.
2. PIEAS has been ranked No. 1 by the Higher Education Commission (HEC), Pakistan (in 2006, 2012, and 2013) & ranked 106 in the top 250 Asian Universities.
3. Published 2 journal and 3 conference papers
4. Attended 13th Master Trainers Faculty Development Program
5. Supervised and Co-supervised MS students
6. Actively participated in the establishment of Centre for Nanotechnology at PIEAS
7. Active organization member for organizing local conferences
8. Four week training on “Impressed Current Cathodic Protection of Gas Pipeline”: at SNGPL, Pakistan
9. Won 1st prize in poster presentation award at ISAM, Islamabad,2007

COURSES TOUGHT

Course Name	Code	Institute
1. Corrosion and its Control	CME-540	PIEAS, ISLAMABAD PAKISTAN
2. Nanomaterials	CME-560	PIEAS, ISLAMABAD PAKISTAN
3. Mechanical Metallurgy	CME-504	PIEAS, ISLAMABAD PAKISTAN
4. Materials Science	ME-217	KFUPM, DHAHRAN, SAUDI ARABIA
5. Manufacturing Processes	ME-323	KFUPM, DHAHRAN, SAUDI ARABIA
6. Materials Science	ME 205	KFUPM, DHAHRAN, SAUDI ARABIA

PUBLICATIONS

Journal Publications 2007 to 2016

1. N. Saheb, **Z. Iqbal**, A. Khalil, A. S. Hakeem, N. Al-Aqeeli et al "Spark Plasma Sintering of Metals and Metal Matrix" Nanocomposites: A Review Hindawi Publishing Corporation Journal of Nanomaterials Volume 2012, Article ID 983470, 13 pages DOI:10.1155/2012/983470
2. **Zafar Iqbal**; Nouari Saheb; Abdel Rahman Shuaib," W-25%Re-HfC Composite Materials for Pin Tool Material Applications: Synthesis and Consolidation" Published in Journal of Alloys and Compounds, March 2016. DOI: 10.1016/j.jallcom.2016.03.030
3. R Khan, M Mehmood, R Rizwan, J Ahmad, M Ul Hasan, **Z Iqbal** et al "Corrosion behavior of zinc-nickel alloy coatings electrodeposited in additive free chloride baths" Corrosion Engineering, Science and Technology 46 (7), 755-761

4. KK Khan, M Mehmood, M ul Hassan, J Ahmad**, Z Iqbal**, T Muddasser "Gas nitriding of electrodeposited Ni–W alloys" Metal Science and Heat Treatment 53 (1), 87-90
5. **Zafar Iqbal**, Fadi A.A. Al-Badour, Abdelrahman Nasr Shuaib, NesarMerah, and Abdelaziz Bazoune "Friction Stir Welding of ASTM A516-70 using W-25% Re Tool" submitted in Journal of Advanced Manufacturing Technology. JAMT-D-16-01170
6. **Zafar Iqbal,** Nesar Merah, Abdel Rahman Shuaib, "Sliding wear behavior of W-Re-HfC composites for Pin tool applications to be submitted soon in Journal of Wear.

Conference Publications

7. **Z. Iqbal,** A.N. Shuaib1, F. Al-Badour, N. Merah, and A. Bazoune, "Microstructure and hardness of friction stir weld bead on steel plate using W-25%Re pin tool", Proceedings of the ASME 2014 12th Biennial Conference on Engineering Systems Design and Analysis ESDA2014 June 25-27, 2014, Copenhagen, Denmark DOI: 10.1115/ESDA2014-20546
8. **Zafar Iqbal,** Abdel Rahman Shuaib, Fadi Al-Badour, Nesar Merah, and Abdelaziz Bazoune, "Experimental evaluation of wear features of W-25%Re pin tool used in friction stir welding mild steel" Proceedings of the ASME 2014 International Mechanical Engineering Congress & Exposition IMECE2014 November 14-20, 2014, Montreal, Quebec, Canada DOI: 10.1115/IMECE2014-38916.
9. Ihsan ulhaq Toor, N. Ahmad, **Z. Iqbal**, H. Z. Shafi, H.M.Irshad, " Comparison of corrosion behavior of commercial stainless steels with and without Si addition" Conference: 16TH MECC to be held from 8~11 Feb 2016, Manama, Bahrain.
10. **Zafar Iqbal,** M. A. Shaikh, M. Mehmood "Production and characterization of al-mg matrix composite by mechanical alloying" International Symposium on Advanced Materials, ISAM September 2007
11. Jawad Ahmad, M. A. Sheikh, J.I.Akhtar, **Zafar Iqbal** "Synthesis and characterization of Fe-Aluminide-Alumina composites" International Bhorban Conference on Science and Technology, 19-22 Jan., 2009